Přírodovědecká fakulta
Univerzita Palackého v Olomouci

Katedra experimentální fyziky

Diplomová práce

Analýza a optimalizace kalibračního procesu fluorescenčního teleskopu projektu FAST

Autor	Koutný Michal
Vedoucí práce	Mgr. Dušan Mandát Ph.D.
Studijní obor	Nanotechnologie
Forma studia	Prezenční
Rok	2023

Bibliografická identifikace

Jméno a příjmení autora	Koutný Michal
Název práce	Analýza a optimalizace kalibračního procesu fluorescenčního teleskopu projektu FAST
Typ práce	diplomová
Pracoviště	Katedra experimentální fyziky, Společná laboratoř optiky
Vedoucí práce	Mgr. Dušan Mandát Ph.D.
Rok obhajoby práce	2023
Počet stran	75
Počet příloh	1
Jazyk	anglický
Abstrakt	The Fluorescence detector Array of Single-pixel Telescopes (FAST) je koncept moderní observatoře určené k detekci ultra vysoko-energetického kosmického záření (UHECRs). Tato práce nejdříve pokládá teoretický základ ohledné kosmického záření, atmosférické spršky a možných detekčních principů. Dále je práce zaměřena na FAST projekt, konkrétně použitých fotonásobiču (PMT) a UV LED flasheru. Analýzou kalibračních dat je možné posoudit stabilitu fotonásobiču a kvalitu naměřených dat. Analýza je primárně zaměřena na časovou a teplotní stabilitu. Práce zpracovává kalibrační data z Pierre Auger Observatory a Telescope Array. Na závěr je navržen automatizovaný proces jak analýzy, tak vizualizace UV LED kalibračních dat a jeho potenciální integrace do měřícího řetězce projektu FAST.
Klíčová slova	kosmické záření, UHECR, EAS, FAST projekt, fotonásobič, relativní kalibrace, absolutní kalibrace

Bibliographical identification

Author's first name and surname	Koutný Michal
Title	Analysis and optimization of the calibration process of the FAST fluorescence telescope
Type of thesis	master
Department	Department of Experimental Physics, Joint Laboratory of Optics
Supervisor	Mgr. Dušan Mandát Ph.D.
Year of presentation	2023
Number of pages	75
Number of appendices	1
Language	english
Abstract	The Fluorescence detector Array of Single-pixel Telescopes (FAST) is a concept for next generation observatory of Ultra High-Energy Cosmic Radiation. This thesis lays the theoretical foundations of these energetic cosmic rays, the induced extensive air shower and the detection methods. The focus is then set on the fluorescent FAST telescopes, mainly the Photomultiplier Tubes and the UV LED calibration system present on the telescopes. By analyzing the data from the individual UV LED calibration events, insight into PMT stability can be provided. Of particular importance is the stability with respect to both time and temperature. The thesis analyzes data from both the Pierre Auger Observatory and Telescope Array. Furthermore, an automated process to both analyze and visualize the UV LED calibration data is then presented.
Keywords	cosmic radiation, UHECR, EAS, FAST project, photomultiplier tube, relative calibration, absolute calibration

Prohlášení

Prohlašuji, že jsem předloženou diplomovou práci vypracoval samostatně pod vedením Mgr. Dušana Mandáta Ph.D. a že jsem použil zdrojů, které cituji a uvádím v seznamu použitých zdrojů.

V Olomouci dne .....

.....
podpis

Chtěl bych poděkovat vedoucímu diplomové práce Mgr. Dušanu Mandátovi, Ph.D. za čas, nesmírnou trpělivost a odhodlání při tvorbě této práce. Dále bych chtěl poděkovat Mgr. Petru Hamalovi, Ph.D. za cenné rady během tvorby práce a též Mgr. Vlastimilu Jílkovi za pomoc s konverzí FAST dat.

Table of Contents

Introduction

The Fluorescence detector Array of Single-pixel Telescopes (FAST) is a concept for next generation observatory of highly energy cosmic particles. These Ultra High-Energy Cosmic Rays (UHECRs) are particles, predominantly protons or heavy atom nuclei, that reach the Earth at incredible velocities, at energies in the range of 10^{18} to 10^{20} electronVolts (eV). The frequency at which these particles reach the Earth is exceptionally low, as the estimated minute flux of UHECRs is one such particle per square kilometer a year.

Detecting these rare cosmic rays is challenging since any observatory attempting to do so must cover a vast area to increase the likelihood of detecting these extremely energetic particles. When a UHECRs reaches the atmosphere of our planet, a cascade of secondary particles is induced. This cascade is denoted as an extensive air shower. During the air shower, by the process of excitation and subsequent deexciation of atmospheric nitrogen atoms, faint fluorescent UV light is produced. The FAST project employs fluorescent detectors in the form of telescopes, that observe the UV light. In combination with other detection methods, for example surface detectors, energy, point of origin or particle composition of the UHECRs can then be estimated. The detectors are set up in a net and data from multiple such detectors has to be taken into account when analyzing any possible UHECRs detection candidates.

The telescope is comprised of a set of one central circular primary mirror surrounded by 8 secondary mirrors in a "petal"shape. The mirrors then reflect the UV light onto a camera box with four 200mm long Photomultiplier Tubes (PMT) positioned in a 2×2 matrix to further amplify the signal obtained. A UV filter is placed at the aperture of the telescope, to eliminate any parasitic light causing damage to the PMTs. Furthermore, the FAST telescope is covered by a shroud to protect against dust sedimentation and aerosols. Finally, the telescope offers a field of view (FOV) of $30° \times 30°$ along with a collecting area of 1 m^2. FAST telescopes have been deployed to the Pierre Auger Observatory in Argentina and to the Telescope Array in Utah, U.S.A.

Calibration of the PMT signal is of vital importance, and thus all FAST telescopes are provided with several sensors measuring the temperature, pressure, humidity, light or shutter status. Furthermore, the telescope is equipped with a UV LED flasher placed on the central primary mirror. The PMTs can then detect the UV LED flashes for the sole purpose of adequate calibration. Of particular importance is the data regarding PMT stability with respect to both time and temperature. Data then can be visualized in absolute values, in the number of photo-electrons produced (Np.e) in absolute calibration, or by comparing the PMT signal to a reference PMT, in relative values through relative calibration.

The goal of this thesis is to develop an automated process for an analysis of the UV LED calibration data and subsequent real-time visualization of all the necessary measurements. Additionally, data obtained from calibration runs from the FAST telescopes stationed on the PAO and TA sites are analyzed. Of particular importance is PMT stability in regard to both time and temperature. The entire process can then be integrated into the FAST project for further usage by the individual shifters operating the FAST telescopes remotely.

1. Foundations

1.1. Cosmic radiation

Cosmic radiation or cosmic rays are particles originating in space that eventually at incredible speeds reached the Earth. The rays consist of electromagnetic radiation, in the from of x-rays or even gamma ray bursts, and charged particles, predominantly protons. Most of these particles interact with the Earth's atmosphere, where they are subsequently absorbed, but some can reach Earth's surface, where they can be detected. In fact, about 11 % of the annual radiation intake of an average human being comes from the cosmos. The closest and by far the largest source of cosmic radiation is the Sun. Both the nature and energetic spectra of Sun's radiation is mostly well established, whether it is UV-radiation or solar wind that might interfere with our magnetosphere, in the form of breathtaking auroras or static on the electrical gadgets we use everyday.[1]

The Sun, however is only capable of producing radiation of relatively small energies. Various detectors have discovered radiation larger than that of the Sun by several factors of 10. The point of origin of these high-energy cosmic rays is also unclear. Currently, there are few models describing the process of creation of these high energy rays. Some of the proposed sources can be inside our own galaxy, for example the black hole in the galactic center in the constellation Sagittarius. Other sources may include supernova explosions or collisions between stars, such as those involving neutron stars. By examining such radiation we can deduce from which direction it hit the Earth, and to a reasonable degree assume the point of origin of said radiation. Extra-galactic sources of high-energy cosmic rays have been discovered in galaxies far from our own.

The energies of cosmic radiation is measured in electronvolts (eV). One electronvolt is the amount of kinetic energy an electron would gain if placed under electric potential difference of one Volt in a vacuum. For example, a photon with the wavelength of 540 nm (which our eyes would assign the color green), carries $\sim$ 2.3 eV of energy. Aforementioned UV radiation falls in the range of 3 eV - 12 eV. In the context of high-energy astroparticle physics, predominantly powers of electronvolts are employed. The peak of energy distribution of high-energy cosmic radiation is $\sim$ 0.3 GeV, or 0.3×10^9 eV. The largest particle energies produced on Earth are done particle collider experiments in Cern. The energies of the accelerated particles reach 10^{13} eV. The cosmic radiation exceeds such energies Other methods of quantifying cosmic rays are for example the point of origin, electric charge, or particle composition.

The rate of all cosmic radiation is however not constant. The higher the energy of the particle, the lower the frequency, or the flux of the radiation. The visualization of such relation can be seen in figure 1. The minute flux of cosmic radiation around 10^{11} eV, or 100 GeV is $\sim$ 1 particle per squared meter per second. With increasing energies the flux decreases dramatically. A particle with 10^{16} eV of kinetic energy hits a square meter once per year. This behaviour continues further, as a cosmic ray with immense energy of 10^{18} eV is estimated to make contact with an area of square kilometer once a year. Cosmic radiation of energies up to $\sim 10^{10}$ eV can be attributed to a large extent to solar activities, such as solar wind or eruptions. Particles with energies up to about 10^{15} eV can be attributed to other phenomena occurring within our galaxy. The low minute flux of cosmic rays of higher energies, one particles per square kilometer per year, constrains our ability to further study said cosmic radiation. It is however presumed that such particles of immense energies could only be of extra-galactic origin, for example generated in various mysterious processes not yet thoroughly examined, such as an interaction of black holes in active galactic nuclei. These ultra-high energy cosmic rays (UHECRs) are still subject to much scientific debate and endeavours. The absence of a solid theoretical model explaining the origin of such immensely energetic radiation continues to motivate extensive research efforts and theoretical inquiries. UHECRs will be further described in chapter 1.1.2.

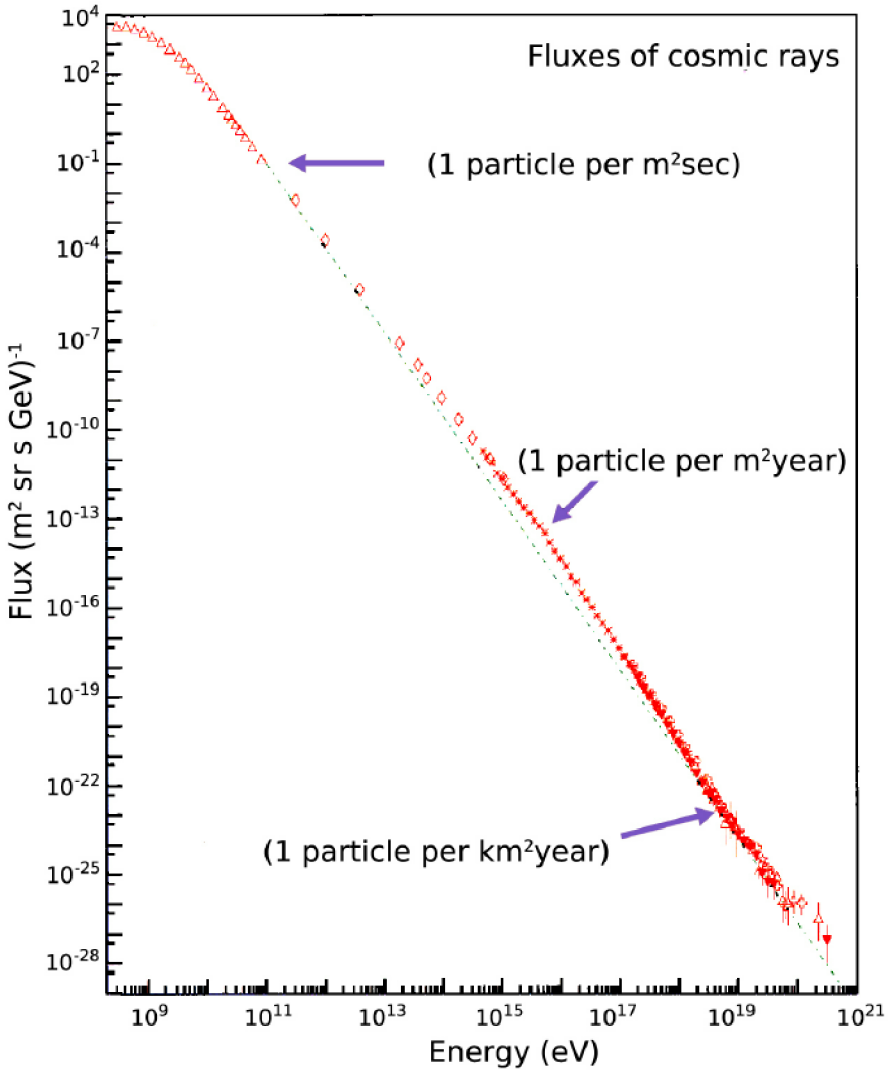

Figure 1 | Relation between the energy and the flux of cosmic radiation. [2]

1.1.1. High energy cosmic radiation

Cosmic rays consist primarily of high energy electromagnetic radiation, such as x-ray or gamma rays and accelerated charged particles, mainly protons and to some extent alpha particles and electrons. Cosmic radiation of lower energies (and higher minute flux) originated during various processes involving the Sun. Therefore, these rays are sometimes called Solar Energetic Particles (SEPs) or solar cosmic rays. The energy of such radiation induced in the Sun ranges from keV to GeV. The particle composition is dominated by protons and electrons with occasional heavy nuclei. SEPs are produced in solar events, such as solar flares and eruptions. Several missions have been established to monitor the Sun's activity an subsequent solar eruptions. Projects such as NASA's STEREO and ESA's COMESEP have successfully studied not only the composition of SEPs and the Sun, but also its effect on space weather, solar wind, and subsequently the effect on Earth. Note that the terminology is not absolute, certain sources may opt to exclude Solar Energetic Particles (SEPs) from the classification of cosmic rays.

Cosmic rays of higher energies, up to $\sim 10^{15}$ eV, with drastically reduced minute flux, are presumed to be of extrasolar, or galactic origin. The composition of said radiation is heavily dominated by charged particles such as protons from stripped hydrogen atoms and alpha particles with some heavier ions. These cosmic rays are further denoted as Galactic Cosmic Rays (GCRs). They are likely formed during violent and explosive events outside our solar system, such as supernovae explosions. Other possible phenomena of origin include star collision, neutron star merger or various interactions with the galactic magnetic field. These highly energetic cosmic rays are associated with a burst of gamma radiation, although of much lesser energy than that of the GCR itself. By gamma-ray mapping of the sky, valuable insight can be obtained into the possible sources of GCRs. Such gamma-ray map of the sky can be seen in figure 2.

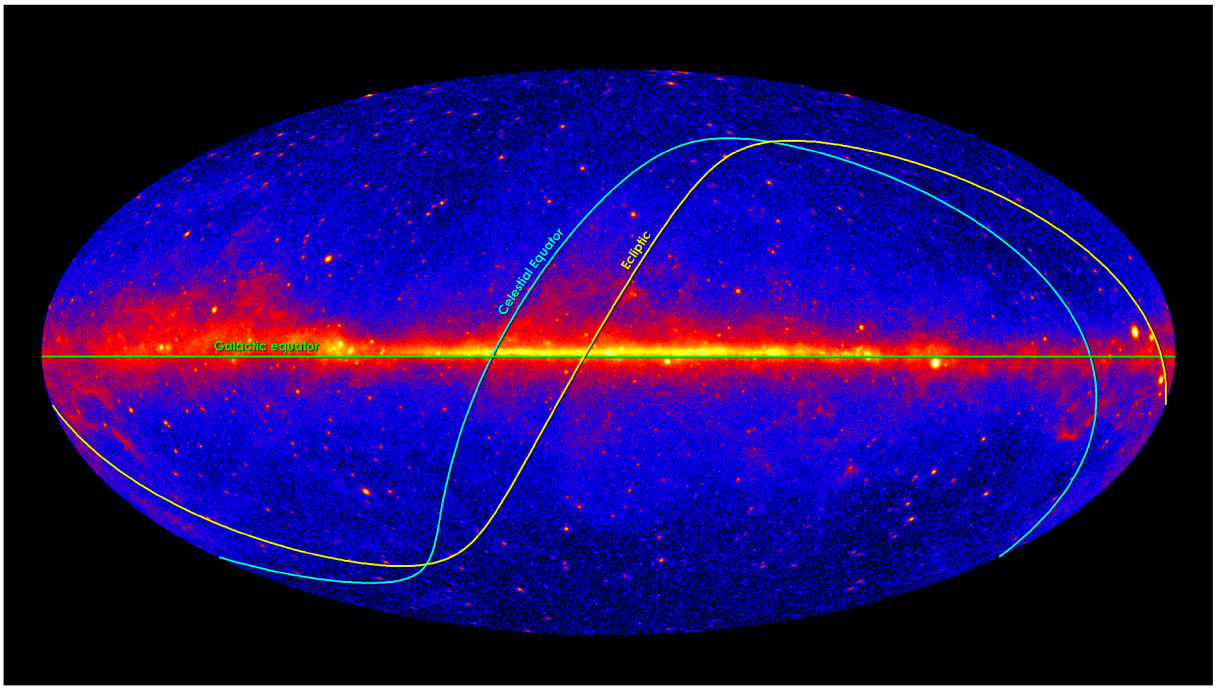

Figure 2 Gamma ray map of the sky. Brighter colors represent regions with higher intensity. Galactic and celestial equator, along with the ecliptic are highlighted. [3]

Regions with the highest intensity of gamma radiation are located along the galactic equator, implying the origin to be that of our own galaxy. Gamma ray burst are a decent indicator of GCRs, as they are formed upon interaction of an energetic cosmic ray with interstellar gas through a process called knows as pion decay. Pions, or π mesons are subatomic particles composed of a quark and its corresponding anti-quark. These particles are extremely unstable and short-lived, as the mean lifetime of these particles is in the range of nanoseconds at most. These particles are created upon interaction of an interstellar gas with a high energy cosmic ray. After their inevitable decay, they produce two gamma photons that can be detected upon reaching the Earth. Galactic cosmic ray study provides insight into the creation process of highly energetic particles, with energies in range that we cannot reproduce in currently available experimental instruments and conditions. Research into these cosmic rays can provide information of galactic and stellar formation and its inevitable demise. Some of the projects researching gamma rays and GCRs are for example NASA's Fermi Gamma-ray Space Telescope, CREAM (Cosmic Ray Energetics and Mass) or SuperTIGER (Super Trans-Iron Galactic Element Recorder).

1.1.2. UHECRs

Cosmic rays with energies larger than 10^{18} eV are labeled as Ultra High-Energy Cosmic Rays, or UHECRs. These incredibly energetic cosmic particles are exceptionally rare, as one such particle makes impact with an area of a square kilometer once a year. These mysterious rays are currently subject to much scientific debate and research, as they might provide valuable information regarding the very birth of our universe and early galaxies. To provide context on the energy of UHECRs, it is noteworthy that a small bird in flight carries a kinetic energy of approximately 2.5 J, equivalent to approximately 1.5×10^{18} eV. The energy of a flying bird consisting of a lot more than trillions of atoms packed into a single accelerated energetic particle.

In terms of particle composition, there is great uncertainty regarding the nature of said particles. It is presumed that only charged particles with non-zero rest mass are eligible for such a profound acceleration to reach massive energies. Protons from hydrogen atoms are one possibility, although they dominate the spectra of lower energies. Another suggested alternative is iron nuclei. The process of generation of these cosmic rays is also unclear, the scientific community lacks a solid model explaining such phenomena producing these immensely energetic particles. Most UHECRs are thought to have an extra-galactic origin, meaning they are formed in distant galaxies in active galactic nuclei (AGNs), those are supermassive black holes in the centers of massive galaxies that are actively accreting matter. Another proposed alternative is the merger of neutron stars. Another potential astrophysical event possibly capable of producing UHECRs are massive supernovae explosions.

When cosmic rays of smaller energies reach the Earth, they are inevitably deflected by Earth's magnetic field, as these particles are predominantly charged themselves. The trajectory of these particles is altered and they appear to hit the Earth from every angle. Deducing the point of origin of such particles is highly problematic. However, the case of UHECRs does not follow this pattern. The high-energetic nature and incredible velocities of UHECRs allows them to blast through the Earth's magnetic field with virtually no trajectory alteration.

When high-energy cosmic particles reach the Earth, they can undergo interactions with its atmosphere. The primary cosmic ray bombards the atoms of our atmosphere, causing generation of a large amount of secondary particles. If the primary cosmic particle carries enough energy, the secondary particles can also further produce a cascade of additional particles and the cycle can continue. Some of these particles have an incredibly short mean lifetime, as previously mentioned pions that through the process of weak electromagnetic interaction decay into muons, can be detected at the surface. Some of the energetic particles can cause excitation of atoms in our atmosphere (predominantly nitrogen) and by subsequent de-excitation can produce faint fluorescent light. This cascade of secondary particles is called an extensive air shower (EAS). The primary method of detection of UHECRs utilizes to some degree detection and analysis of an EAS. An illustration of such EAS can be seen figure 3 and will be described further in chapter 1.2.1. [4]

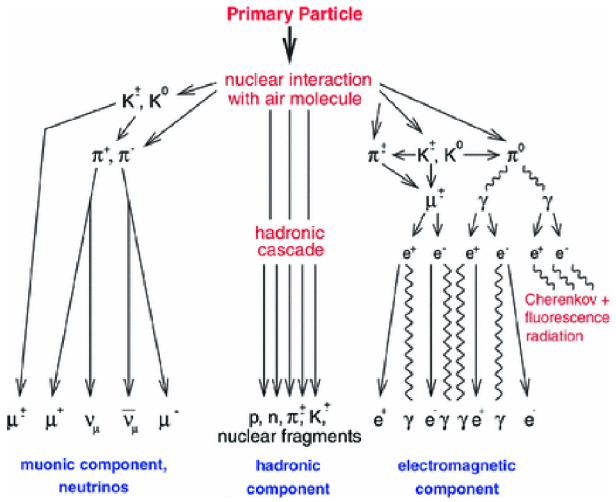

Figure 3 An illustration of an EAS. Primary cosmic particle may induce a cascade of secondary particles, such as pions, muons, neutrinos or fluorescent light. [4]

1.2. Detection of UHECRs

1.2.1. Extensive air showers

Cosmic rays were originally discovered in 1912 by Victor Hess utilising a balloon equipped with several electrometers ascending to an altitude of more than 5 km. Electrometers served as devices measuring ion production in a sealed chamber due to external radiation. Hess found that the level of radiation has risen significantly with increasing altitude. The discovery of UHECRs is generally attributed to Dr. John D. Linsley and Livio Scarsi several decades later, in 1962 during the Volcano Ranch experiment. A series of ground-based particle detectors were utilized to detect a particle of an energy in the range of 10^{20} eV. Balloon-borne detection methods are still used to this day, for example in the Cosmic Ray Energetics And Mass (CREAM) project. However, currently most wide-spread detection methods of UHECRs employ their secondary effect on the atmosphere, predominantly in the form of an EAS.

When a cosmic ray of sufficient energy interacts with atoms of the Earth's atmosphere, it produces a cascade of secondary particles. This event is denoted as an extensive air shower. During such an event, countless exotic particles are formed, for example pions, muons and many others. The primary interaction is dominated by the formation of pions, in the form of $\pi^{\pm}$ or π^0 pions, or charged and neutral pions. These subatomic particles are highly unstable, and quickly decay via weak electromagnetic interaction into either muons and neutrino or a pair of high-energy photons, respectively. Due to the incredible velocity of the primary cosmic ray, the collision products follow the initial trajectory, with only a slight dispersion with higher factors of interaction occurring. An illustration of such an event can be seen in figure 4.

As the secondary particles travel faster than the speed of light in our atmosphere, Cherenkov light is produced. Special Cherenkov detectors can detect this light and provide information regarding the original cosmic ray. Other detectors can spot the neutrinos produced during the pion decay and map both the direction and energy of the incident particle. A set of surface detectors can capture other subatomic particles and map the entire air shower. Fluorescent light produced upon interaction of the particles with nitrogen atoms in our atmosphere can also be utilized as a viable detection method. Surface-based and fluorescent detectors are further described in sections 1.2.2 and 1.2.3, respectively.

Some of the largest projects dedicated to the detection and research into UHECRs include the Akeno Giant Air Shower Array (AGASA) in Japan, Pierre Auger observatory (PAO) in Argentina and Telescope Array (TA) in Utah, U.S.A.

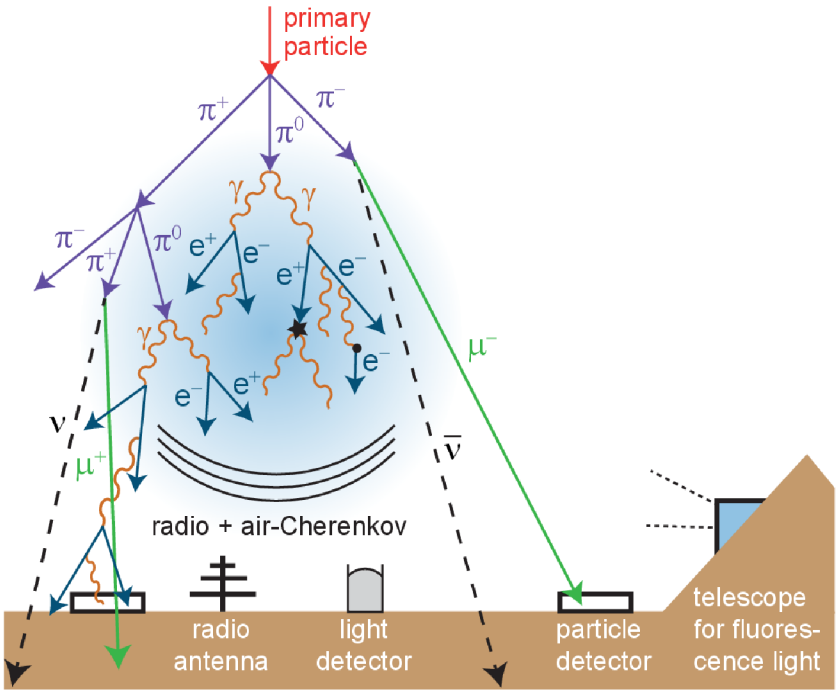

Figure 4 An illustration of an EAS. Primary cosmic particle may induce a cascade of secondary particles, such as pions, muons, neutrinos or fluorescent light. [5]

1.2.2. Surface detectors

Surface-based detectors , or scintillator detectors, detect the amount, or density of the secondary particles produced during an air shower once they reach the surface of the Earth. Timing of these measurements is crucial, as only one of these detectors provides very little information regarding the whole astrophysical event. Thus, an array of such detectors is used and the EAS is then reconstructed via information obtained by including and analyzing the data of all surface-based detectors involved in capturing the air shower. Because of the exceptionally low minute flux of UHECRs, one particle per square kilometer per year, a large array of such detectors is required to obtain any meaningful amount of data within a reasonable time frame. There are several possibilities in constructing aforementioned surface detectors. Methods utilized in PAO and TA observatories will be examined.

The surface detectors utilized in Telescope Array employ a plastic scintillator designed to produce faint UV to blue light upon interacting with ionizing radiation of the extensive air shower. The scintillators detecting charged particles are enclosed in metal sheets with photomultiplier tubes (PMTs) to increase the intensity of the produced light. The surface detectors are then placed in a grid containing 507 individual detectors spaced in distances of 1.2 km between each other. The surface detectors measure the timing, charge and spatial distribution of the particles. An image of one such unit is shown in figure 5.

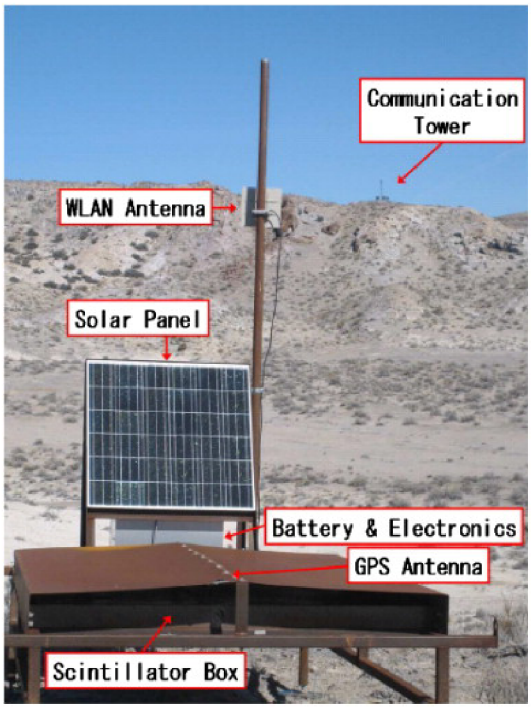

Figure 5 An image of a surface detector in TA, Utah. Several key components, including the scintillator box are highlighted. [6]

Surface detectors in the Pierre Auger Observatory utilize a different approach. These detectors are comprised of a 12 000 liter cylindrical tank of ultra-pure water (UPW). The ultra-pure water, that is water with any kind of organic material or additional gases removed, serves as a medium for secondary particles of an EAS. Upon reaching the UPW tanks, Cherenkov radiation is produced, as the particles themselves travel at a velocity higher that of the speed of light in such medium. A photomultiplier tube is used to increase the intensity of the produced Cherenkov light. The tanks provide a height of 1.6 meters and so far more than 1400 of them were deployed in the Argentinian desert. An image of one such UPW tank can be seen in figure 6. [7]

Figure 6 | An image of a surface detector in Pierre Auger Observatory in Argentina. [8]

Surface detectors provide valuable information regarding cosmic rays, concerning their energy, composition and origin. However, due to the low minute flux of cosmic radiation of incredible energies, a plethora of such detectors has to be utilized to obtain sufficient data. Surface detectors are best used when combined with other methods of detection UHECRs, for example fluorescence detectors.

1.2.3. Fluorescence detectors

During an extensive air shower, secondary particles of the cosmic ray can interact with nitrogen atoms comprising Earth's atmosphere. Electrons in nitrogen atoms may rise to an excited state, and upon de-excitation emit a photon. This subsequent photon falls in the UV range of the electromagnetic spectrum. UHECRs of incredible energies produce enormous showers of detectable UV light from mentioned emission. This UV light can then be detected using ground-based fluorescent optical telescopes. Note that Cherenkov telescopes also detect UV light, but the photons are formed due to the Cherenkov effect when secondary particles travel at speeds higher that the speed of light in our atmosphere (or water mentioned in Section 1.2.2). This process is widely used when detecting cosmic rays of energies in the TeV (10^{12}) range. UHECRs shower detection is dominated by the use of fluorescent telescopes. Because of the exceptionally low minute flux of UHECRs, an array of such telescopes is required obtain meaningful amount of data.

Such fluorescent telescope utilize a large area comprised of curved mirrors to reflect the aforementioned UV photons and focus them into a set of photomultiplier tubes, where the electrical signal obtained from the photoelectric effect on the cathode of the PMT is amplified by an order of several factors. PMTs are incredibly sensitive devices, so sufficient shielding is mandatory. Any additional electromagnetic radiation inevitably and irredeemably damages the PMTs, so the telescope can only operate on clear moonless night far from any excessive artificial light. The telescope has to be protected physically due to the nature of the location of observatories. Their placement in dry deserts may cause sand and dust buildup which has the potential to severely damage the electronics of the PMTs. Aerosols and natural humidity present in the air may hinder the detecting capabilities of the detector, but this issue is of relatively low concern due to the dry air in both Argentinian and American deserts in PAO and TA, respectively.

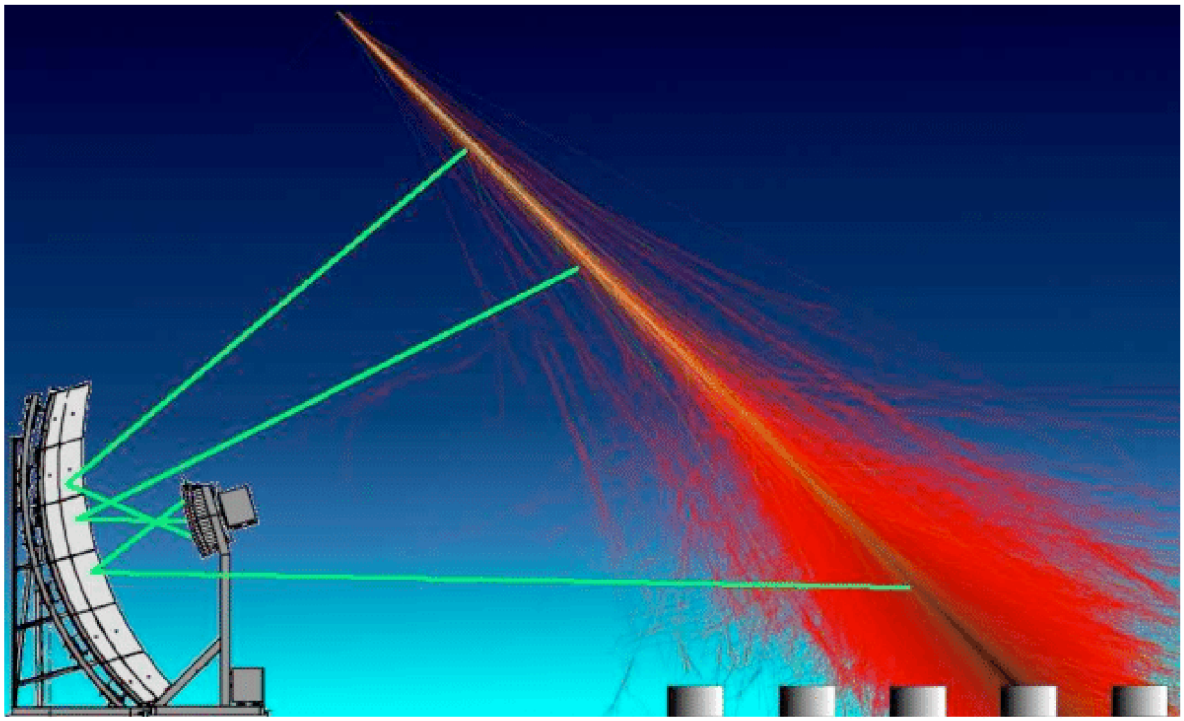

Figure 7 | A sketch of an air shower produced by a cosmic ray with a fluorescent telescope detecting UV radiation produced by the EAS. [9]

Fluorescence detectors provide valuable information concerning UHECRs. Utilizing such methods yields insight into both the energy and direction of the primary UHECR, allowing scientists to further investigate these rare energetic cosmic rays. To obtain any meaningful amount of data, a set of these detectors is required, as the reconstruction of the induced air shower is only possible upon analysis of the data of multiple involved telescopes. Fluorescent telescopes provide a powerful tool in studying high-energy cosmic radiation, but the most effective approach involves their combined utilization with other methods, such as surface-based detectors. An illustration of on such fluorescent telescope detecting UV light induced by an EAS is shown in figure 7.

1.3. FAST project

A project dedicated to studying UHECRs has to fulfill several criteria. Due to the extremely low minute flux of such energetic particles, the detection area has to encompass an immensely large surface area to be able to obtain any meaningful amount of data. Due to the enormous scale of the project, numerous detectors have to be deployed. By analyzing data from multiple measurements of the same astrophysical event, researchers can then adequately reconstruct the whole extensive air shower and its parameters, such as energy, particle composition of the primary ray and point of origin, or the trajectory of the particle.

One such project is the focus of this thesis. The Fluorescence Array of Single-pixel Telescopes (FAST) is a concept for a next-generation ground-based UHECRs observatory. The project utilizes telescopes detecting faint fluorescent UV light produced during an air shower. Taking into effect the enormous scale of the whole operation, having a large grid of economically viable and reliable detectors is mandatory for quality detection and analysis of primary cosmic rays and its properties. The FAST project offers just that, a large grid of affordable low-cost fluorescence detectors observing UHECRs.

A single FAST telescope consists of a matrix of four pixels observing a $30° \times 30°$ portion of the night sky, with an aperture area of ~ 1 m^2. Each pixel is equipped with a 200mm photomultiplier tube (PMT) to adequately amplify given signal. In total, on a single FAST telescope four such PMTs are present. The cost-effectiveness renders this design a competitive contender in the aspiration of planning and deployment of a new generation of UHECRs observatories. Currently, FAST telescopes are commissioned in Pierre Auger observatory (PAO) in Argentina and Telescope Array (TA) in Utah, U.S.A. [10]

However, its low cost comes at a prize of low geometric resolution. Its 2×2 matrix of four PMTs does not allow for any quality extensive air shower reconstruction. The single-pixel nature of the telescope prohibits any meaningful analysis by obtaining data from a single telescope. An array of said telescopes need be deployed. A cosmic ray of sufficient energy is capable of producing an air shower detectable by multiple telescopes, by analyzing measurements from multiple such detectors, researchers can then analyze and reconstruct the primary cosmic rays. Surface detectors present in both PAO and TA observatories serve as excellent detectors regarding the composition of secondary particles, mostly due to their impressive duty cycles. However these methods exhibit limited precision in measuring the energy of UHECRs. Thus, a combination of both surface and fluorescence detectors proves superior in proper detection of UHECRs.

Fluorescence detectors provide a calorimetric measurement regarding the air shower's energy. This is achieved by detection of the UV light produced by the excitation and subsequent de-excitation of nitrogen atoms in our atmosphere during the EAS. This provides information on a parameter indicative of the primary energy, X_{max}, denoted as depth of maximum development. While fluorescence detectors offer great accuracy in reading the energy of the UHECRs, they suffer from poor duty cycle (at least compared to surface detectors) and sub-optimal spatial coverage due to low geometric resolution. Thus, data from several FAST telescopes involved in the detection of the shower has to be taken into account. Energy readings from fluorescent telescopes can serve as a calibration method regarding energy measurements of their surface counterparts. This so called hybrid detection is employed successfully in both PAO and TA observatories. With this technique, both TA and PAO have measured energy spectrum up to 100 EeV. The thesis will examine data from one FAST telescope situated at the PAO site and three telescopes located on the TA site. The telescopes themselves are shown in figure 8 and 9, respectively. [11]

Figure 8 An image of the PAO FAST telescope examined in this thesis (left). Another FAST telescope (right) is further currently under construction.

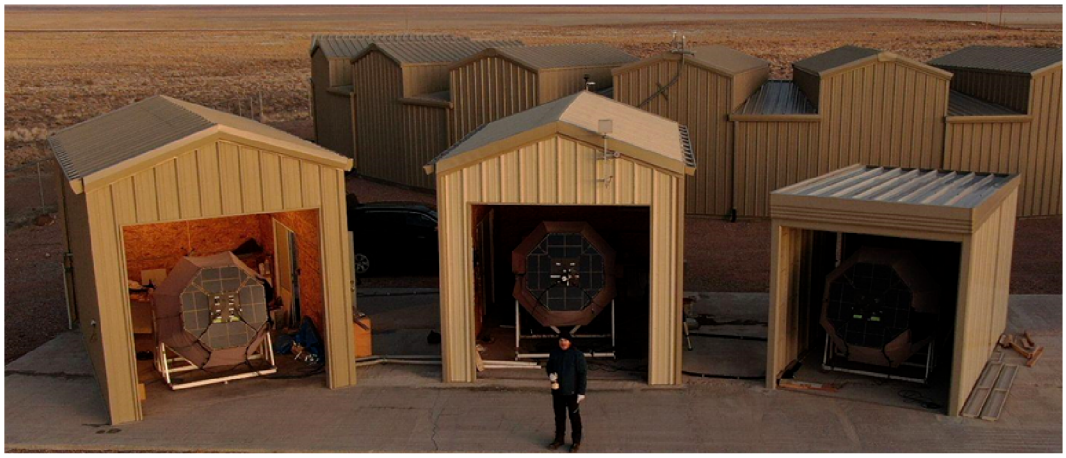

Figure 9 An image of the three TA FAST telescopes examined in this thesis.

1.4. FAST telescope design

The design goal of the individual FAST telescope is set as to achieve an optical system with at least a 1 m^2 collecting aperture area and a $\sim 30° \times 30°$ field-of-view (FOV). The telescope then focuses incident UV light on to a grid comprised of a matrix of 2×2 200mm PMTs capable of amplifying the optical signal for adequate data analysis. Additionally, due to the large number of required deployed telescopes, both low cost and easy maintenance are emphasized in the design of a FAST. telescope. This requires the minimization of optical elements present in the telescope itself. Both refractive and reflective options were considered in the initial stages of development. These option are further described in the following sections 1.4.1 and 1.4.2, respectively.

1.4.1. Refractive design

A proposed refractive design consisted of a series of Fresnel lenses. This draft would be of lowest possible cost. Unfortunately, largest commercially available Fresnel lenses present large off-axis aberration, rendering them unsuitable for wide angle optical telescope such as that of the FAST project. Furthermore, these Fresnel lenses offer only a ~ 0.36 m^2 of collecting area, which does not fulfill the set criteria of the FAST project of 1 m^2 collecting aperture area. Additionally, limitations in regard to the field of view of the optical system present a sizeable downside of this proposed design.

It was however tested in the Black Rock Mesa (BRM) of the Telescope Array as a proof-of-concept detector in 2014. Two 1m long Fresnel lenses focused light onto a single PMT. The test proved the detector to be viable, as the PMT succeeded in observing laser flashes up to distance of 21 km, as well as 16 candidates of UHECRs induced air shower. Utilizing the sample of coincident events, this design proved successful in detecting cosmic rays in the range of 10^{19} eV. An illustration of this design can be found in figure 10 and a the PMT camera in such design can be seen in figure 11.

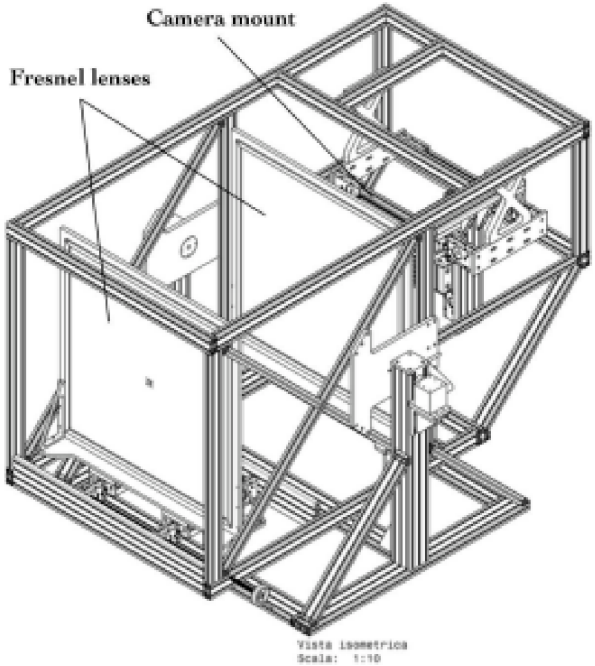

Figure 10 An illustration of the refractive design of the FAST telescope including two Fresnel lenses. [12]

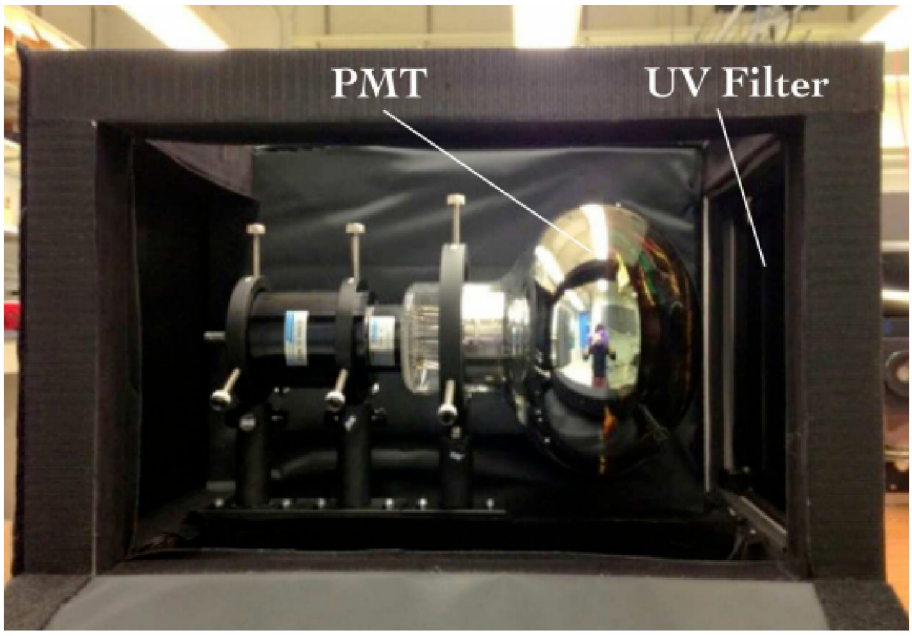

Figure 11 An image of the PMT camera with a UV filter present in the refractive solution. [12]

1.4.2. Reflective and optimal design

Due to the drawbacks of the refractive design, a reflective design was proposed. The simplest solution would consist of a single large spherical mirror reflecting the UV light onto an aperture at its radius of curvature. This design is called a Schmidt camera. An aspherical corrector plate is often utilized to limit on-axis aberrations. Such design is nevertheless only suitable for low FOV applications, unlike the requirements of the FAST project. To follow the said criteria, a lenseless Schmidt solution lacking the corrector plate can be employed.

The optimal design of the FAST telescope utilizes a Schmidt type optical system, with several differentiating factors altered. One such typical design utilizes a corrector plate located at the aperture, regulating the effect of coma, astigmatism and off-axis aberration. However these optical defects do not impede the functionality of the telescope itself, and thus can be, for the most part, ignored, due to the granular shape of the the PMT camera grid present at the entrance aperture. This allows the telescope point spread function, a parameter characterizing the spatial light distribution, to be relaxed.

The prototype of one such FAST telescope can be seen in figure 12. The aperture sits at a height of 1.24 meters at a distance of 1 m to a 1.6 single primary spherical mirror. This proposed solution fulfills the requirements of the FAST project, a 1 m^2 collecting aperture area and a $\sim 30° \times 30°$ field-of-view (FOV) of the telescope. Furthermore, figure 13 shows optical ray tracing simulations concerning on-axis (blue) and off-axis (green) rays.

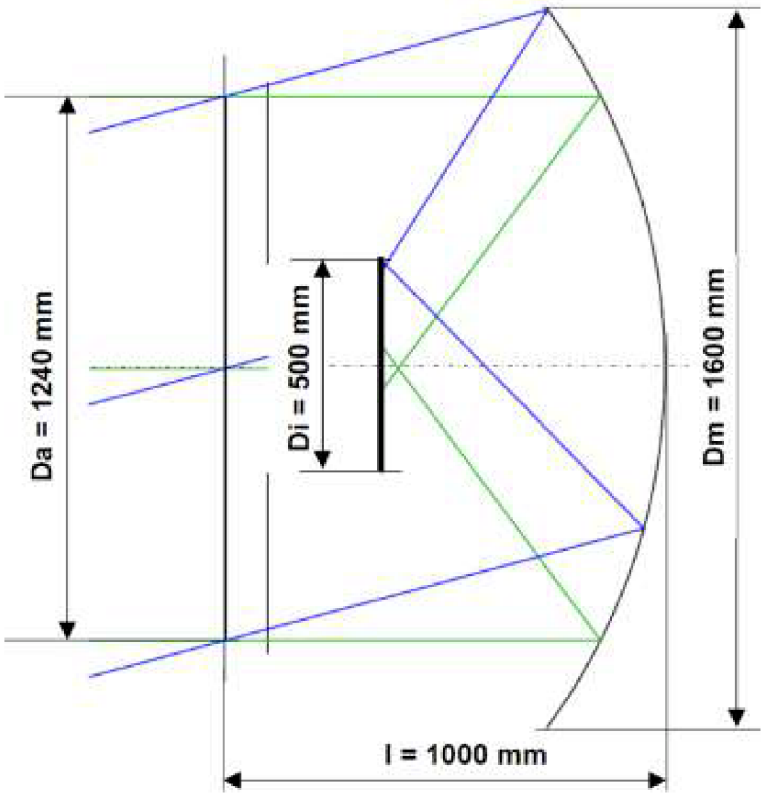

Figure 12 The dimensions of the FAST prototype telescope's optical system. D_a is the face-to-face size of the octagonal telescope aperture, D_i is the side length of the square camera box, D_m is the diameter of the primary mirror, and l is the mirror-aperture distance. Taken from [10]

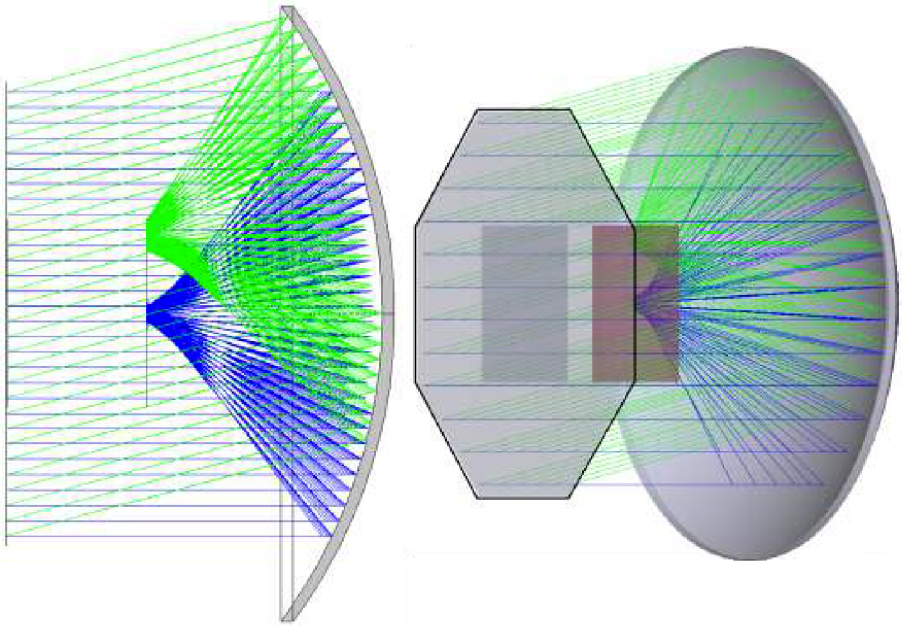

Figure 13 2D (left) and 3D (right) ray-tracing simulation for optical performance of parallel on-axis rays (blue) and off-axis rays (green). [10]

Note that in figure 13, on-axis optical rays are focused directly onto the very center of the telescope. However, the center grid is comprised of four 200mm PMTs spaced in a 2×2 matrix, and thus no PMT would be able to detect light reflecting directly into the center of the aperture grid. To prevent that, a mirror pyramid is placed onto the central part to further reflect light onto the PMTs. On the contrary, light reflected on the very edge of the aperture during off-axis ray reflections will not be detected as well. To diminish signal loss, a mirror band is placed on the edge of the aperture, reflecting light from the sides toward the four PMTs. The camera box with the mirror pyramid and band can be seen in figure 14.

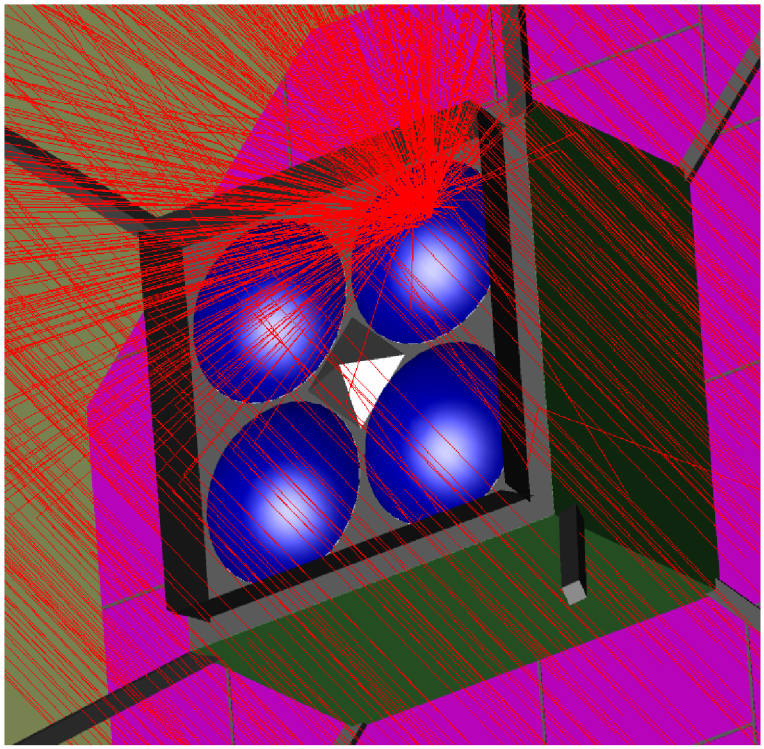

Figure 14 A ray tracing image showing the aperture grid containing the four 200mm PMTs with the mirror pyramid in the centre and mirror band located on the edges of the grid. [11]

The most cost-effective and straightforward approach to constructing a 1.6m diameter spherical mirror involves utilizing a segmented design. A single spherical mirror would be optimal, however construction of such a large mirror is not feasible, both economically and technologically. The optimal FAST telescope design utilized a primary circular mirror enclosed with 8 side mirrors, in a "petal"like structure. The arrangement of the mirrors was optimized to achieve highest efficiency concerning the reflective area of the telescope. Several stages of the design can be seen in figure 15. The very first design consisted of a primary mirror with 6 side mirrors overlapping each other to diminish dead spots between the individual mirrors, as can be seen in figure 15(a). Although in this optical configuration, the curvature of the side mirrors would have to be adjusted to comply with the telescope requirements. To further diminish the dead space, the side mirrors can be cut and placed directly next to each other, as shown in figure 15(b). This design is more efficient, however still entails a large dead space. Another proposed solution consisted of cutting the mirrors even further and employing a hexagonal central mirror as depicted in figure 15(c). This solution however decreases the reflecting area of the telescope and thus another design was finally selected. The optimal configuration is one central circular mirror surrounded by 8 "petal"shaped mirrors, as shown in figure 15(d).

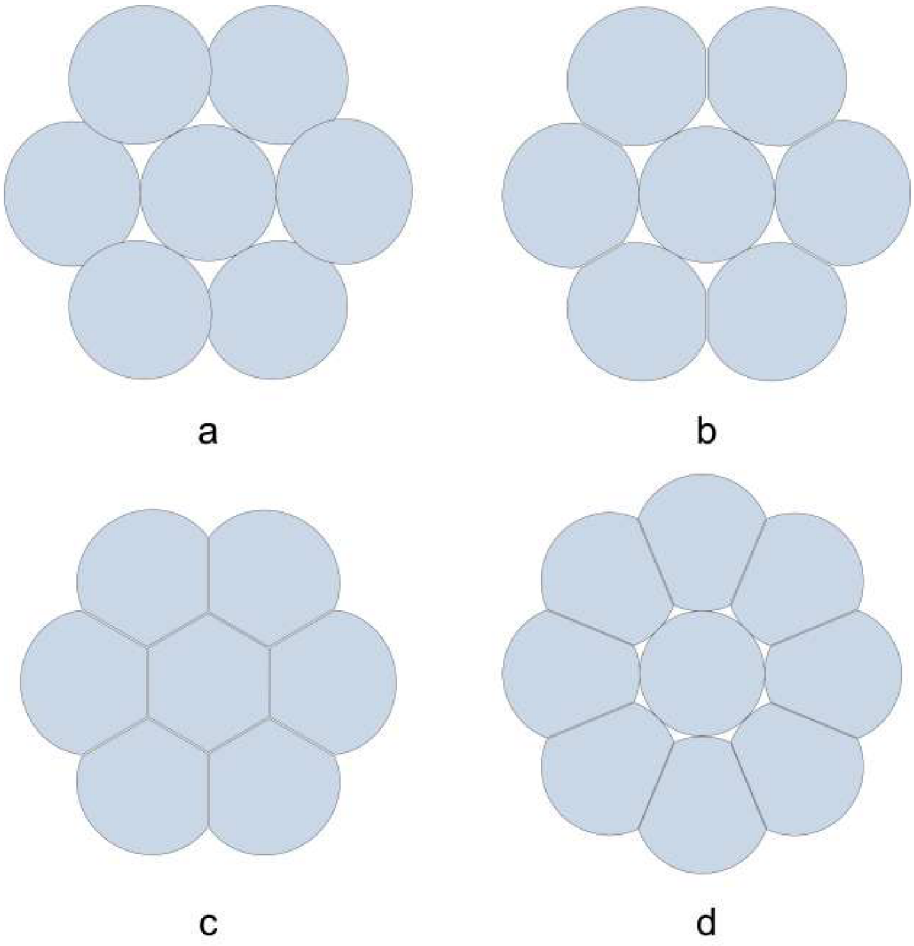

Figure 15 | Four original designs of the FAST telescope. [11]

The final design offers 2.39 m^2 of reflecting area. The individual mirrors are produced in the Joint Laboratory of Optics of the Palacky University and the Institute of Physics of the Academy of Sciences of the Czech Republic. The custom substrate of the mirrors is a borosilicate glass sufficient with regard to both optical and mechanical quality. The spectral reflectance of the mirror segment is showcased in figure 16(blue). The telescope will observe UV light of the extensive air shower, and thus only the wavelength within the range of 260 nm and 420 nm is shown. The mirror coating offers satisfactory reflectivity within the required UV range with mostly 70 to 90 %.

Additionally, a UV filter is installed at the aperture of the telescope, with the intent to reduce parasitic environmental night sky background light. Furthermore, the filter serves as a mechanical barrier protecting the optical components of the FAST telescope from sand and dust buildup of dry air Argentinean and American deserts. ZWB3 filter manufactured by Shijiazhuang Zeyuan Opticswas was utilized. Its spectral transmittance is displayed in figure 16(red). The final collecting aperture area of the telescope is 1 m^2.

The support structure of the telescope was entirely built from commercially available aluminum profiles. This allows a straightforward assembly and disassembly and furthermore, due to the relatively light weight of the profiles, easy and low-cost transportation. The support structure of the telescope allows several discrete options regarding the elevation of the telescope. These elevation values are 0°, 15°, 30° and 45°. The telescope is then finally enclosed in a protective shroud. The final FAST telescope including the shroud can be seen in figure 17.

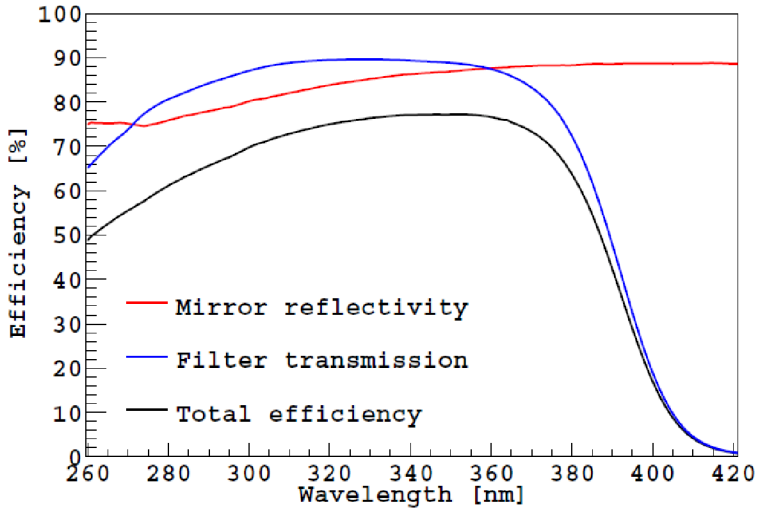

Figure 16 Spectral reflectivity of the FAST telescope borosilicate glass mirror (red) along with UV filter transmittance (blue) and total efficiency of the optical setup (black). [11]

Figure 17 An image of the FAST telescope, including the aluminum structure, octagonal UV filter and a protective shroud. [11]

1.5. Photomultiplier tubes

Photomultiplier tubes are extremely sensitive light detectors that amplify incident optical signal and convert it into an electrical signal. This is done firstly by employing the external photoelectric effect, as the incident light is absorbed in the cathode. As the primary photon carries enough energy causing an emission of an electron out of the material of the photocathode, the electron is then focused by an electrode towards a series of anodes with assigned ascending voltage. The series of anodes, called dynodes act as a final multiplier for the electrical signal, as the electrons are accelerated due to the electric field and cause secondary emissions at the individual dynodes. The electrons are at last focused onto a single final anode, where the signal can be measured.

The FAST telescope utilizes a PMT produced by Hamamatsu (mod. R5912-03). This PMT offers adequate spectral response in the range of 300 to 650 nm, well within the required UV portion of the electromagnetic spectrum for the faint fluorescent light produced by the extensive air shower. The individual PMT is 8 inches long, or $\sim$ 200 mm. The incident light travels through a borosilicate glass window suitable for transmittance of UV electromagnetic radiation during the EAS. Spectral characteristics of the borosilicate window can be seen in figure 19. The interior of the PMT consists of a bialkali photocathode and a series of 10 box and linear-focused dynodes. A graph visualizing the quantum efficiency of the PMT can is then shown in figure 20.

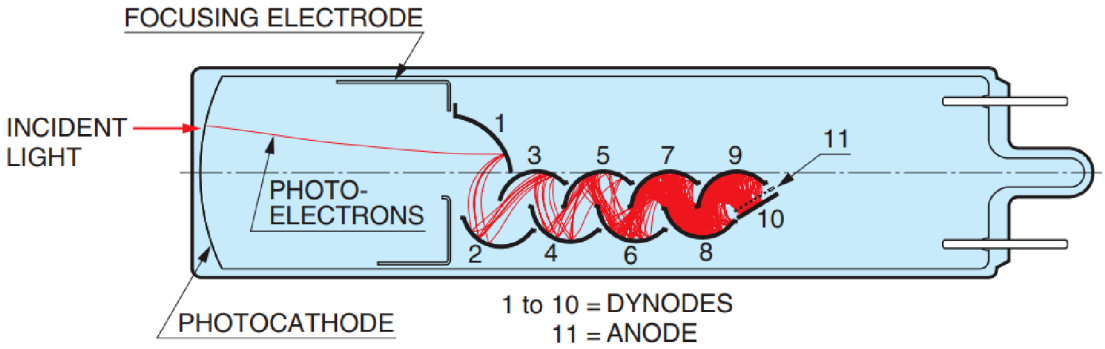

Figure 18 | A schematic of a box and linear-focused PMT. [13]

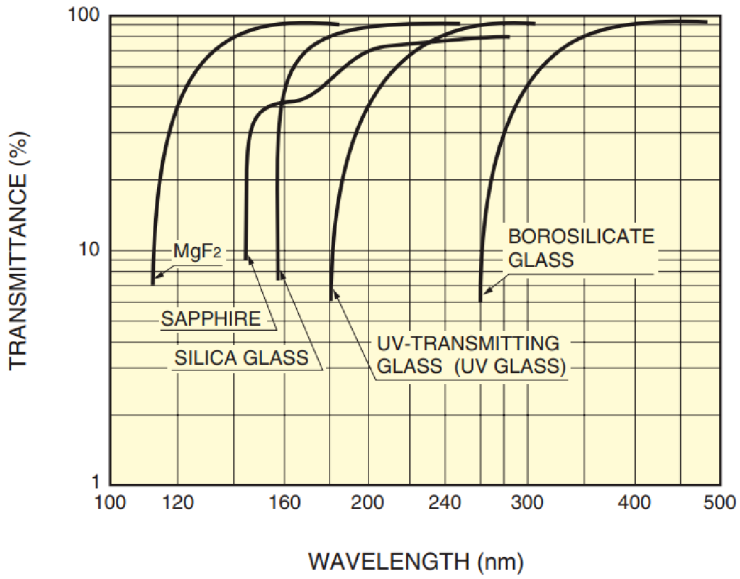

Figure 19 | Spectral transmittance of various materials used in PMT windows. The windows of PMTs utilized in the FAST telescope are comprised of borosilicate glass. [13]

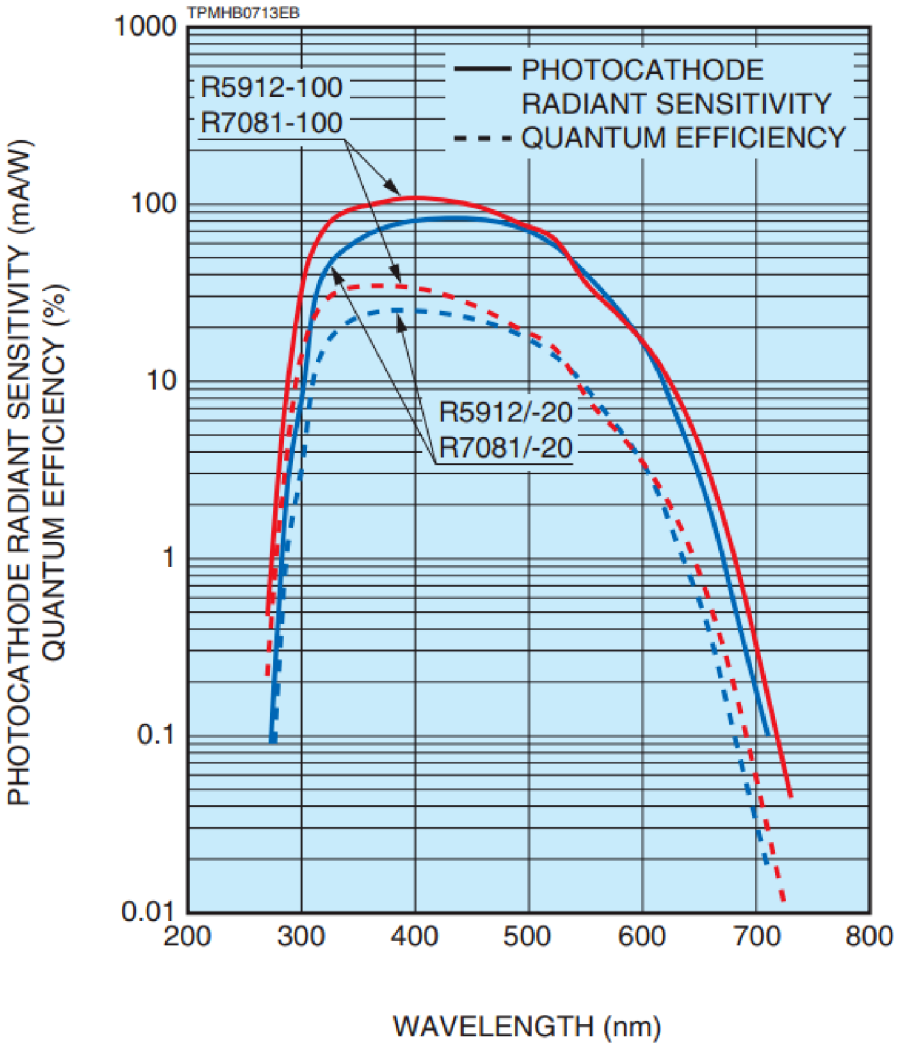

Figure 20 A graph displaying the relation between quantum efficiency of the FAST telescopes' PMTs and wavelength of the incident light. FAST telescopes measure light in the UV range of the electromagnetic spectrum [13]

1.5.1. Time dependency

It is important to ensure stability of the PMT signal with respect to time. Variations over small time horizon (hours) is called a drift, while instability over a large amount of time (thousands or tens of thousand of hours) is called life characteristic. Drift characteristics of the PMT can be found in figure 21. Drift per unit of time improves with longer operating time. It is advised to warm-up the PMT 30 to 60 minutes before usage, so the drift can stabilize at acceptable values. As the drift itself behaves in a relatively stable manner, other variations including life characteristics generally depends on other factors, such as the ratio of secondary emission, voltage, or temperature.

Figure 22 displays the presumed life characteristic of FAST telescope PMTs. Significant signal variability can be observed with operating time increasing to the range of thousand operated hours. This is crucial in order to establish long-term time stability of PMTs during UHECRs measurements. Over the period of several years, the relative anode sensitivity might interfere with the functionality of the telescope and impede the detection process.

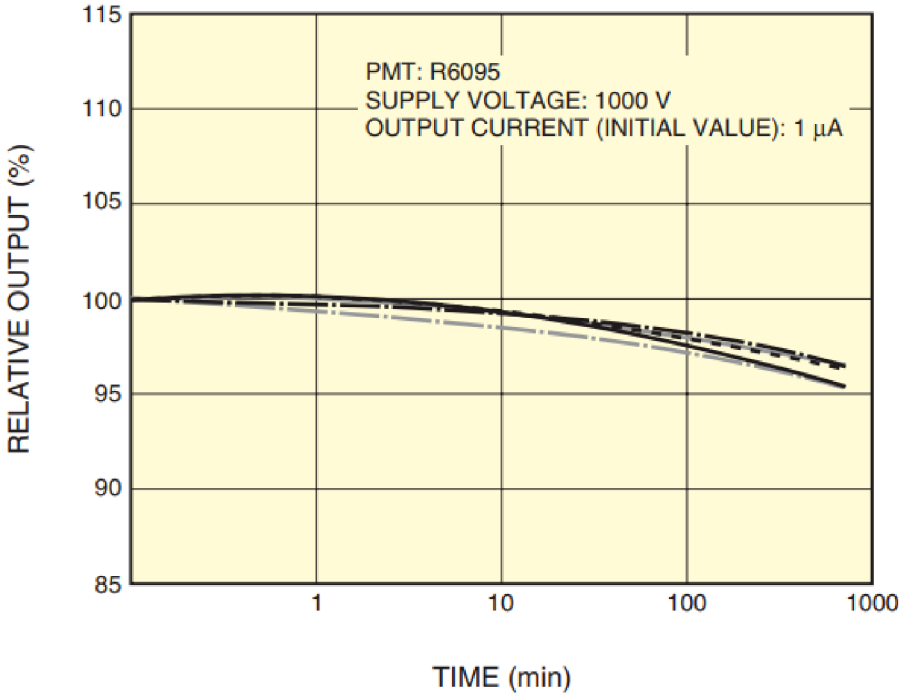

Figure 21 A graph visualizing the variability of PMT signal in a small time horizons, called drift. [13]

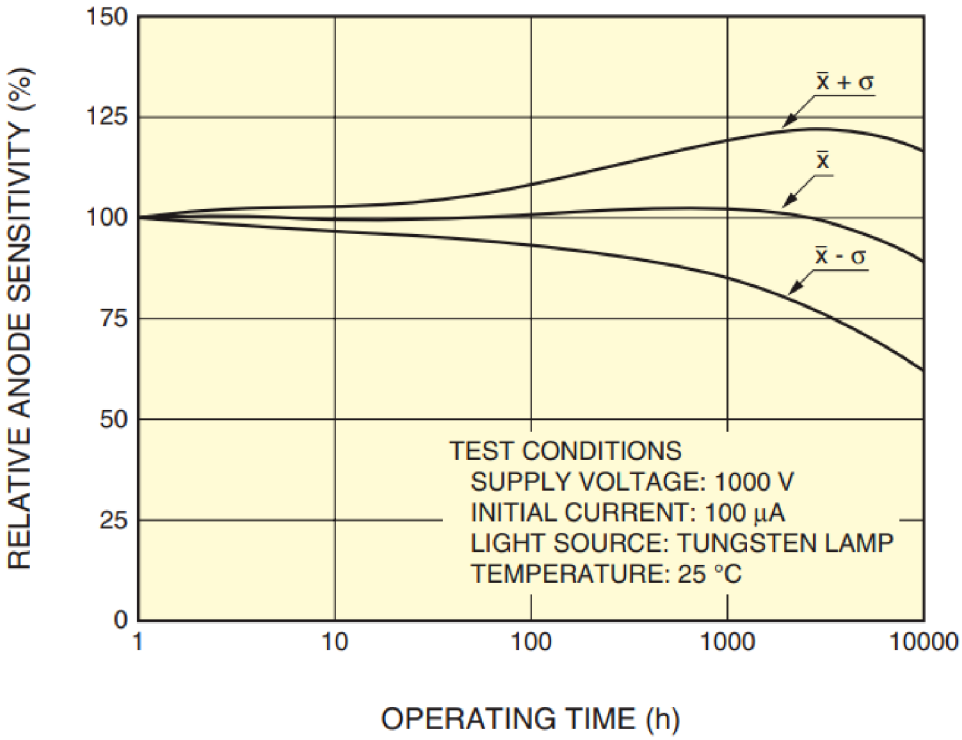

Figure 22 A graph visualizing the variability of PMT signal during a long time interval, called life characteristic. [13]

1.5.2. Temperature dependency

Sufficient temperature stability is required for precise concrete measurements in the extreme weather conditions of both the Argentinian and American deserts. The drastic temperature differences may results in significant variability of the PMT signal which has to be taken into account and appropriately adjusted for. Temperature regulation, or effective cooling can be considered as an option to reduce the effect of environment towards the PMTs. Otherwise, different comparative methods are required for adequate temperature stability.

The effect of temperature on PMTs can be divided into several sections. Photo-cathode sensitivity is of primary concern when examining signal reliability of PMTs. The sensitivity depends foremost on the wavelength of light. The relation between anode sensitivity and wavelength of incident light is provided by the manufacturer in figure 23. The sensitivity of bialkali photo-cathodes remain constant at the UV portion of the electromagnetic spectrum, at a value of $\sim$ -0.4 % per °C. In other words, the sensitivity of the anode decreases by 0.4 % per every °C.

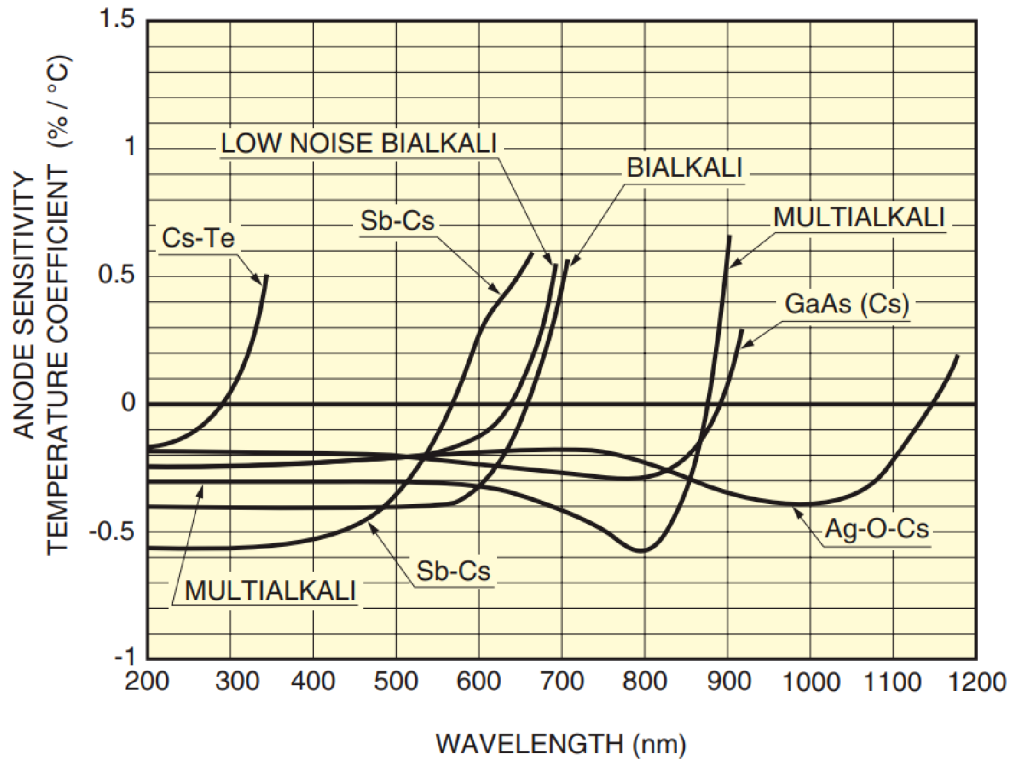

Figure 23 The relation between anode sensitivity and the wavelength of incident light. Bialkali photo-cathodes are of primary concern, as the PMTs employed on a FAST telescope utilize such photo-cathodes. [13]

Another important factor to consider is the saturation current of the photo-cathodes. The detection sensitivity of PMTs may be significantly impeded by the loss of output linearity, which is a necessary requirement for achieving high levels of detection accuracy. This loss of output linearity may become apparent particularly at low temperatures, as the increase of photo-cathode surface resistance can cause saturation at relatively low currents, inducing aforementioned loss of output linearity. This effect is further enhanced in bialkali photocathodes, so sufficient care is mandatory for proper function of PMTs. The relationship between saturation current and temperature is shown in figure 24.

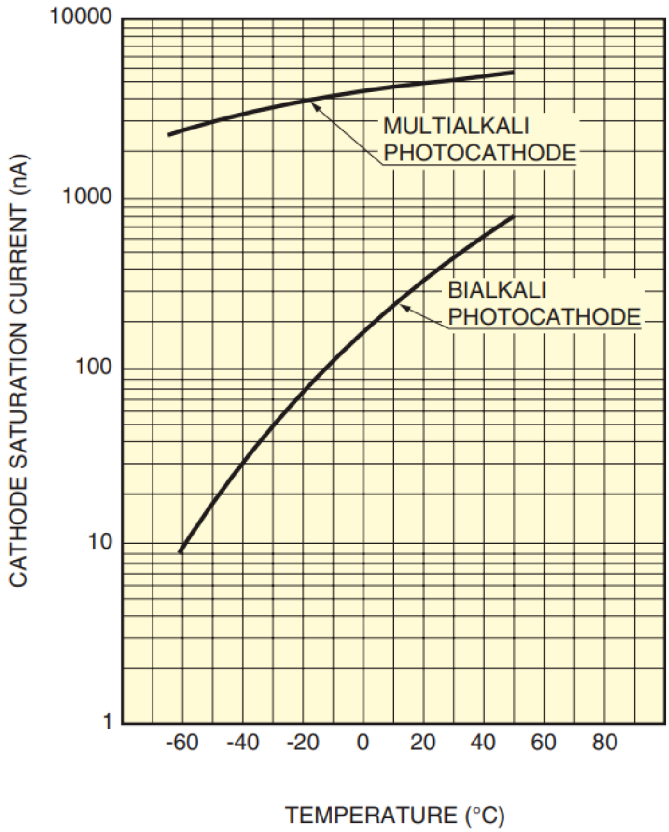

Figure 24 The relation between saturation current and temperature of Hamamatsu PMTs. [13]

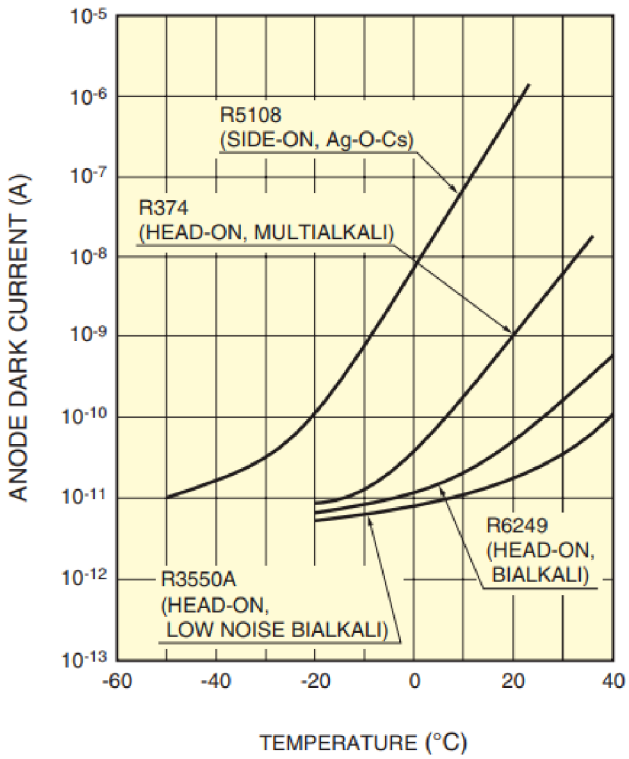

Figure 25 The relation between dark current and temperature. [13]

Another important factor to consider is the dark current of the photocathode. Due to the need of a small energy gap, so electrons can be released efficiently upon absorption of incident light, significant amount of dark current can be present primarily at low temperatures. This means that the dark current itself is heavily dependant on ambient temperature. Graph displaying such relation is shown in figure 25. One particular solution to removing the effect of dark current is the cooling of PMTs, or the use of low-noise bialkali photo-cathodes. Otherwise, this may become an important factor to contemplate upon examining the PMT signal with respect to temperature during the measurements.

During the first full-scale test of the FAST telescope prototype in Telescope Array, Utah, U.S.A, a signal strength dependency on temperature was measured. The results and subsequent fitted relation is shown in figure 26. These finding are in accordance with the manufacturer's documentation as showcased primarily in figure 23.

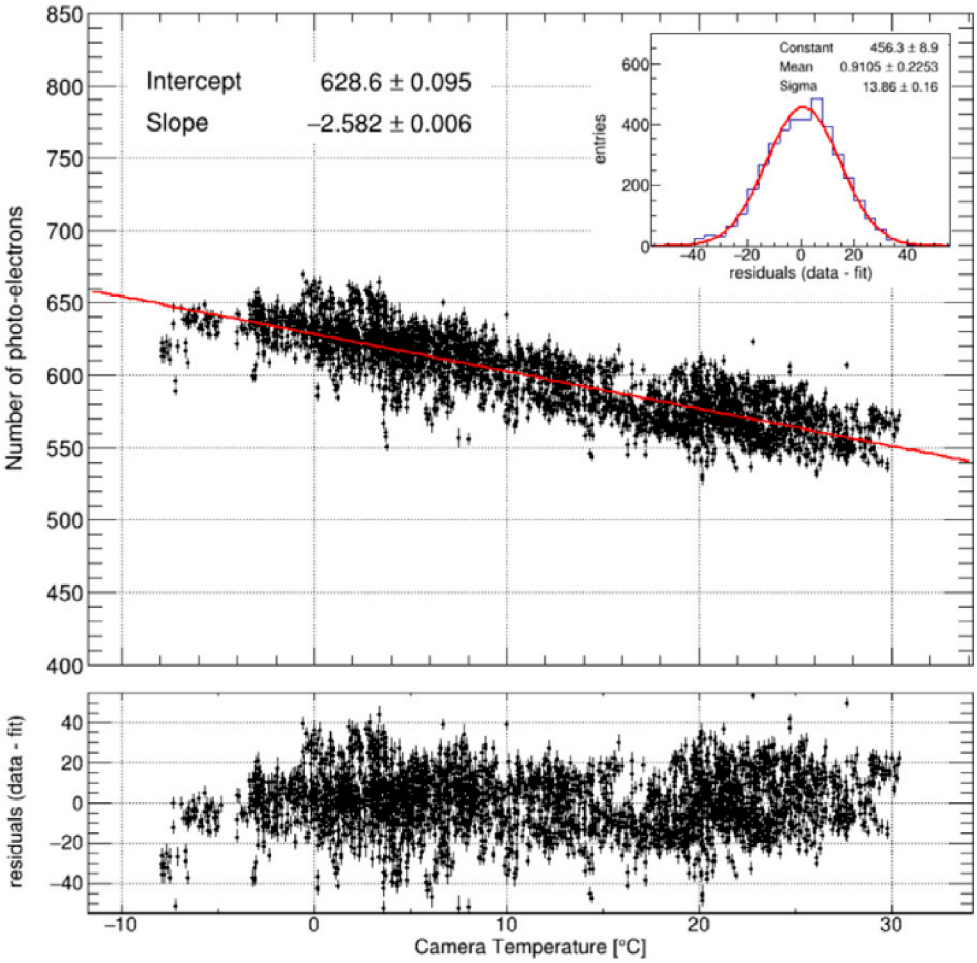

Figure 26 The fitted relationship between the strength of PMT signal (measured in the number of photo-electrons) and ambient temperature as measured on the TA site. The residuals of the fit are shown in the bottom panel. [11]

1.6. Data acquisition

The entire FAST electronics chain is composed from commercially available components. The camera box consists of four 200mm PMTs (mod. R5912-03, Hamamatsu) organized in a 2×2 matrix. The PMTs are powered from an AC-coupled active base (mod. E7694-01, Hamamatsu) with maximum operational voltage of $\sim$ 2600 V. The ideal operational voltage is $\sim$ 1000 V. The voltage is conveyed by a NIM-mounted module (mod. N1470, CAEN), and the signal emanating from the base undergoes transmission through a low-pass (LP) filter (mod. CLPFL-0015, Crystek) to eliminate any high-frequency noise above 15 MHz. The signal then travels through an amplifier (mod. 777, Phillips Scientific). A Fast Analog-to-Digital Converter (FADC) (mod. SIS3316, Struck Innovative Systeme) is located in a VME crate, alongside a GPS module (mod. GPS2092, Hytec) and a single-board PC (mod. V97865, GE Intelligent Platforms) responsible for the operation of the Data Acquisition (DAQ) software. The schematic of the electronics for a single PMT is displayed in figure 27.

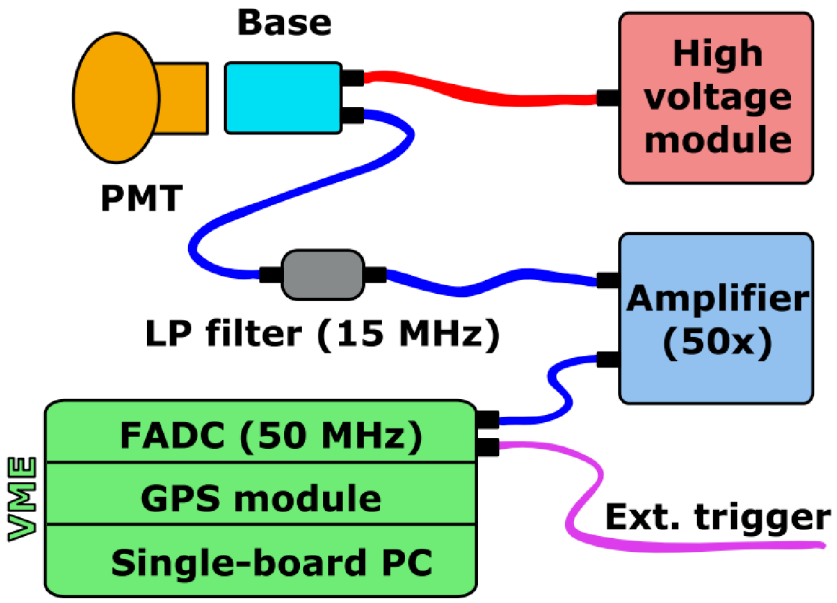

Figure 27 | Schematics of the FAST electronics chain for a single PMT. [11]

1.6.1. Environmental conditions

A single individual FAST telescope is provided with a number of detectors capable of monitoring the environmental conditions both inside and outside the FAST telescope hut. Detectors of temperature, humidity, light, pressure are present. Furthermore, every FAST telescope is equipped with detectors monitoring the status of the shutter of the FAST hut. To monitor indoor and outdoor temperatures, as well as the temperature of the rack case, multiple temperature sensors (mod. DS18B20+, Dallas) are installed. Additionally, the FAST camera box is equipped with the same sensor, albeit in a waterproof case. An integrated sensor that measures temperature, humidity, and pressure (mod. BME280, Bosch) is located on the aluminum profile that supports the telescope's optical elements. A Raspberry Pi 4 (RPi4) computer serves as the basis for the readout system. Both the sensors and their respective locations are present in a compilation of images found in figure 28.

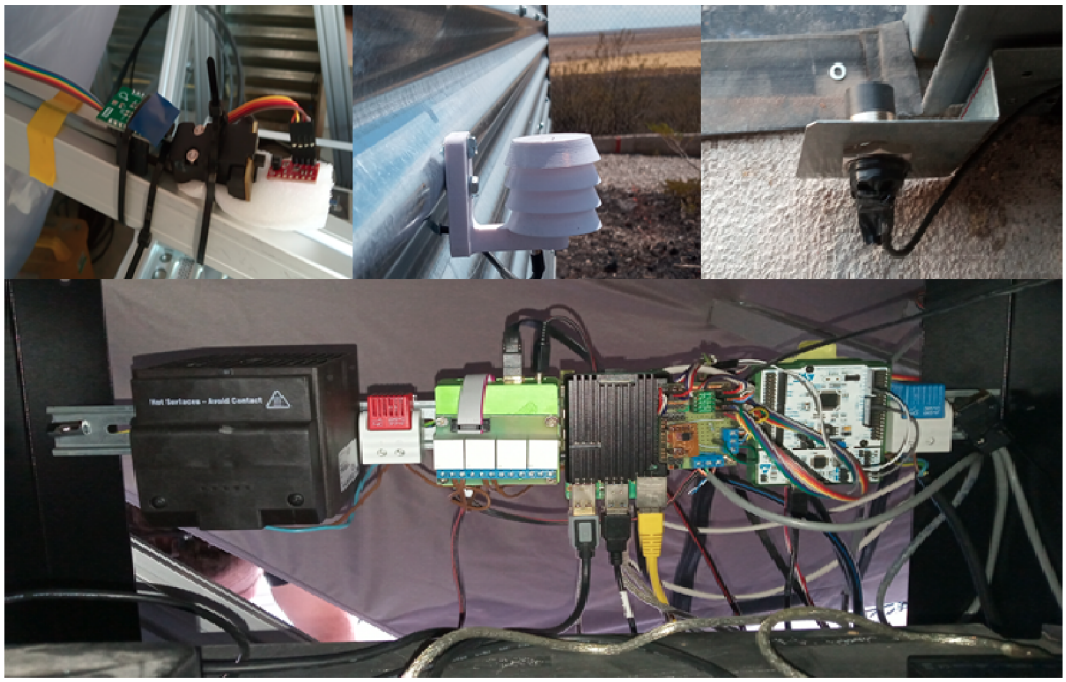

Figure 28 Sensor images and their respective locations. An indoor Dallas temperature sensor with a Bosh combined sensor (top left), outdoor Dallas temperature (top centre), shutter sensor (top right) and the electronics chain including the RPi4 computer and a Dallas rack case temperature sensor (bottom) can be seen. Taken from an internal presentation of the FAST collaboration.

1.6.2. UV LED calibration

Calibration of all PMTs present on a FAST telescope is mandatory for proper data analysis. Before deployment, the gain of the individual FAST PMTs is measured with respect to its corresponding voltage level. A fit analysis was performed on the measurements obtained within a chosen high voltage range. The resulting fit provides a calibration constant that can be utilized for further analysis. Initially, the intention was to standardize the gain across all PMTs. However, variations in spectral responses were observed, with some PMTs displaying higher or lower responses than others. Consequently, a unique calibration constant was assigned to each PMT. Additionally, it is necessary to recalculate the calibration constants periodically as their values are prone to change over time. The calibration measurements were performed on all PMTs included on both the PAO and TA sites. Further information involving the calibration constants regarding the individual PMTs is present in Section 2.1.

A UV LED flasher (RLT365-10E) is permanently installed in the central mirror of one PAO and at all three deployed TA FAST telescopes. The location with respect to the telescope in shown in figure 29. The flasher serves as another calibration method. It radiates at the UV portion of the electromagnetic spectrum, with peak wavelength of 365 nm at 25 °C with operating temperature range from -30 °C to +85 °C [14]. Dedicated UV LED measurements are conducted at the beginning and at the end of each observation run, called a shift. A micro-controller (STM32F411) is employed to operate the UV LED flasher. The UV LED flasher itself is not equipped with any means of temperature regulation, and thus is subject to a degree of variability in the produced UV radiation. Any temperature variance directly results in a shift of the emitted UV spectrum and thus can affect the spectral response of the both the optical elements and individual PMTs located in a FAST telescope. The relationship between temperature and peak wavelength of the spectrum is provided by the manufacturer of the UV LED flasher and is shown in figure 30. Furthermore, the amount of light emitted can be subject to a degree of temperature dependency as well. This can then significantly impact measurements conducted throughout various seasons and a broad temperature range. Such relationship is further shown in figure 31.

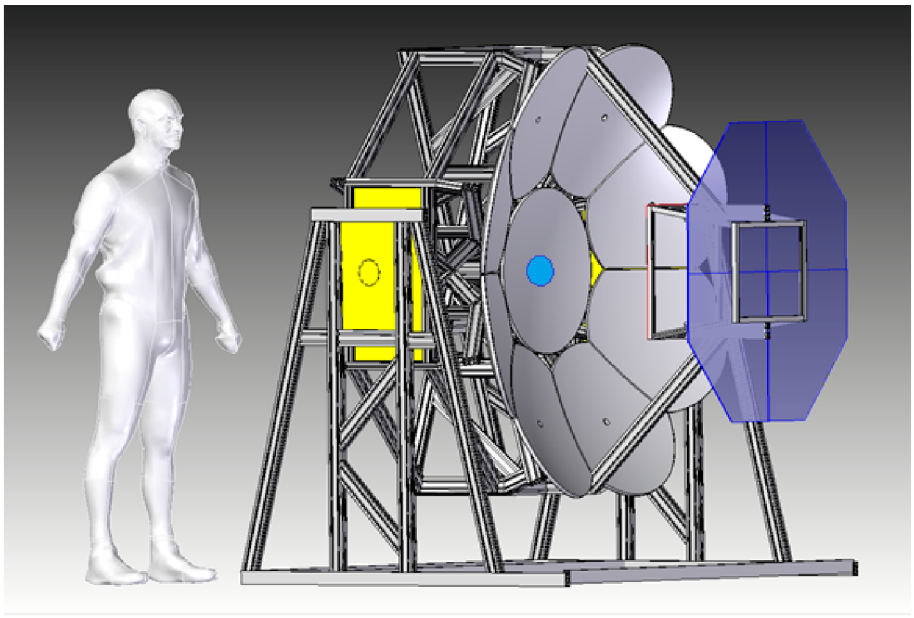

Figure 29 Location of the UV LED flasher (blue dot) on a central circular mirror of the FAST telescope. Edited from [12]

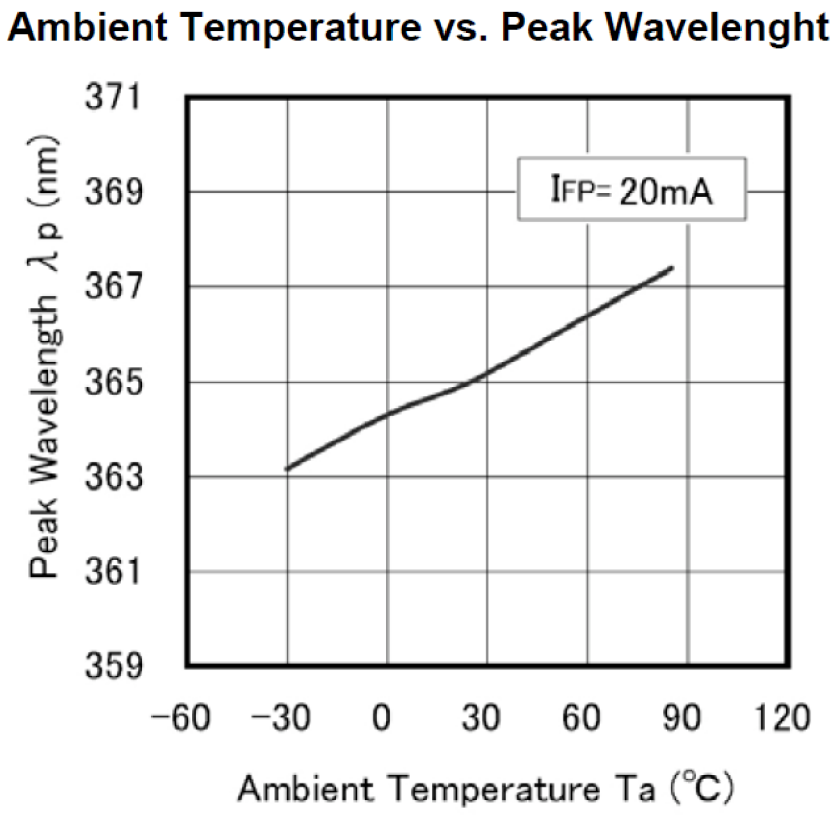

Figure 30 Relation between ambient temperature and the peak wavelength of the UV light emitted by the UV LED flasher. [14]

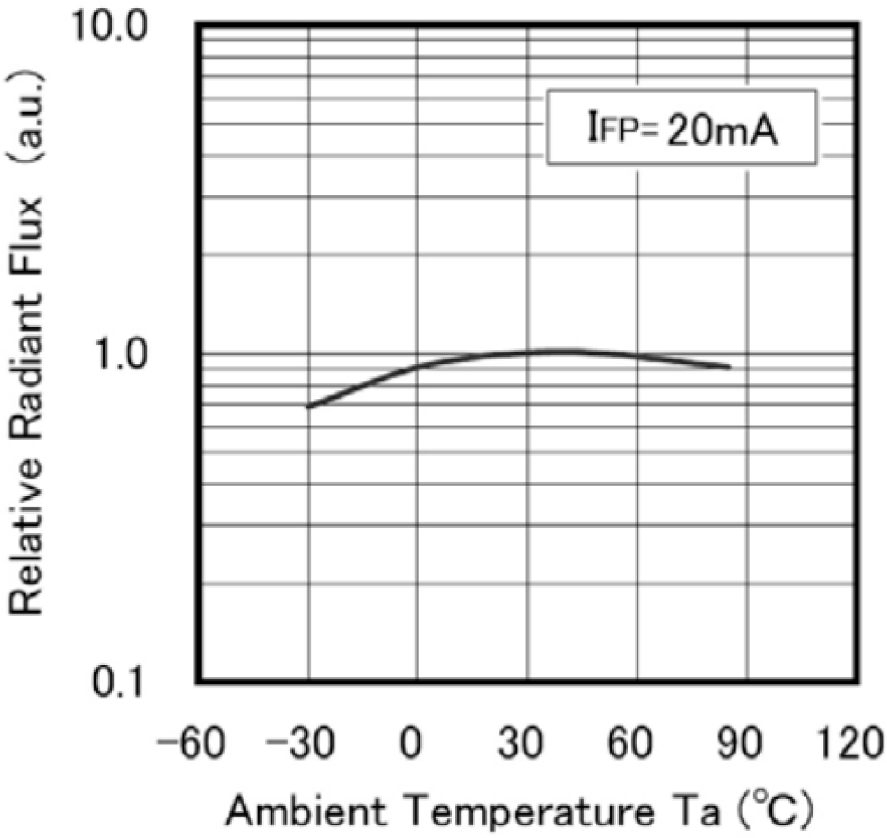

Figure 31 Relationship between ambient temperature and the relative radiant flux of the UV LED flasher. [14]

Temperature fluctuations affecting the UV LED flasher can cause a shift in the emitted light wavelength onto the PMTs, potentially altering their efficiency. This is due to several reasons. As shown before, the borosilicate glass of the PMT windows exhibits a degree of wavelength dependency. This is also true to the spectral sensitivity of the photo-cathode. This is significant because the wavelength of the emitted UV light is temperature-dependent as shown in figure 30. Secondly, ambient temperature also impacts both the saturation and dark current of the PMT. Additionally, significant temperature change will also impact the radiant flux of the flasher. All these effect should however affect all the four PMTs present in a FAST telescope equally. In addition, the spatial distribution of emitted light has to be examined. Relative radiant intensity with respect to direction of the flasher, or rotational angle, is shown in figure 32. Additionally, a photo of the UV LED flasher is present in figure 33.

By comparing the individual values of the calibration measurements, through a process called relative calibration, these effect should, in theory, be bypassed. This is not the case when examining the absolute values of the PMT signal, in a process denoted as absolute calibration. Both methods can provide valuable insight regarding the stability and reliability of PMTs located on the telescopes. This is mandatory to ensure meaningful results from UHECRs observational detection. This thesis furthermore examines both absolute and relative calibration of a single FAST telescope located in the Pierre Auger Observatory and three telescopes located in the Telescope Array. An infrared image of all examined telescopes is shown in figure 34.

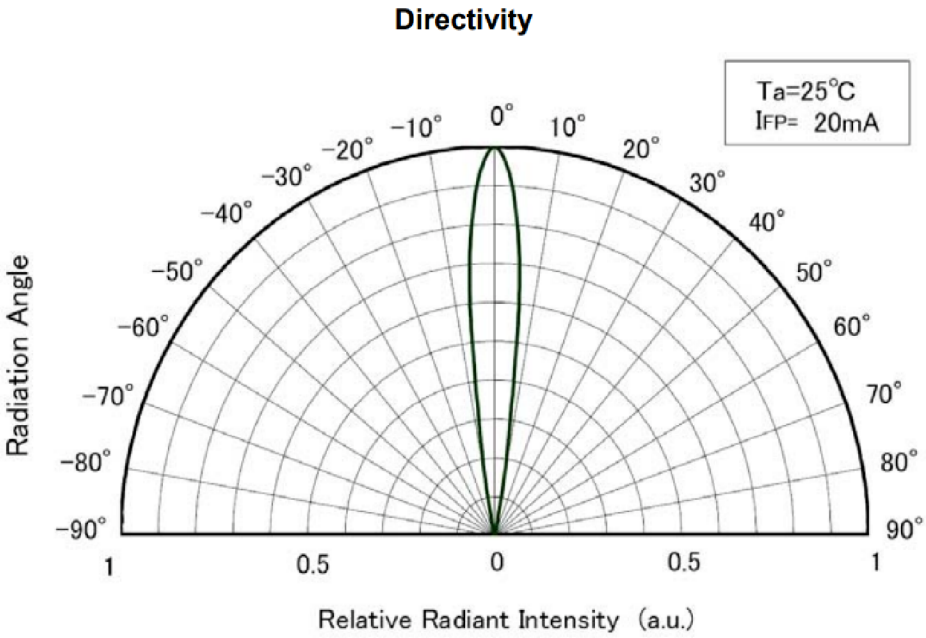

Figure 32 | Relative radiant intensity with respect to the rotational angle of the UV LED flasher. [14]

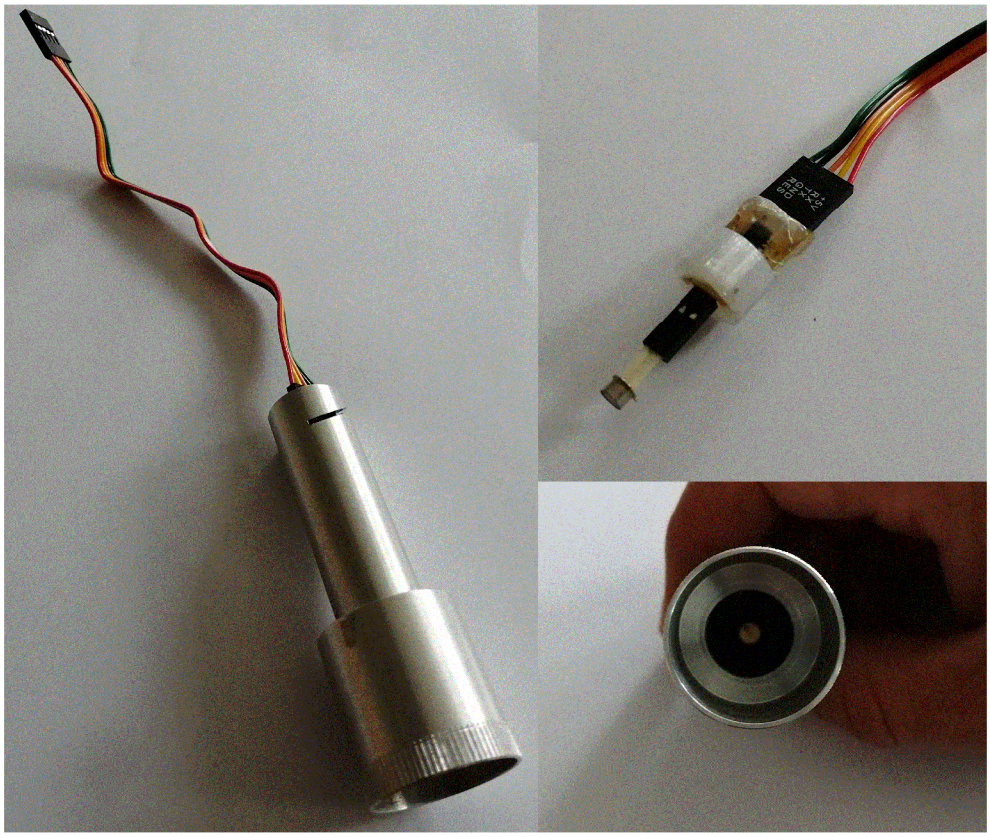

Figure 33 | Photos from various angles of the UV LED flasher used in calibration measurements.

Figure 34 Infrared images of all four examined FAST telescopes. One, (top left) located in PAO, Argentina and north (top right), middle (bottom left) and south (bottom right) are telescopes located in TA, Utah. Taken using CamView App.

2. Data analysis

2.1. FAST database

In 2020, a FAST database has been established. The aim of this database is to store any necessary information regarding FAST telescopes on both PAO and TA sites. Measurements from environmental monitoring sensors are stored on this database, as well as all required calibration constants mentioned in sections 1.6.1 and 1.6.2, respectively. The database is set up on a MariaDB server in the Joint Laboratory of Optics of the Palacky University, Czech republic. A free, multi-platform database program DBeaver [15] was employed for the purpose of database visualization. This thesis examines data from both the PAO and TA site, and thus multiple tables of the aforementioned database are utilized. The server contains several databases with unique purposes. The individual databases are:

- FAST - A database containing various data about the conditions of the FAST telescope situated on the PAO site. This database offers measurements up to July 2021 and is currently unused.
- FAST_PAO_CALIB - A database containing information about the UV LED calibration measurements, including the calibration constants for PMTs on FAST telescopes on the PAO site.
- FAST_PAO_MONI - A database containing measurements from environmental sensors for the PAO site mentioned in Section 1.6.1.
- FAST_PAO_RUN - A database containing various data about the PMT measurement runs for the PAO site. Data from this database was utilized in [1].
- FAST_TA_CALIB - A database containing information about the UV LED calibration measurements, including the calibration constants for PMTs on FAST telescopes on the TA site.
- FAST_TA_MONI - A database containing measurements from environmental sensors for the TA site mentioned in Section 1.6.1.
- FAST_TA_RUN - A database containing various data about the PMT measurement runs for the TA site.

The databases are divided into sections for both the PAO and TA sites. For the purpose of this thesis, calibration constants for the individual PMTs located in the CALIB databases are utilized, as well as the environmental measurements located in the MONI databases.

2.1.1. Calibration database

The CALIB database consists of tables regarding the calibration constants for the PMTs situated on FAST telescopes. The calibration constants are further used to convert the signal of the PMT (measured in counts) to the number of photoelectrons produced during the detection (Np.e). The calibration constants of the PMTs of the TA FAST telescopes are provided as an example in figure 35.

The table consists of these columns:

- timestamp - Specific time of the calibration measurement. The value provided is in Epoch Time, the number of seconds that have elapsed since the midnight (UTC time) of January 1st, 1970. To convert into a more conventional time format, an Epoch Time converter can be utilized.
- chanid - The ID of the individual PMTs. Each FAST telescope consists of 4 PMTs, so for the 3 telescopes present on the TA site, 12 PMTs are employed, labeled as channel ids from 0 to 11.
- value - The specific value of the calibration constant for individual PMTs. This value value is further used in conversion of the FAST PMT signal to the number of photoelectrons (Np.e).

	timestamp	chanid	value
1	1,475,466,439	4	8.3
2	1,475,466,439	5	8.262
3	1,475,466,439	6	8.223
4	1,475,466,439	7	8.328
5	1,506,406,530	0	6.443
6	1,506,406,530	1	8.026
7	1,506,406,530	2	7.965
8	1,506,406,530	3	6.174
9	1,538,809,169	8	11.451
10	1,538,809,169	9	8.05
11	1,538,809,169	10	7.832
12	1,538,809,169	11	7.962

Figure 35 Example of a FAST database containing the calibration constants for the PMTs on the Telescope Array site.

2.1.2. Environmental conditions database

Data regarding the environmental conditions measurements are located in the MONI databases. In the case of the PAO site, data up to July 2021 are present in a different table, as mentioned in the previous section. Furthermore, as mentioned in Section 28, the FAST telescope is equipped with detectors of temperature, pressure, humidity, light, or sensor status. Data from these telescopes are then stored within these databases. Additionally, an example of the FAST_TA_MONI database is provided in figure 36.

	ID	timestamp	RainStat	RainCounts	RainTime
1	1	1,669,250,054	0	0	1,669,249,989
2	2	1,669,250,557	0	0	1,669,250,529
3	3	1,669,250,954	0	0	1,669,250,890
4	4	1,669,251,481	0	0	1,669,251,430
5	5	1,669,251,854	0	0	1,669,251,790
6	6	1,669,252,154	0	0	1,669,252,091
7	7	1,669,252,454	0	0	1,669,252,391
8	8	1,669,252,754	0	0	1,669,252,691
9	9	1,669,253,054	0	0	1,669,252,992
10	10	1,669,253,353	0	0	1,669,253,292
11	11	1,669,253,654	0	0	1,669,253,592
12	12	1,669,253,954	0	0	1,669,253,893
13	13	1,669,254,254	0	0	1,669,254,193
14	14	1,669,254,554	0	0	1,669,254,493
15	15	1,669,254,854	0	0	1,669,254,794
16	16	1,669,255,154	0	0	1,669,255,094
17	17	1,669,255,454	0	0	1,669,255,394
18	18	1,669,255,754	0	0	1,669,255,695
19	19	1,669,256,054	0	0	1,669,255,995
20	20	1,669,256,354	0	0	1,669,256,295

Figure 36 Example of a FAST database containing measurements from the environmental conditions detectors situated inside the FAST telescope hut.

Of particular importance are these columns of the table:

- ID - an ID of the individual measurements.
- timestamp - Specific time of the calibration measurement. The value provided is in Epoch Time, the number of seconds that have elapsed since the midnight (UTC time) of January 1st, 1970. To convert into a more conventional time format, an Epoch Time converter can be utilized.
- tempin - Data from a temperature sensor situated in a FAST telescope hut.
- tempout - Data regarding the outdoor temperature outside the FAST telescope hut.
- tempcam- Data from a temperature sensor located close to the camera box of the FAST telescope. This value is perhaps the most indicative of the temperature of the PMTs.
- humidity - Data regarding the humidity inside the FAST telescope hut.
- pressure - Data regarding the atmoshperic pressure inside the FAST telescope hut.
- lightin - Data from a light sensor measuring the light status inside the FAST telescope hut.
- lightout - Data from a light sensor measuring the light status outside the FAST telescope hut.
- ShutterClosed - Data regarding the status of the shutter of the FAST telescope hut.

Note that three FAST telescopes are located in the Telescope Array, Utah. Thus the database has to contain data from individual huts. If the measurement fails or the detectors are unable to function properly, the value -300 is assigned to the measurement. Consequently upon further analysis, all such inaccurate measurements are to be eliminated from the analysis.

2.2. Software

For any subsequent data analysis Python programming language[16] was utilized. Additionally, the integrated development environment PyCharm[17], developed by JetBrains, was employed. Due to the massive sizes of the FAST calibration measurement data, a fast and effective tool is required for proper data management and analysis. A python library NumPy[18] provides the necessary extensive mathematical, computational and data processing functions crucial to the analysis. For data visualization, two distinct python libraries were employed. MatPlotLib[19] offers excellent graphical framework for generating high-quality static graphic images in python. Another data visualization toolkit used is Bokeh[20]. This python library allows creating interactive visualization in a .html format, displayable in any web browser. In addition, Bokeh enables the construction of a real-time visualization toolkit linked to python code and executed on a Bokeh server. Deployment of one such Bokeh server displaying FAST data is discussed in Section 3. Since the calibration constants and telescope environmental conditions measurements are located on a SQL MariaDB server in Joint Laboratory of Optics of the Palacky University, Czech republic, it was necessary to employ an SQL toolkit and object-relational mapper. The Python programming language's SQLAlchemy[21] library provided an open-source toolkit to interact with the SQL database, which was essential to access the data stored on the MariaDB server. Several examples of the python scripts utilized in the context of this thesis are provided in the appendix of the thesis.

2.3. Environmental conditions

Valid environmental conditions have to be ensured for proper functionality of the FAST telescopes. A single FAST hut is equipped with numerous sensors monitoring several variables that can influence the performance of the telescope. Variables such as temperature, pressure, humidity, light are monitored constantly and stored on an SQL server. The weather conditions of both the Argentinian and American deserts are observed to secure that the conditions present do not impede the detection capabilities of the telescope, or the electronics operating said telescope. Figure 37 displays a histogram of all measurements of outdoor temperature from the PAO and TA sites. Note that the histogram of Telescope Array temperature measurements is heavily skewed towards lower temperatures, as the FAST telescopes have been deployed since late 2022 and are only gathering environmental data since then (to April 2023). Only data obtained during winter are thus present in the database. Figure 38 then displays the indoor temperature measurements inside the FAST huts of one PAO and three TA telescopes. Additionally, information about the camera temperature is provided in figure 39 in the same format.

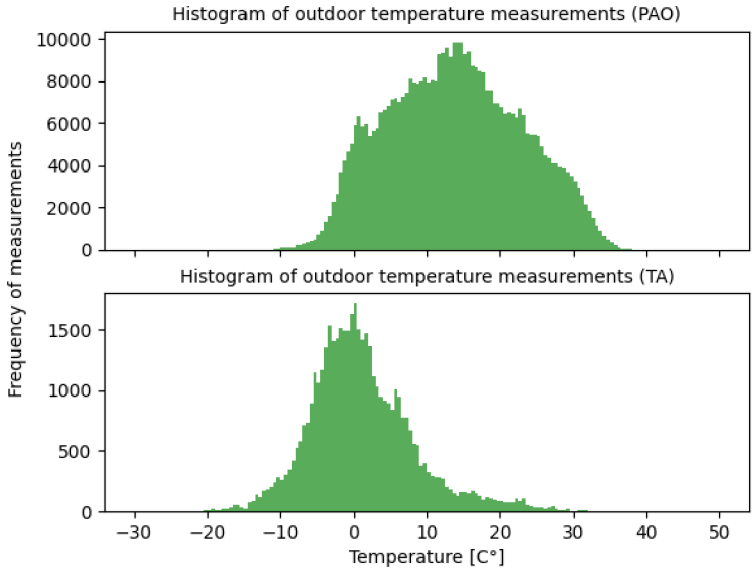

Figure 37 Histogram of outdoor temperature measurements of the telescope situated at the PAO site (top) and three other FAST telescopes located in TA, Utah.

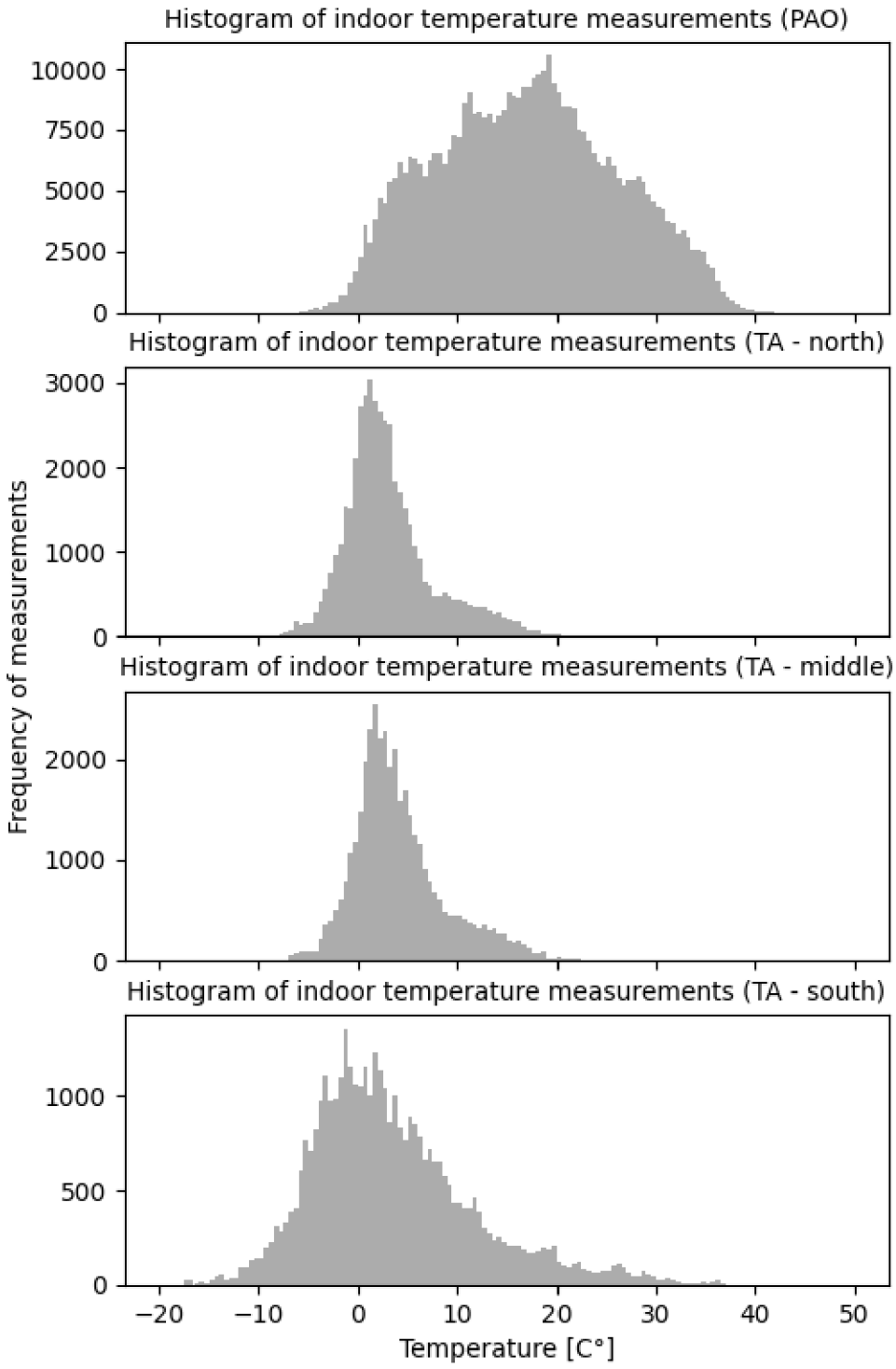

Figure 38 Histogram of indoor temperature measurements of the telescope situated at the PAO site (top) and three other FAST telescopes located in TA, Utah.

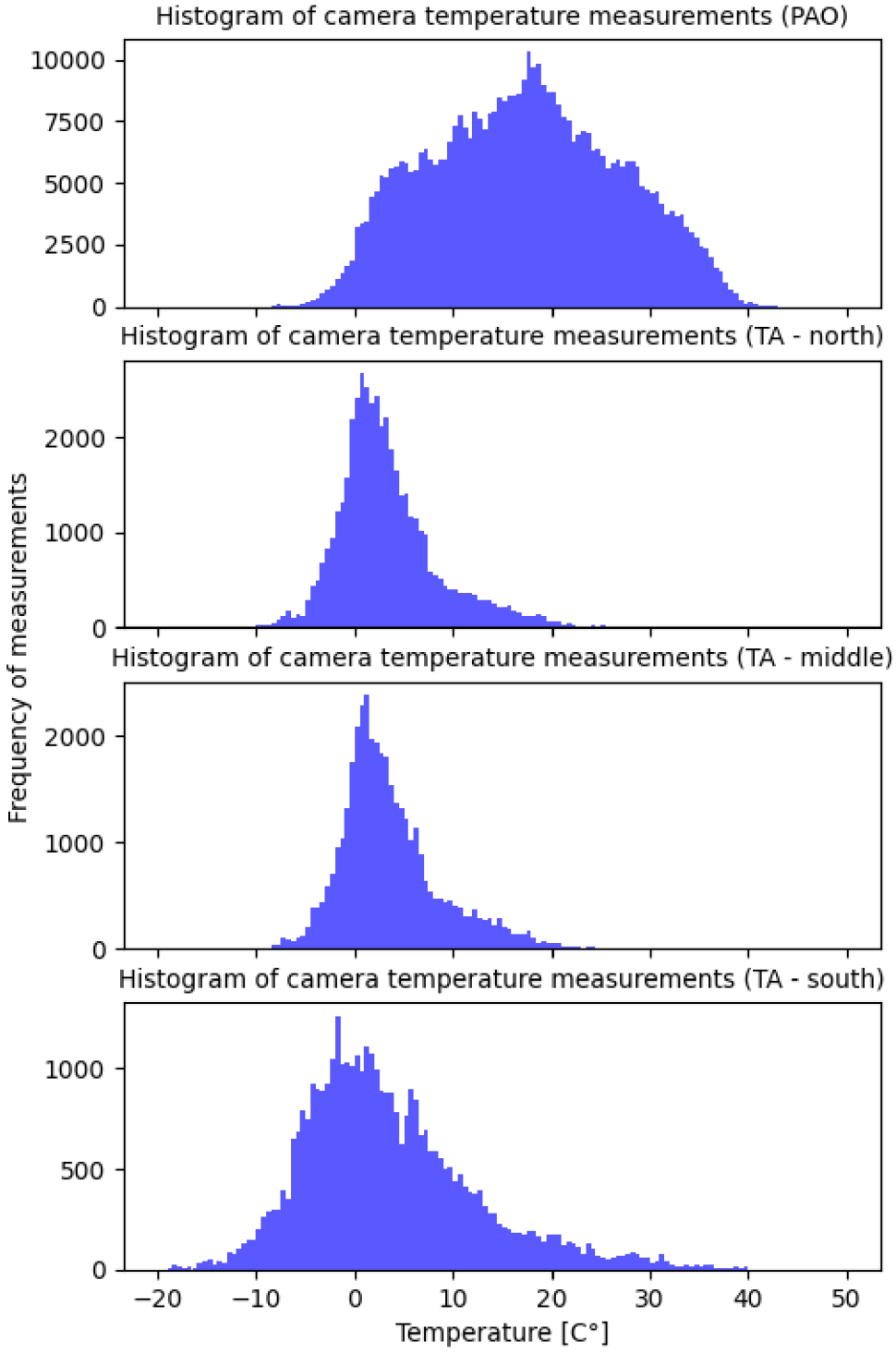

Figure 39 | Histogram of camera temperature measurements of the telescope situated at the PAO site (top) and three other FAST telescopes located in TA, Utah.

The histograms in previous figures are set up with a resolution of 0.5 °C. The outdoor temperature measurements shown in figure 37 are differentiated for both the PAO and TA sites. The histogram concerning outdoor temperature in the PAO site has been created with data ranging from early 2020 to April 2023. Thus data off all seasons throughout a number of years is present. The temperatures were measured using the Dallas DS18B20+ temperature sensor situated behind the fast hut, as can be seen in figure 28. The temperature range is relatively stable, with the lowest temperature being $\sim$ -10 °C and highest being $\sim$ 36 °C. The peak of the histogram, or the most common outdoor temperature in the Pierre Auger Observatory recorded is $\sim$ 15 °C. Note that the PAO and TA sites are located on different hemispheres, and thus experience different seasons and different temperatures during the same time horizons. The data from outdoor TA temperature measurements are shifted towards lower temperatures, as the telescopes have been commissioned in late 2022 and only winter data is currently available. The winter conditions at Telescope Array are considerably harsher, with temperatures often plummeting below -20°C. The average temperature of the TA site is $\sim$ 0°C, which is typical for winters of the Delta Utah region where the site is located.

Of higher importance is the data regarding temperature inside the individual FAST huts, as seen in figure 38. As was the case with outdoor measurements, PAO histogram is comprised of measurements obtained throughout all seasons from a number of years, whereas the data visible in TA indoor measurements were obtained during winter 2022/2023. The PAO FAST hut registers temperatures in the range of $\sim$ -5°C to $\sim$ 40°C, with a peak at $\sim$ 20°C. The data from TA FAST huts exhibit interesting variability. Whereas the sensors located in the north and middle huts provide relatively similar results, the Dallas DS18B20+ temperature sensor inside the third south FAST hut exhibits drastic temperature variations. The north and middle huts measure temperature in the range of $\sim$ -8°C to $\sim$ 11°C, with a peak at $\sim$ 3°C. The sensor located inside the south FAST hut detects temperature within a wider range, from $\sim$ -18°C to $\sim$ 36°C, with a peak at $\sim$ -1°C. The data from the south hut closely resembles the outdoor temperature shown in the bottom panel in figure 37, with roughly the same lower and higher temperature extremes. As the shutters of the three TA FAST huts are usually operated in sync, another cause has to be examined. This observed variation is most probably due to the difference of the material of the FAST huts. The north and middle huts are constructed with a core made of chipboard, whereas the south FAST hut is comprised of sheet metal. The sheet metal provides higher heat conductivity than the chipboard counterpart and thus offers less heat insulation. This temperature variability will be further discussed in Section 4.

The most significant temperature measurements are those of the camera box, which are visible in figure 39. The temperature sensors responsible for these measurements are the closest to the individual PMTs, and thus the temperature of the camera box will be further used as the temperature of the PMTs for subsequent data analysis. The histogram of the camera box temperatures of the FAST telescope on the PAO site matches the data from the indoor measurements, in a range of $\sim$ -8°C to $\sim$ 40°C, with a peak at $\sim$ 20°C. The measurements from the three FAST huts located in the Telescope Array exhibit the same behaviour as their respective indoor temperature measurements.

The temperatures of the camera boxes of all four panel are well within the operational range of both the electronics (as mentioned in Section 1.6.2) and of the PMTs, but severe temperature variability may alter the data from the UV LED calibration runs. The PMT signal is dependant on ambient temperature, as was discussed and shown in Section 1.5.2. This is due to the change in quantum efficiency with varying temperatures. Additionally, both the intensity of the UV light and the spectrum produced by the UV LED flasher is dependant of temperature as well, which may further increase the instability of the calibration runs. Furthermore, the appropriate spectral coefficients of both the glass of the FAST telescope mirrors and PMT input window are dependant on the wavelength of the incident light, further enhancing any present variability in the signal strength. However, these effect should only by visible when visualizing data via absolute calibration. By comparing the individual PMTs located on a FAST telescope, any temperature fluctuations should, in theory, effect all four PMTs equally, hence the temperature variability should not be seen in relative calibration. Data analysis regarding temperature stability of the PMTs will be further discussed in sections 2.6.2 and 2.7.2 for the PAO and TA sites, respectively.

2.4. Signal analysis

A single UV LED calibration run is comprised of five cycles, with a 10-second interval between individual cycles. Each cycle contains $\sim$ 200 flashes of the UV LED flasher, or events. This is recorded by each PMT individually. The measurements for each cycle are then stored in a ROOT file, named after the particular time of the measurements. One such measurement run might for example include these measurements:

- FAST_2022_08_17_04h01m30s_flasher
- FAST_2022_08_17_04h01m40s_flasher
- FAST_2022_08_17_04h01m50s_flasher
- FAST_2022_08_17_04h02m00s_flasher
- FAST_2022_08_17_04h02m10s_flasher

This particular calibration measurement was conducted on August 17th, 2022 at 4 hours, 1 minute and 30 seconds to 4 hours, 2 minutes and 20 seconds of UTC time. However, due to time delays, the cycles can be spaced 11 or even 12 seconds between each other. The individual event is then comprised of a rectangular signal, measured in counts. The PMTs detect the signal upon triggering an internal trigger. The electronics then register the time in bins, with each bin representing 20 ns. Aside from the rectangular signal, the event consists of $\sim$ 2000 bins both before and after the signal itself. This is done for the purpose of noise elimination. Given this, the rectangular signal is consistently observed at specific bins. For subsequent data analysis, the ROOT files were further converted into a format readable by the Python programming language.

Due to the immense number of measurements, the sheer size of the calibration files requires fast and effective computational procedures to manipulate and further analyze the calibration runs. This raises the need of computing a single value representative of the whole UV LED calibration run for application in subsequent large-scale analysis. This means that, initially, a specific value is assigned to each signal or event. And then further apply mathematical and statistical methods to determine a most representative value for the whole calibration run. For a single PMT, a UV LED calibration run is comprised of $\sim$ 1000 events, allowing for meaningful data comprehension and analysis. The calibration values of individual measurements runs are then further analyzed for both the PAO and TA sites.

2.4.1. Event signal

The signal generated by a specific UV LED flash, or event, is measured in counts and has a rectangular format, with its timing determined by bins corresponding to 20 nanoseconds. To assign a single value to directly represent the rectangular signal, several approaches can be considered. Ideally, a rectangular function should only exhibit a single non-zero value, corresponding to its amplitude or height. In practice, this is far from the case. Aside from a rising edge of the signal, the peak is not constant as well, as the signal at its height exhibits certain fluctuations. An example of one such PMT signal is shown below in figure 40. The rectangular signal of the FAST PMTs expresses a non-negligible rising edge, along with significant fluctuations at its amplitude. To appropriately assign a single value to a UV LED PMT event, several methods were considered.

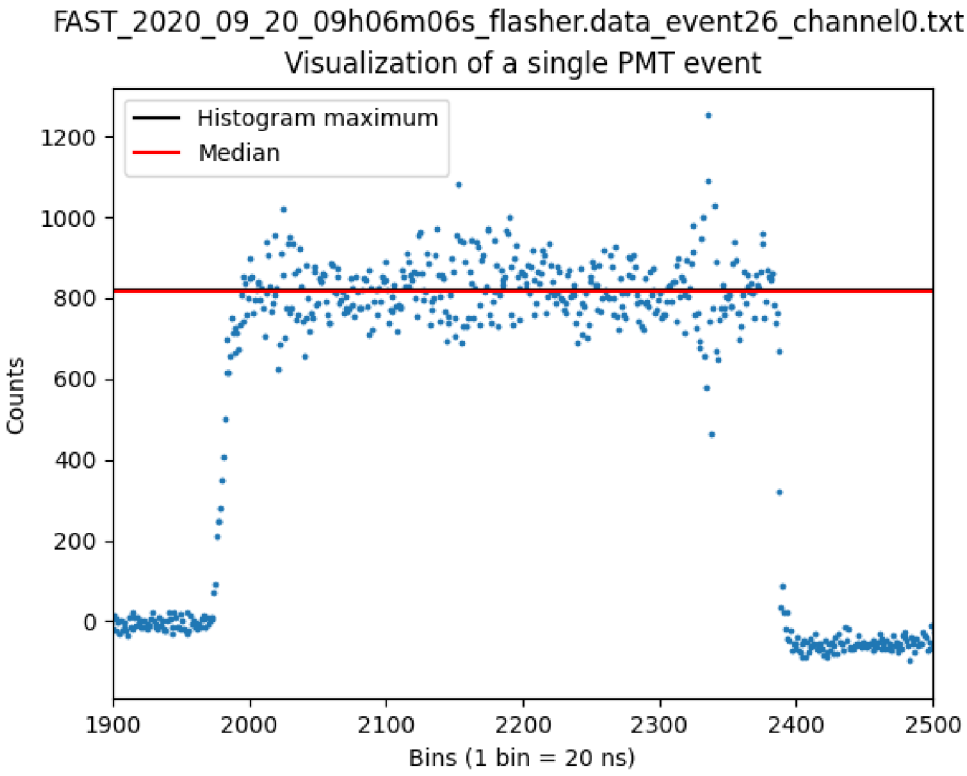

Figure 40 An example of a PMT signal detected on September 20th, 2020 at 9 hours, 6 minutes and 6 seconds (UTC).

Perhaps the fastest and the easiest method is to find the maximum of the signal, and assign the value as such. However, this leads to extreme loss of accuracy, as the fluctuations of the rectangular signal prohibit such approach. Furthermore, as can be seen in the example UV LED run in figure 40, a FAST PMT signal exhibits additional noticeable oscillations. These oscillations can become fairly extensive, as displayed on bins $\sim$ 2010, $\sim$ 2150 and $\sim$ 2320 in the example figure. Therefore, it can be concluded that the peak value of the signal does not serve as a precise and suitable representation of the FAST PMT signal.

Another possible approach is to find the most frequent value, or the maximum of a histogram of the PMT signal. As mentioned before, the PMT rectangular signal is always found at specific bins. Eliminating both the noise and the rising edge of the signal, bins ranging from 2000 to 2400 are most appropriate for the purpose of PMT event analysis, as the signal is predominantly concentrated within this range. Figure 41 shows histogram of the PMT event showcased in figure 40. Maximum of the histogram (black) is found at a count value of $\sim$ 821, which corresponds to the peak of the histogram. The count value of the histogram maximum is also shown as in figure 40 (black line).

Another possible approach to determine a value most representative of the rectangular PMT signal is to obtain a median of the discrete signal values. To once again eliminate the noise and the rising edge of the signal, bins ranging from 2000 to 2400 are utilized. The median value is then displayed in both figures 40 and 41 as a red line. The median of the discrete signal closely corresponds to the histogram maximum, further demonstrating the feasibility of utilizing this method for the analysis of FAST PMT signals. Figure 42 displays the difference (in absolute values of counts) of histogram maximum and the median of 10 000 randomly selected FAST PMT signals. In the vast majority of cases, the difference can be estimated at several counts.

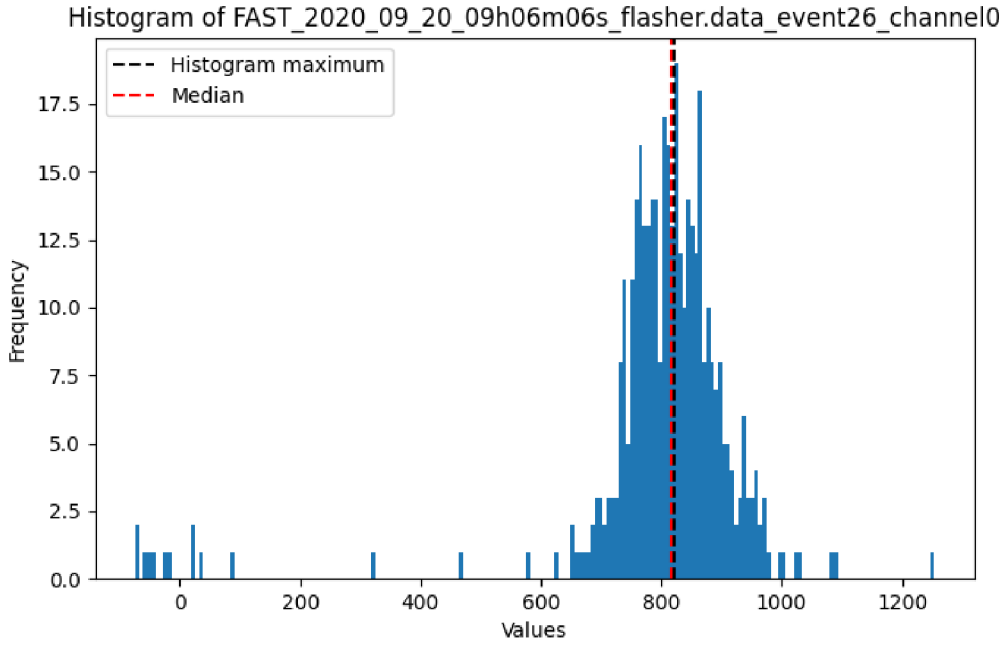

Figure 41 | A histogram of the PMT signal displayed in figure 40.

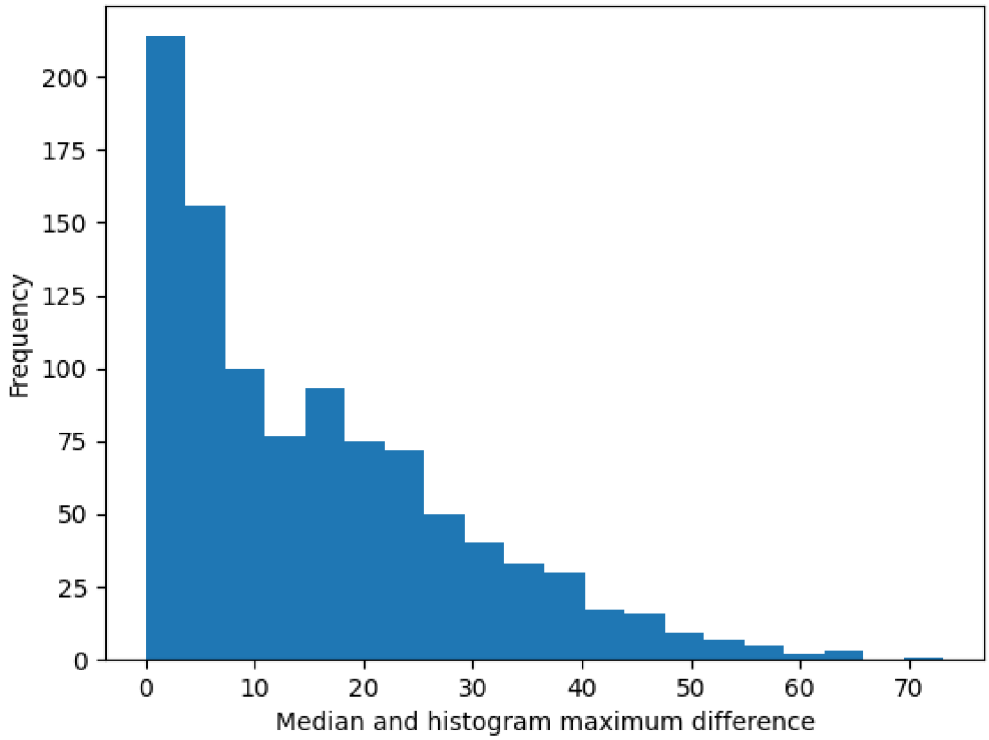

Figure 42 | A histogram of the absolute difference of histogram maximum and median from 10 000 randomly selected FAST PMT UV LED calibration measurements.

The last and perhaps the most sophisticated method for computing the most representative count value is to fit the histogram with Gaussian distribution and find the mean of the distribution through the fit. However, this presents a computational challenge, as performing such a task with tens of thousands of events detected by the PMTs within the FAST telescope would require a significant amount of time. Due to the size of the FAST UV LED measurements files, a computationally more suitable method of calculating the histogram maximum was chosen. Furthermore, a computationally less demanding approach is also required to enable the shifter operating the telescopes to retrospectively review the calibration measurements and assess their quality, potentially examining any issues should they arise.

The major disadvantage of this method is partially shown in figure 42. Throughout the 10 000 calibration measurements, in less than ~ 1 % of them, the difference between median and histogram maximum can reach tens of counts. One such UV LED calibration measurement is shown in figure 43 and its corresponding histogram is shown in figure 44. The disadvantage of computing the histogram maximum lies in the occasional inaccuracy representing the discrete rectangular signal. However, the difference, upon conversion, is a few photo-electrons at most. The variation is subsequently obscured in the immense statistical sample of the entire UV LED calibration run. Another interesting UV LED event is shown in figure 45. This measurements exhibits severe time delay of the rising edge and the rectangular signal as a whole. In such instances, histogram maximum is more accurate at representing signal amplitude than a median. Several other examples of FAST UV LED calibration events are shown in figures 45 to 47. For any further data analysis, histogram maximum was used as a representative of the PMT UV LED events.

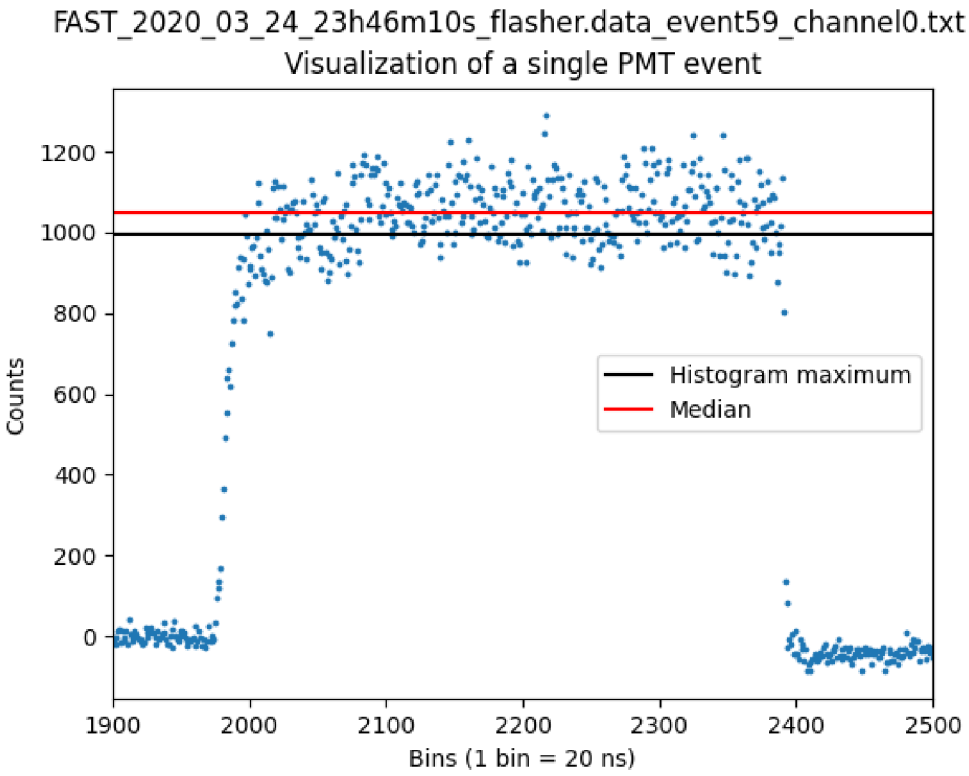

Figure 43 An example of a PMT signal detected on March 24th, 2020 at 23 hours, 46 minutes and 10 seconds (UTC).

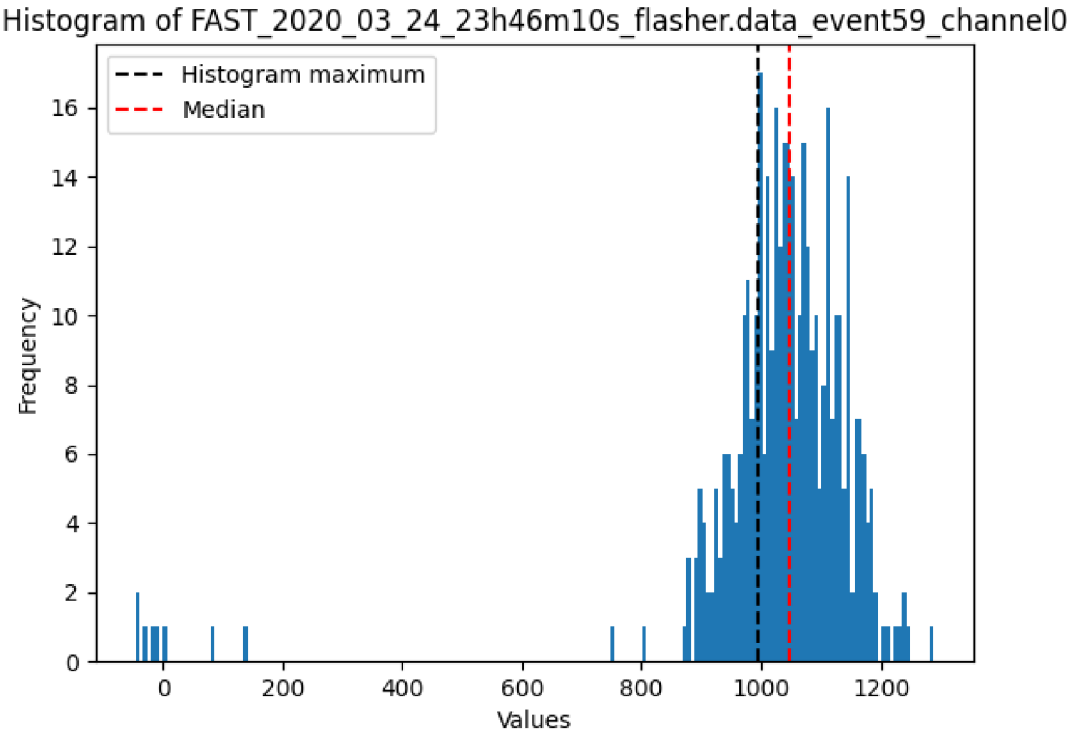

Figure 44 | A histogram of the PMT signal displayed in figure 43.

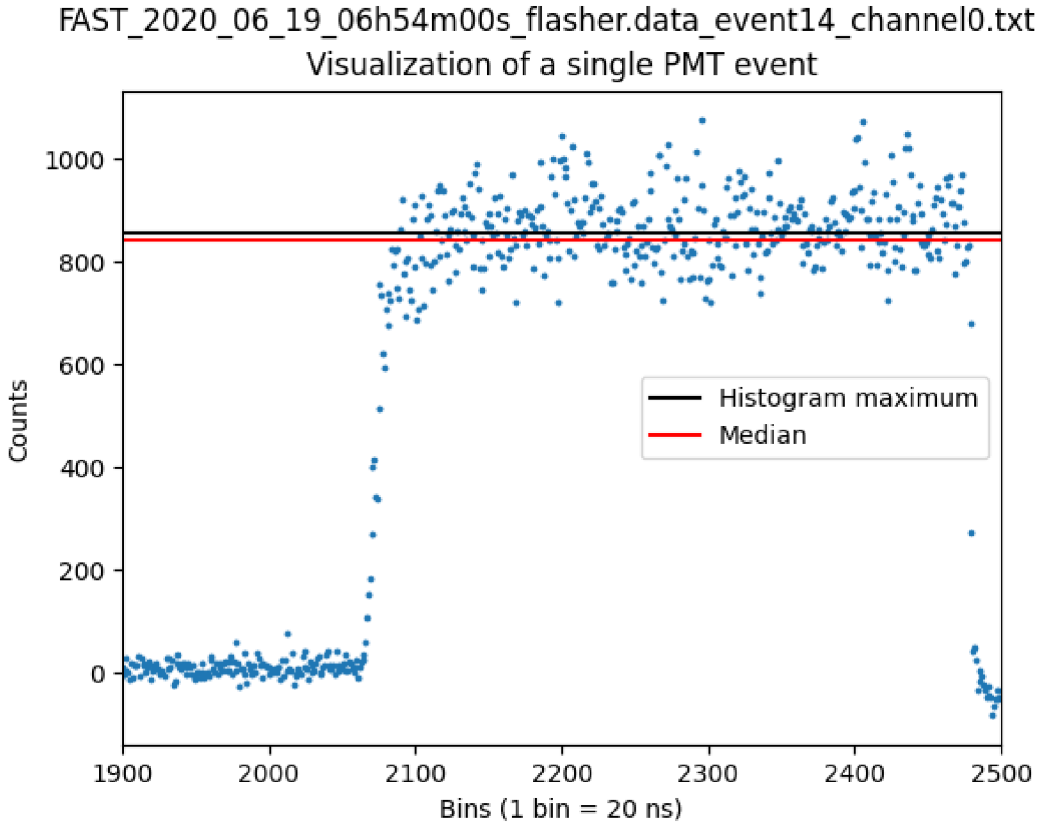

Figure 45 | An example of a PMT signal detected on June 19th, 2020 at 6 hours, 54 minutes and 0 seconds (UTC).

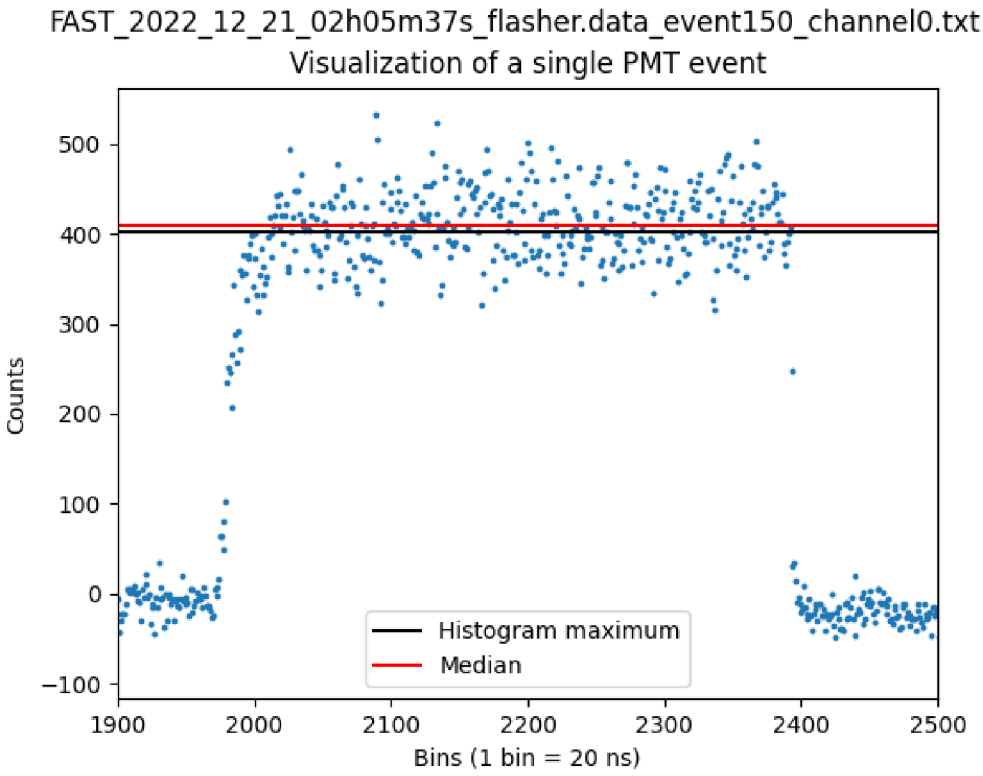

Figure 46 An example of a PMT signal detected on December 21st, 2022 at 2 hours, 5 minutes and 37 seconds (UTC).

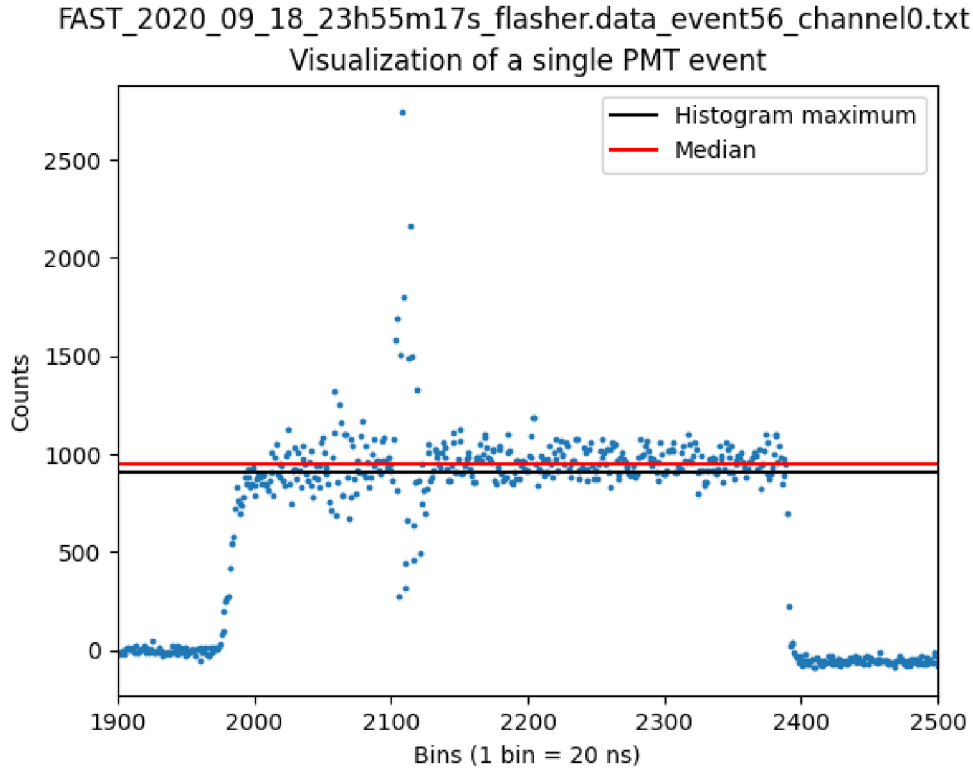

Figure 47 An example of a PMT signal detected on September 18th, 2020 at 23 hours, 55 minutes and 17 seconds (UTC).

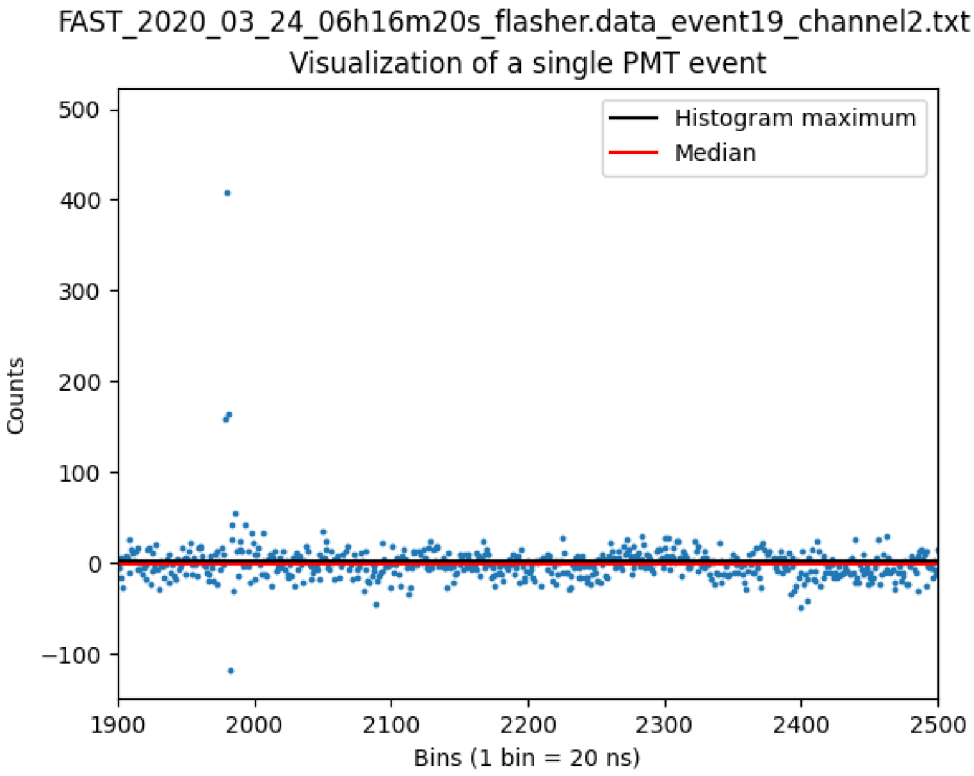

Figure 48 An example of a PMT signal detected on March 24th, 2020 at 6 hours, 16 minutes and 20 seconds (UTC).

2.4.2. Filters

For proper subsequent data analysis, faulty measurements have to be eliminated from the statistical sample of the calibration run. These faulty measurements might include runs with no signal detected, a signal with particular time delay, or a signal with severe oscillations present at its amplitude. Several of such filters were set up in order to improve the quality of the FAST data set and analysis.

The first and most important filter is set up to eliminate events with no signal detected. This phenomenon can occur mainly due to the presence of random peaks several bins in size, which can be attributed to unknown parasitic light sources or momentary malfunction of present electronic components. An example of one such UV LED measurement is displayed in figure 48. An ideal solution to such issues would be to set up a portion of the calibration python script to detect whether a signal contains a rising edge and a significant amplitude. Such process would however severely increase the computational time of the calibration and is deemed redundant. For the purposes of signal detection, a simple threshold will suffice. If the histogram maximum is lower than this threshold, than no signal is present in the measurement and the event is removed from the sample. This however presents a major drawback, as a signal with particularly low amount of counts would be mistaken for a signal with no signal detected. However, the FAST PMTs exhibit significant count gain and thus this does not happen in practice for the threshold of 40 counts used for further data analysis. In contrast, an event with no UV LED signal may still exhibit fluctuations and, in theory, its histogram maximum may indeed climb over 40 counts. This however has not happened for any of the calibration runs analyzed on both the PAO and TA sites. Furthermore, such an event would still not pass the filter examined in the following paragraph.

Severe fluctuations and oscillations of the FAST UV LED calibration event may reduce the quality of said measurement. To ensure that this parameter is adequately measured, another filter layer is introduced. The filter examines the standard deviation of the rectangular signal. Only bins ranging from 2000 to 2400 are utilized in the variance calculation, as the signal is predominantly concentrated withing those bins. The standard deviation of the FAST PMT UV LED rectangular signal can be calculated using this formula:

$$\sigma = \sqrt{\frac{1}{N}\sum_{i=1}^{N}(x_i - \mu)^2}, \tag{1}$$

where σ is the standard deviation of the signal, N is the number of data points, in the case of the FAST PMT signal, bins. Furthermore, x_i is the number of counts at a specific bin and μ is the mean of the analyzed discrete signal. Due to variation in the PMT gain, the standard deviation of a single event lacks significance. Hence, only relative standard deviation (or coefficient variation) is utilized. The standard deviation of the measurement is then calculated relative to the histogram maximum of the rectangular signal to compute the relative standard deviation. UV LED calibration events with significant oscillations at its amplitude may exhibit high standard deviation. However, as the oscillations do not significantly impact the resulting histogram maximum value, the filter cutoff can be set in a relatively non-discriminating manner. Thus, the threshold of relative standard deviation of elimination of a FAST PMT UV LED signal has been set up at 0.25. Standard deviation is examined further in Section 2.5.

The final layer of filters were set up to ensure that the UV LED calibration run is deployed in the appropriate format. Some of the performed UV LED runs were lacking any signal at all. It is possible that this is caused by a lack of power supply to the flasher or its complete absence. Such measurements then cannot be properly analysed, as they lack any determinable rectangular signal. These UV LED runs are to be eliminated from the sample. During this occurrence, some of the measurements may become corrupted, as the UV LED run is comprised of an incomplete amount of cycles, e.g, less than five. These incomplete UV LED calibration runs have to be eliminated from subsequent analysis as well, as they may reduce the quality of the data.

2.4.3. UV LED calibration run analysis

A complete FAST UV LED calibration run is comprised of 5 measurement cycles, each consisting of $\sim$ 200 events for particular PMTs. In Section 2.4.1, it was described that each event is assigned a histogram maximum of the measurement, a value representing the entire rectangular signal. A UV LED calibration run is then comprised of $\sim$ 1000 values for each PMT. The goal of this process is to obtain a value representative of the entire calibration run. A simple mean of the histogram maxima is sufficient, as the individual values are equally representative. For all further subsequent analysis, to determine a value most representative of the entire calibration run, a mean from histogram maxima of the individual events was utilized.

Another possible and superior approach to compute a value most representative of the calibration run would be to sum all the UV LED events into a single histogram, and then determine the final value through a Gaussian fit. This approach yields the most accurate results, however is all the more computationally demanding. Due to the sheer volume of FAST UV LED calibration files, a simpler and faster approach described beforehand was used.

2.5. Standard deviation calculation

The uncertainty of the individual UV LED PMT events can be calculated using the formula 1 provided in Section 2.4.2. By using the mean of the histogram maxima of all the events in a calibration run, a value representing the entire calibration run can be calculated. To further enhance the data analysis, calculation of the corresponding standard deviation of the calibration run has to be performed. Several different approaches are discussed in this section.

First of the mentioned methods utilizes the law of uncertainty propagation. The individual events exhibit inherent uncertainty, which may be used to determine the overall uncertainty of the calibration run. This is achieved via the formula:

$$\sigma_{run} = \sqrt{\frac{1}{N_{events}^2} \sum_{i=1}^{N_{events}} \sigma_i^2}, \tag{2}$$

where σ_{run} is the standard deviation of the whole FAST UV LED calibration run, N_{events} is the number of events detected throughout the five calibration cycles, and σ_i^2 is the standard deviation of the individual events as calculated using the formula 1. This approach, while statistically correct, leads to unrealistically low estimate of the standard deviation. Using the formula 2, the standard deviation of a calibration measurement would only arose to a few counts. With the gain of the PMTs, the relative standard deviation would only be a fraction of a percent. This is due to the fact that when multiple measurements are taken from a population, each measurement has its own inherent variability (as measured by its standard deviation), but the mean of the events will have reduced standard deviation, since the variation in the measurements is reduced when they are averaged.

Another possible approach is to modify equation 2 in a way that deliberately overestimates the standard deviation of the calibration run by voluntarily ignoring the reduction of the variance upon calculating the mean. This can be done with the formula:

$$\sigma_{run} = \sqrt{\frac{1}{N_{events}} \sum_{i=1}^{N_{events}} \sigma_i^2}. \tag{3}$$

The only difference between the formula 2 and formula 3 is the N_{events} present in a non squared form. This deliberately increase the standard deviation due to the reduction of variance upon averaging the measurement being ignored. This method is however far from ideal, as in return, this equation lead to gross overestimation of the complete standard deviation. This is shown in figure 49, on the data of PMT 0 on a FAST telescope stationed in PAO, Argentina in respect to time.

Note that both of the formulae mentioned can only be used due to the fact that the individual events within the calibration run are not correlated, in other words a prior PMT measurement does not, in theory, impact the measurements after and vice versa. The covariance of the events is thus 0. Furthermore, if all events exhibited equal standard deviation, the formula 2 would then simplify into a more well-known format:

$$\sigma_{run} = \frac{\sigma_{events}}{\sqrt{N_{events}}}, \tag{4}$$

where σ_{events} is the standard deviation of the events. This is however not the case, as the all the individual events within the UV LED calibration run exhibit different statistical variance.

Perhaps the most suitable approach is to calculate the standard deviation of the run without error propagation, using only the base equation for computing the standard deviation (as described in equation 1). This approach would ignore the inherent statistical variance of the individual events, but yields results that are more representative of the underlying population. The modified equation is provided below:

$$\sigma_{run} = \sqrt{\frac{1}{N_{events}} \sum_{i=1}^{N_{events}} (c_i - \mu_{run})^2}, \tag{5}$$

where σ_{run} is the standard deviation of the entire calibration run, N_{events} is the number of events in said run, c_i is the value in counts for the individual event and μ_{run} is the mean of the calibration run, the value most representative for the entire calibration measurement. An example of

the standard deviation calculated in such manner is provided in figure 50 on the same data set as figure 49. For the sake of clarity, the standard deviation of the calibration runs is omitted in any subsequent visualizations.

When calculating relative calibration, comparison of the absolute values is required and thus, the law of uncertainty propagation is further employed. The values are taken relatively to a certain reference PMT. The formula for computing the standard deviation of the subsequent relative values is shown below:

$$\sigma_{rel} = \frac{PMT_i}{PMT_{ref}} * \sqrt{(\frac{\sigma_{PMT_i}}{PMT_i})^2 + (\frac{\sigma_{PMT_{ref}}}{PMT_{ref}})^2}, \tag{6}$$

where σ_{rel} is the standard deviation of the relative value of the PMT, PMT_i is the absolute value of the PMT (in counts of Np.e), PMT_{ref} is the value of the reference PMT and σ_{PMT_i} with $\sigma_{PMT_{ref}}$ are the standard deviations of the i-th and reference PMT, respectively.

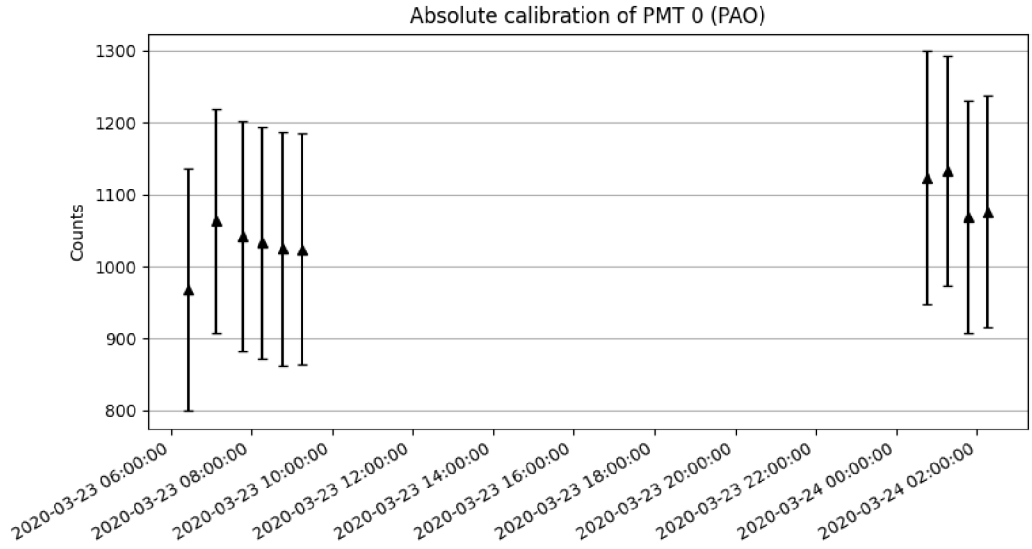

Figure 49 The absolute calibration of several UV LED runs of PMT0 of the FAST telescope in PAO, Argentina. The error bars were calculated using equation 3.

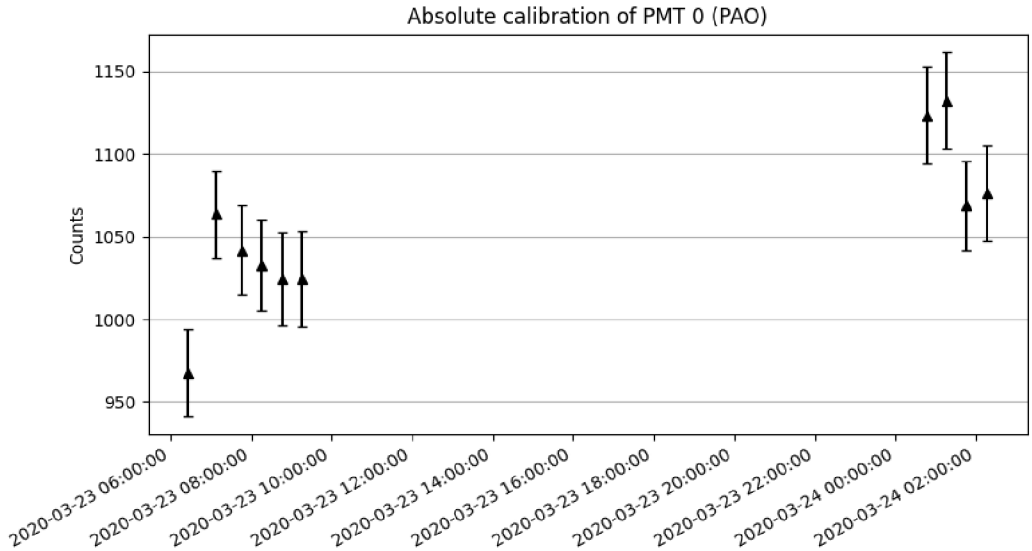

Figure 50 The absolute calibration of several UV LED runs of PMT0 of the FAST telescope in PAO, Argentina. The error bars were calculated using equation 5.

2.6. Analysis of PAO data

2.6.1. Time stability

Time stability is of severe concern to ensure appropriate quality of measurements over a long period of time. Time drift and life characteristics of PMTs were described in Section 1.5.1. Time drift is of relatively low priority, as the FAST telescope can only operate on moonless nights, or at most at $\sim$ 8 continuous hours of use. Life characteristics are more significant, as due to the economical constraints of the FAST project, the PMTs present on a FAST telescope are required to detect UHECRs over a long time horizons, preferably without major alteration in the strength of the PMT signal. Figure 51 then displays data obtained from March 2020 to March 2023 from the FAST telescope deployed in the Pierre Auger Observatory in Argentina. Figure 52 then shows the relative values of the PMT signal in reference to PMT1. The data were obtained and analyzed with methods described in Sections 2.4.1, 2.4.2 and 2.5. Overall, more than 2 000 000 individual UV LED events were analyzed.

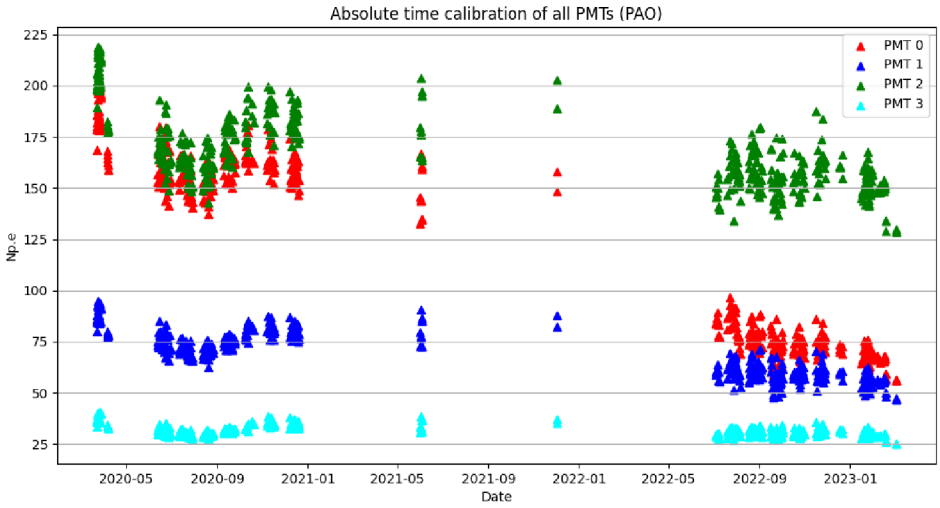

Figure 51 | Absolute time calibration of all PMTs on the FAST telescope located on the PAO site.

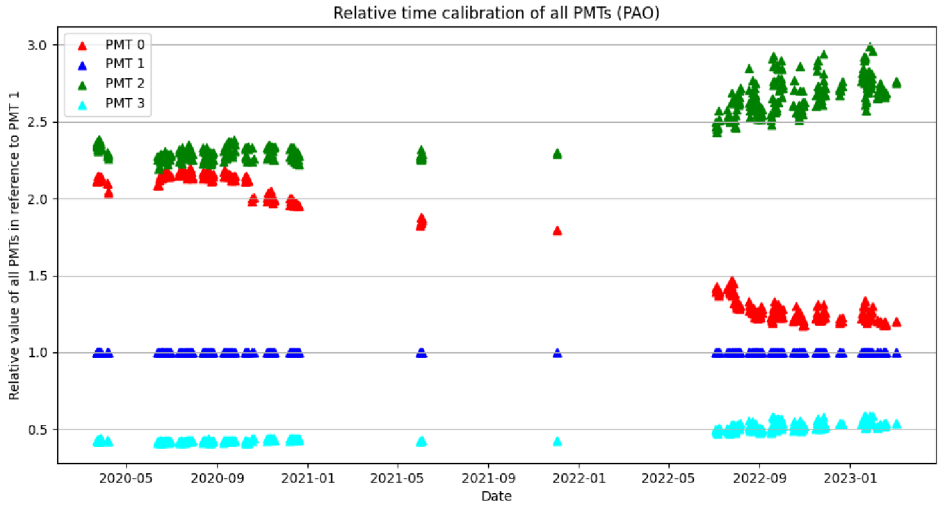

Figure 52 | Relative time calibration of all PMTs on the FAST telescope located on the PAO site. The relative values are taken with PMT1 as a reference.

The data of all PMTs exhibit significant fluctuations, which is expected with varying seasonal temperature in regard to both the annual and daily temperature cycles. While PMT3 displays a degree of stability, the signal from PMT0, PMT1 and PMT2 is largely unstable. This is further seen in figure 52, as the signal from PMT3 is more compact than the signal of the other PMTs. Note that the relative value of PMT1 is constant at a value of 1, as the PMT signal was compared to itself. The left side of the same graph is consistent with data presented in [1], further demonstrating the feasibility of all methods utilized. PMT3 also exhibits impressive life characteristic, as the signal from the PMT is fairly constant, with next to no present instability or variance. This however can be caused by the low gain of the PMT, as the oscillations are not as pronounced as is the case with other PMTs.

The values obtained from PMT0 are of primary concern, as the decrease in signal strength between 2020 and late 2022 to 2023 is appalling. The decrease is more than 50%, which is significantly larger than the data in the PMT documentation provided by Hamamatsu present in figure 22. All PMTs experienced at most 3 000 hours of mean time, which should, at maximum decrease, correspond to $\sim$ 80% signal decrease. PMT1 shows a degree of signal attenuation as well, but the attenuation is well within the provided life characteristic signal decrease range. This singular effect is further visibly enhanced in relative calibration, as the relative value of PMT0 in reference to PMT1 falls from $\sim$ 2.1 in early 2020 to $\sim$ 1.2 in early 2023. This shows that the signal of PMT0 decreases at almost twice the pace of PMT1.

The general fluctuations of the absolute values of all PMTs might be caused by varying temperature, which will become apparent in the following section if indeed that is the case.

2.6.2. Temperature stability

It is mandatory to ensure adequate temperature stability for quality data analysis of the atmospheric showers produced by UHECRs. As was mentioned in Section 1.5.2, the PMT signal should decrease with rising temperatures, in $\sim$ 0.4% per °C. Dallas DS18B20+ temperature sensor positioned on the camera box of the FAST telescope records the temperature of all four 200mm PMTs. The effect of temperature on the signal of PMTs is enhanced even further, as the UV LED flasher is dependent on temperature as well. The peak of the UV wavelength of light emitted is shifted towards smaller wavelength with increasing temperature. Furthermore, the radiant flux is highly dependant on temperature as well, with a peak at $\sim$ 30 °C. Data regarding absolute temperature calibration is provided in figure 53, whereas data regarding relative temperature calibration is provided in figure 54.

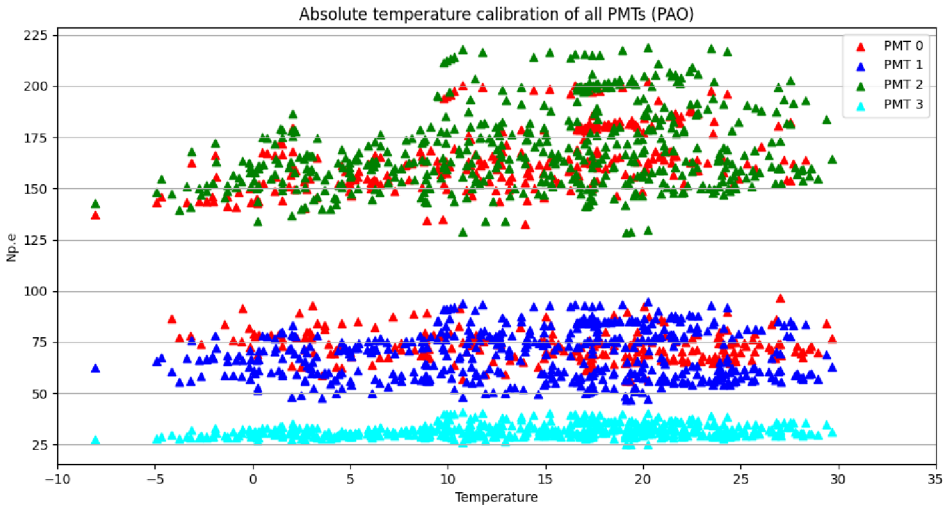

Figure 53 Absolute temperature calibration of all PMTs on the FAST telescope located on the PAO site.

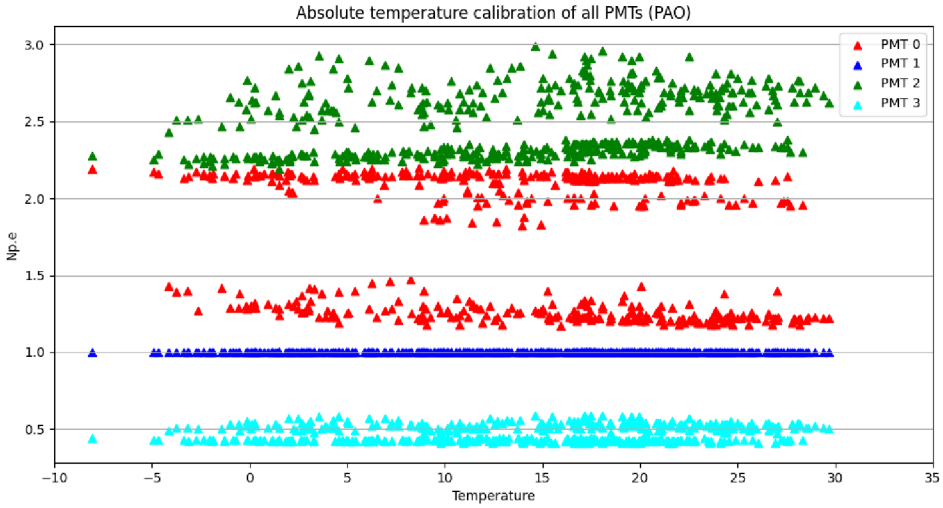

Figure 54 Relative temperature calibration of all PMTs on the FAST telescope located on the PAO site. The relative values are taken with PMT1 as a reference.

The data regarding temperature calibration is fairly clouted, due to some of the effects discussed in Section 2.6.1. The PMT signal reduced drastically between early 2020 and late 2022, and thus for improved visual clarity, data from these time periods is further separated and provided in figures 55 and 56. It is difficult to isolate the impact of temperature on individual PMTs, as the life characteristic of the PMT signal effect is also present in both figures. The data presented in this section is the same as in the previous Section 2.6.1, but is visualized in relation to temperature.

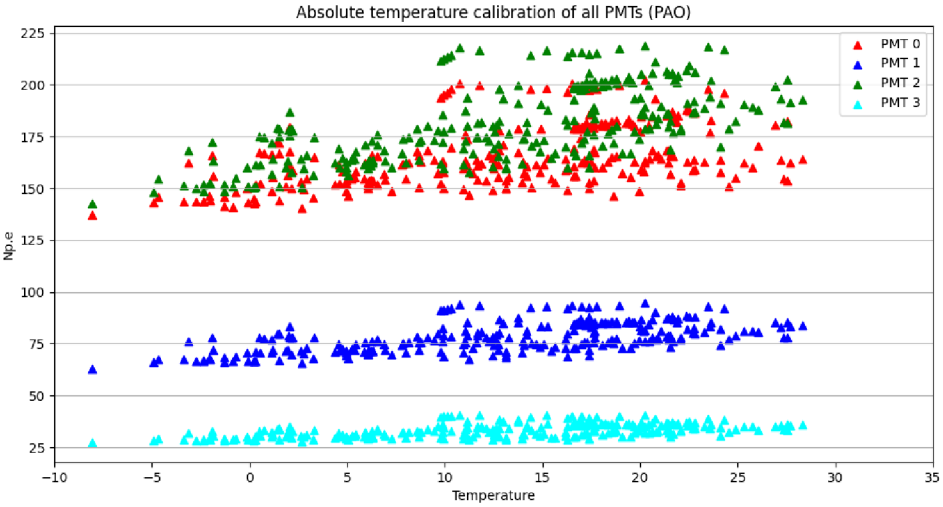

Figure 55 Absolute temperature calibration of all PMTs on the FAST telescope located on the PAO site. The relative values are taken with PMT1 as a reference. Data from March to December 2020.

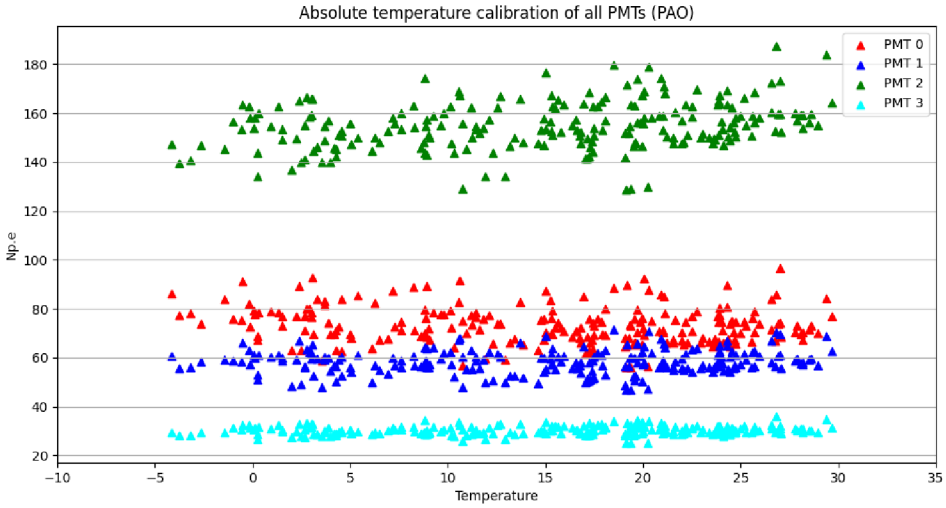

Figure 56 Absolute temperature calibration of all PMTs on the FAST telescope located on the PAO site. The relative values are taken with PMT1 as a reference. Data from August 2022 to March 2023.

The effect of life characteristic, or the reduction in signal strength in time is best seen in figure 54, as the relative values of all PMTs (except PMT1, as the PMT is used as a reference) are divided into 2 discrete sections. This effect is most pronounced on PMT0, as the sections are based at relatives values of $\sim$ 2.1 and 1.3. This corresponds to the effect shown in 52, as the PMT signal drastically reduced over a period of several years. Therefore, it is advisable to separate the data and analyze the two time periods independently.

Figure 55 displays data regarding absolute temperature calibration from March 2020 to December 2020, whereas figure 56 from August 2022 to March 2023. The effect of different life characteristics of the PMTs should be mostly avoided. Despite such efforts, the PMTs exhibit notable instability. The fluctuations of PMT0 and PMT2 could be further caused due to signal loss in November 2020 and September 2022. However, PMT1 and PMT3 exhibit similar behaviour, with no notable apparent signal reduction with respect to time. A possible culprit, although unlikely, is the positioning of the PMTs on the FAST telescope, as PMT0 and PMT2 are located on the same horizontal plane.

Furthermore, the data from 2020 exhibit severe temperature dependency, as the signal increases with increasing temperature. This is directly in contrast to the data provided by the manufacturer in Section 1.5.2. This is perhaps due to the temperature dependency of the UV LED flasher, as both the peak wavelength and radiant flux of the emitted light is highly temperature dependent. This will be examined further in Section 4.

2.7. Analysis of TA data

In November 2022, three separate FAST telescopes were commissioned in the Telescope Array, Utah. All of these telescopes are further equipped with a UV LED flasher as well, for calibration measurements. Two of the telescopes are also equipped with a Yttrium Aluminum Perovskite (YAP) crystal, that permanently emits light in discrete sets of several bins at most. Along with the UV LED measurements, YAP can serve as a calibration method for FAST telescope to properly assess the signal strength of individual PMTs present on the telescope.

Three FAST telescopes contain in total 12 individual PMTs. PMTs 0-3 are situated on the north FAST telescope, PMTs 4-7 on the middle and PMTs 8-11 on the south FAST telescope. However, the signal from the UV LED flasher is corrupted to a significant degree, as the individual PMTs exhibit a wide range of gain values. Several of the PMTs detect the rectangular signal at a few hundred counts at most, while others record the UV LED signal at thousands, or ten thousand counts. This is further shown in figures 57 and 58. For this reason, the data visualization is not separated into graphs for separate telescopes, but rather separated into high-gain and low-gain data sets. The middle FAST telescope exhibits only high-gain PMT values, and is therefore most suitable for data analysis. The reason for the signal corruption will be discussed in further sections.

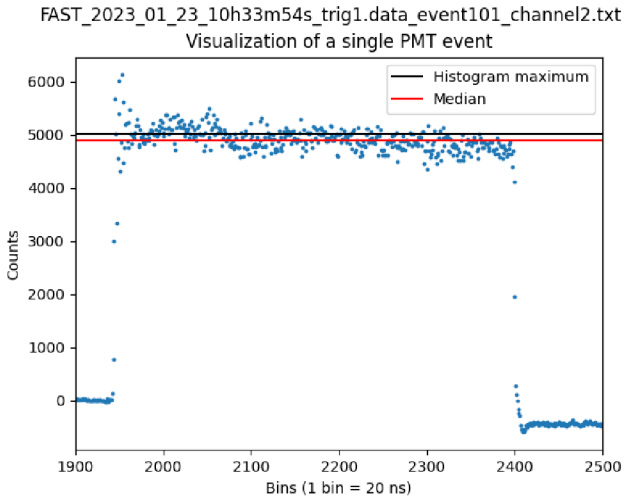

Figure 57 An example of a PMT signal detected on January 23rd, 2023 at 10 hours, 33 minutes and 54 seconds (UTC) from the FAST TA north telescope exhibiting high PMT gain.

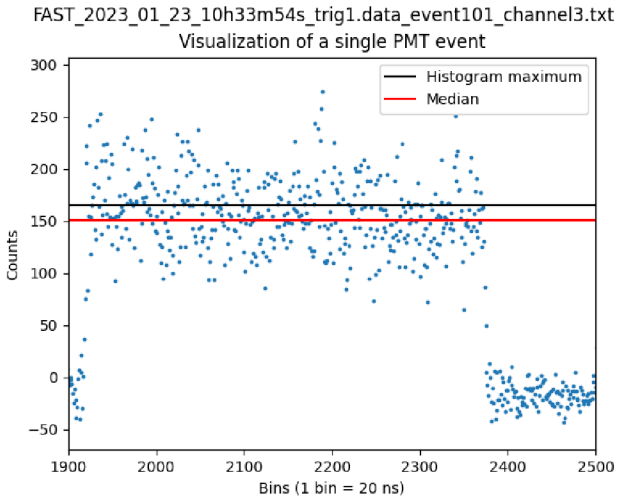

Figure 58 An example of a PMT signal detected on January 23rd, 2023 at 10 hours, 33 minutes and 54 seconds (UTC) from the FAST TA north telescope exhibiting low PMT gain.

2.7.1. Time stability

The three FAST TA telescopes have been deployed in late 2020, and only data from January 16th to February 10th are available. Due to the limited data set, it is impossible to assess the life characteristic of the PMT, as they have only been commissioned recently. Only absolute calibration is shown, as comparing the PMT signal relatively yields little to no benefit, due to the varying PMT gain. Figure 59 displays absolute time calibration of high-gain PMTs, while figure 60 provides the same data for low-gain PMTs.

High-gain PMTs exhibit sufficient time stability, although no particular concrete assessment can be made due to the limited data set. Temperature variations play a minimal role, as all the measurements were taken in January to February, in the winter season on northern hemisphere. This will become apparent in the following Section 2.7.2. The PMTs with low gain demonstrate significant instability. However, it is important to note that the displayed data should be interpreted with caution, as the UV LED configuration for these PMTs is not properly set up. Due to the high standard deviation of measurements on low-gain PMTs, the omission of the standard deviation filter in the data analysis was necessary to obtain a sufficient quantity of data for analysis purposes. PMT2 however demonstrates a degree on signal loss on January 20th, but this effect is present on all PMTs located on the north FAST TA telescope.

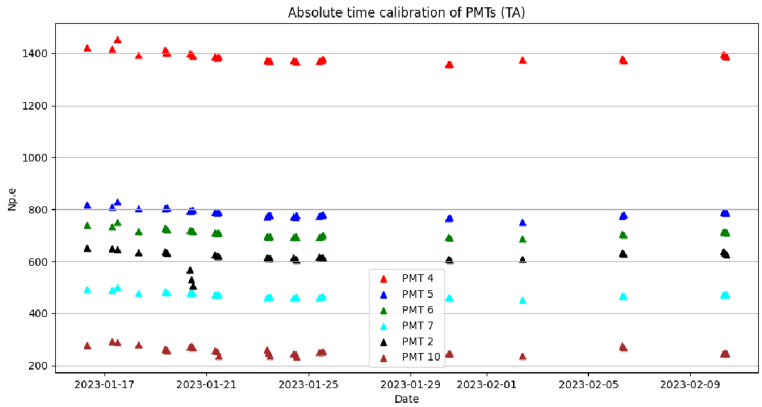

Figure 59 Absolute time calibration of PMTs demonstrating high gain on the FAST telescopes located on the TA site.

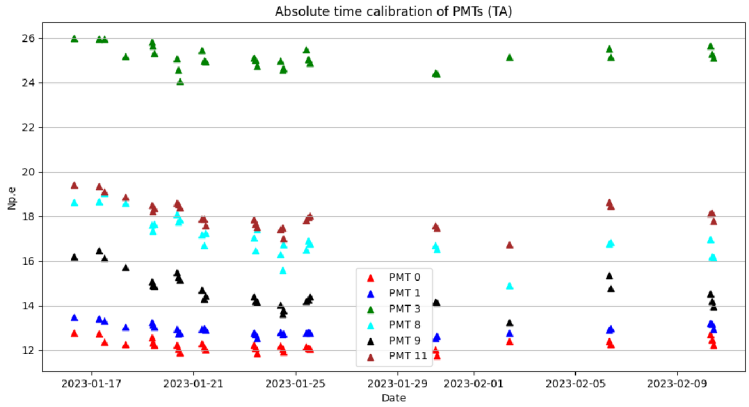

Figure 60 Absolute time calibration of PMTs demonstrating low gain on the FAST telescopes located on the TA site.

2.7.2. Temperature stability

Temperature stability is of primary concern, as various changes in temperature may alter the functionality of not only the FAST PMTs, but the UV LED flasher along with the optical elements themselves. The data from PAO site were not ideal in that manner, as the data was obtained from a period of several years, and as demonstrated in figure 51, some of the present PMTs experienced drastic signal loss with respect to time. This is not the case in the data obtained from all three TA FAST telescopes, as the telescopes were deployed in late 2022 and have only been used for several months. Figure 61 then shows the absolute temperature calibration of high-gain PMTs, whereas figure 62 displays absolute temperature calibration of low-gain PMTs.

Note that the Dallas temperature sensor was located in each individual FAST hut, therefore the temperature of the PMTs is measured for each FAST telescope separately. This is important, as we have seen in the Section 2.3, that the three FAST huts present on the TA site experience different temperatures. This is the reason why the temperature is not aligned in both mentioned figures.

Temperature dependency not burdened by the life characteristic or time drift of the PMT is crucial for any temperature data analysis. The PMTs on the TA FAST telescopes currently provide exactly that. Of particular importance is data from PMTs 4-7 on the middle FAST telescope, as all the PMTs present on said telescope exhibit the correct high-gain from the UV LED calibration measurements. Aside from the life characteristic of the PMTs, the data shown corresponds to the temperature calibration of data from the PAO site, as the signal strength increases with rising temperatures. Again however, this is in direct contrast to the expected behaviour provided by the manufacturer and measured in preliminary FAST temperature calibration mentioned in Section 1.5.2.

The range of the temperature is important as well, as the PMTs situated in the south TA FAST hut experienced temperatures drastically lower than their PAO counterparts. While the PMTs on the PAO FAST telescope performed measurements at temperatures of -5°C, the Dallas temperature sensor in the south TA FAST hut recorded temperatures as low as -12°C. AS mentioned before, this is due to the fact that the south TA FAST hut is equipped with less heat insulation, as the hut itself is constructed using sheet metal. This enables analysis of a wider range of temperatures and provides subsequent data for further analysis.

Although the PMTs' behavior concerning temperature is unexpected, the gathered data indicates that the PMT signal remains stable across all available PMTs situated on the three FAST telescopes. The data obtained from the low-gain PMTs however exhibit a degree of instability and fluctuations, which is expected as the UV LED events are not properly detected, which further reduced the quality of UV LED calibration measurements for these PMTs. The temperature dependency will be discussed further in Section 4.

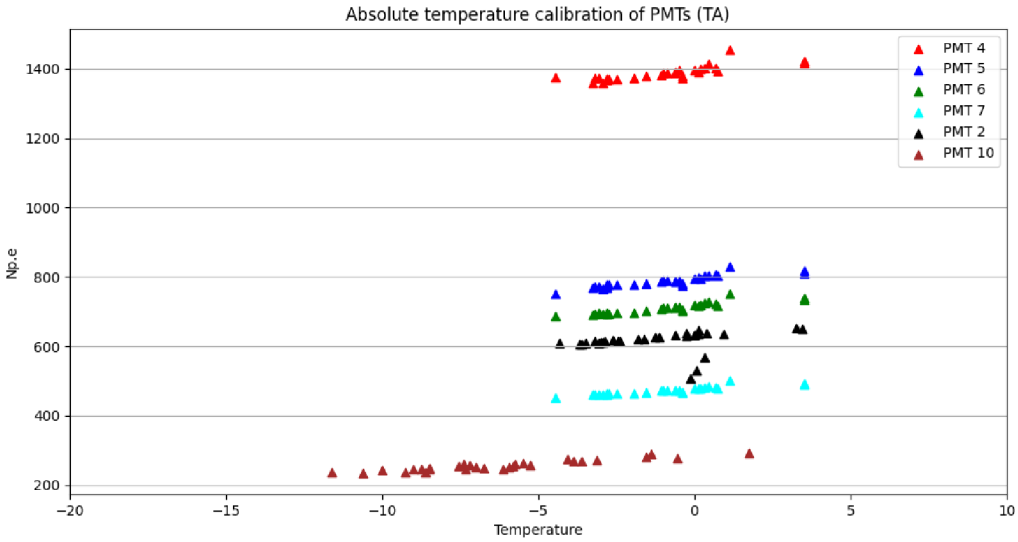

Figure 61 Absolute temperature calibration of PMTs demonstrating high gain on the FAST telescopes located on the TA site.

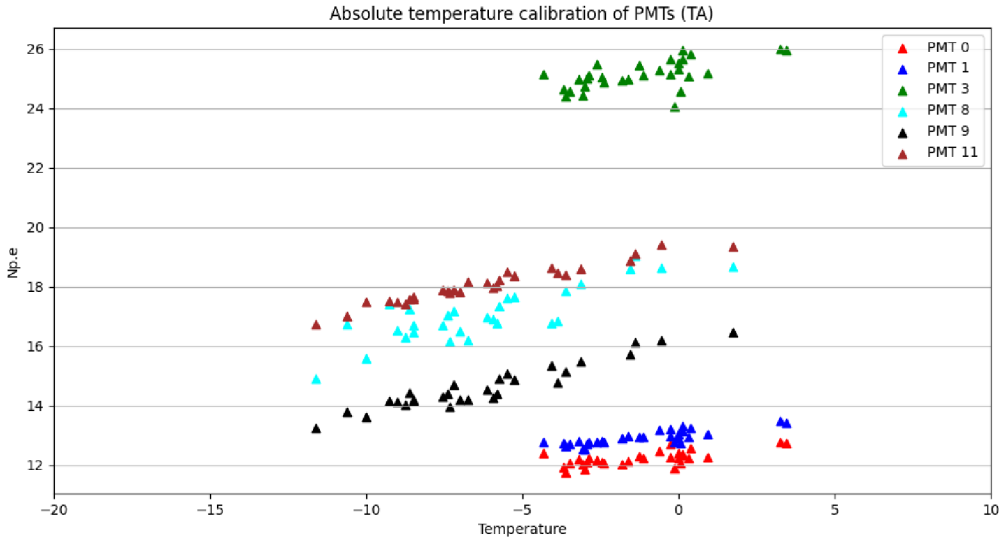

Figure 62 Absolute temperature calibration of PMTs demonstrating low gain on the FAST telescopes located on the TA site.

3. Deployment of a bokeh server

Bokeh is a python data visualization library developed for creating interactive graphs in a .html format. In addition, Bokeh enables the construction of a real-time visualization toolkit linked to Python code executed on a Bokeh server. One such server was deployed and is capable of displaying data from both the PAO and TA sites examined in the two previous sections. Currently, the Bokeh server displays both absolute and relatives calibration data regarding time and temperature stability for both Pierre Auger Observatory and Telescope Array. The server is composed of two tabs (PAO and TA) that facilitate real-time transition between the data of the two observatory locations. The observer can then choose between 5 sub-tabs, absolute and relative time calibration, absolute and relative temperature calibration and finally, a single event viewer.

Furthermore, the server was developed with a visualization of particular UV LED calibration events. The tool displays the UV LED events of all four PMTs on the PAO and all twelve PMTs on the TA sites. Currently, the viewer can display over 2 million individual events from the PAO site and close to 3 million events from the TA site. Figure 63 then displays the single event visualization of a UV LED calibration measurement of the 50th event from 10th of February, 2023 at 7 hours, 23 minutes and 40 second (UTC). The single data visualization allows for seamless transition between individual events. This can be done either manually, by directly typing the number of the desired events, or by using the blue arrows seen in figure 63, which change the event currently showing for the selected calibration measurement. The viewer can choose any date of the calibration run, and then select the individual calibration cycle desired. The visualization even allows for displaying events that were eliminated from the data analysis, as for example the events in 63 show no particular UV LED rectangular signal detected.

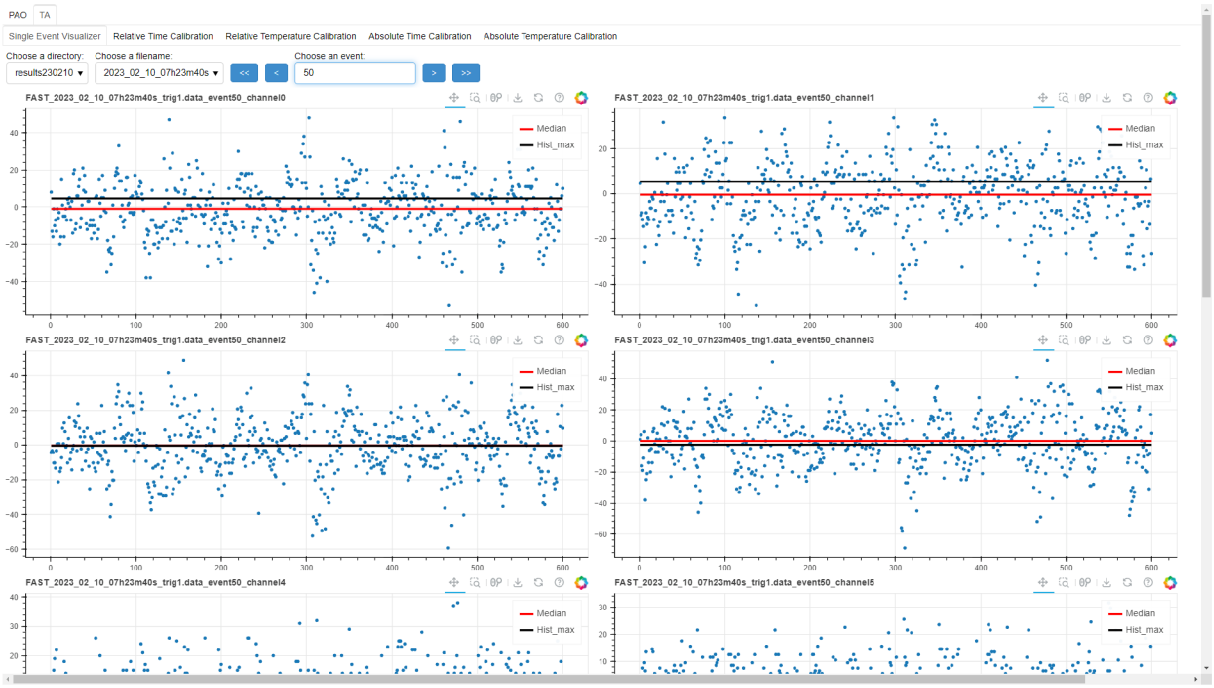

Figure 63 A screenshot of the deployed Bokeh server, currently displaying the single event visualization for the TA site.

Figure 64 | Absolute temperature calibration of PMTs demonstrating low gain on the FAST telescopes located on the TA site.

Figure 64 then provides a screenshot of the PAO tab currently displaying absolute time calibration of all four PMTs. The same data is also shown in figure 51 in Section 2.6.1. The viewer can then seamlessly transition between the individual tabs regarding all possible calibration methods utilized, as well as the single event visualization of the PAO UV LED calibration events.

The Bokeh server is set in part to provide easy access to all FAST data for the internal FAST collaboration. The FAST telescopes in both the PAO and TA sites are operated by designated shifters, who connect to the computers operating the telescope via a remote ssh tunnel. The shifters then operate the telescopes and can gather more UV LED calibration measurements, which upon data analysis can be displayed in real-time on the Bokeh server. This allows the shifters to properly assess the quality of the measurement in relatively low time, as the calibration measurement can be analyzed directly after obtaining the data. This will allow the shifters to look at both the absolute and relative signal for all PMTs present and assess the functioning quality, whether it will be with regard to time or temperature.

4. Discussion

The goal of the FAST project is to develop a commercially viable fluorescent detector of the UV radiation produced during an extensive air shower. The FAST telescopes capable of detecting said radiation are then set up in a grid to observe the faint fluorescent light. The telescope itself is comprised of numerous optical and electrical elements, mainly a camera box with four 200mm long PMTs that detect the UV light and further amplify the signal. It is important to ensure the quality of light detection of the PMTs. This is done mainly via a UV LED flasher present on the central mirror on all examined FAST telescopes, or a YAP scintillator.

Temperature fluctuations may directly and indirectly affect the signal of the PMT from the UV LED calibration runs. Firstly, the PMTs themselves are dependent on temperature, with a signal loss of around 0.4% per increase of a degree Celsius, as is shown in figure 23. The temperature of the PMT also impact the dark current present and the saturation current. Reaching the saturation current can cause loss of linearity of PMT response. However this effect was not observed in the provided data.

Furthermore, the temperature change also impacts the flasher in two different ways. The electromagnetic spectrum of the flasher itself is dependant on temperature, as the peak of the UV wavelength is shifted towards higher wavelength with rising temperatures. This is illustrated in figure 30. This effect is however only a few nanometers of peak wavelength shift, which is minuscule compared to the change in radiant flux due to temperature fluctuations, which is displayed in figure 31. The flasher emits the most amount of light at 30°C, then the flux is reduced to $\sim$ 80% of that toward the temperature of $\sim$ -15°C. This is however a gross approximation, as due to the lack of any raw data regarding the UV LED flasher stability, only an estimate about the dependency can be made. The shift of the electromagnetic spectrum of the flasher may impact the optical elements of the FAST telescope as well. The quantum efficiency of the PMT is highly dependant on the wavelength of incident light, as is the transmittance of the borosilicate primary windows of the PMT. The only two effect with the potential to noticeably alter the PMT signal is the loss of PMT sensitivity in regard to temperature, along with the decrease of the radiant flux of the UV LED flasher with decreasing temperature. The other mentioned effect may alter the PMT signal of only $\sim$ few percent at most. Thus only the two variables will be discussed further concretely in the context of data obtained from both the PAO and TA site.

Aside from the effect of temperature, the PMTs may exhibit a degree of signal loss with respect to time. The data provided by the manufacturer shows a potential 25% decrease in signal strength with several thousand hours of mean-time usage. The telescope can only operate on moonless night, so thus assuming the FAST telescope would gather data every possible night, the PMTs would reach almost 1500 hours of operational time in a year of usage. In reality, the mean-time is much lower, but it is nevertheless important to examine the time stability of all PMTs to ensure quality subsequent data analysis.

4.1. PAO data

A single FAST telescope was deployed in the Argentinian desert of Pierre Auger Observatory in 2020 and has been gathering data since. The telescope is also equipped with numerous sensors, measuring temperature, humidity, pressure, light or shutter status for example. The telescope is also provided with a UV LED flasher placed on the centre of its primary mirror. Data analysis obtained between March 2020 and March 2023 is provided in Section 2.6. Data was analyzed both in absolute numbers, in the number of photoelectrons produced during the event, along with relative calibration, by comparing individual PMT signal to a reference point, chosen as PMT1.

In absolute calibration, the PMT exhibit varying behaviour with respect to time. While the signal from PMT 3 is mostly stable, the PMTs 0, 1 and 2 experience drastic signal loss over the 3 year long period. PMT 0 in particular demonstrates signal loss of more than 50%. This is way more extreme than the data regarding life characteristic of a typical PMT provided by the manufacturer, seen in figure 22. This effect is further seen in relative numbers, as the signal of PMT0 falls in the range of the signal of PMT1. In addition, both PMT0 and PMT2 exhibit particular fluctuations, which cannot be explained by life characteristic of time drift of the PMTs. The only common denominator of these two PMTs is the fact that they are located on the same horizontal plane on the FAST telescope. A possible cause of the mentioned instability might be dust sedimentation, as the buildup of dust particles can cover the primary PMT windows, reducing the transmittance. Furthermore, the dust itself can damage the electronics operating both the PMT and the DAQ system of the FAST telescope.

It is important to ensure sufficient PMT stability in order to properly calibrate the data obtained from the detection of UHECRs. All PMTs present on a FAST telescope should, in theory, experience the same conditions and should behave in a similar manner. As is seen in Section 2.6, this is not the case, as the signal from the four PMTs is reduced in varying pace, indicating either variance in the life characteristic of the individual PMTs or perhaps a degree of damage to the PMT itself.

All the data provided is from the UV LED calibration measurement, obtained due to the UV LED flasher. It is possible, although highly unlikely, that the cause of the mentioned PMT behaviour is the flasher itself. Both environmental factors and human-induced disturbances can have a physical impact on the flasher, as any change in its position can result in a loss of light uniformity. The UV LED flasher is situated behind a small pinhole, and gradual tilting or falling of the flasher could potentially block the light, thereby explaining the observed behavior in the data. This effect should potentially alter the PMT located on the same horizontal plane equally, unless a degree of tilt or sideways movement was introduced to the flasher. Without conducting a manual examination of the physical conditions of the FAST telescope in PAO, it is highly improbable to deduce a definitive factor and elucidate the disparate PMT behavior.

Due to the signal loss in respect to time, it is difficult to assess the PMT dependency on temperature. Thus, the data was separated into two groups of data obtained up to December 2020 and subsequently from July 2023. A simple linear fit was performed on these two data sets to find the relation of the PMTs with respect to temperature. The fit can be seen in figure 65 for the first data set and in figure 66 for the second.

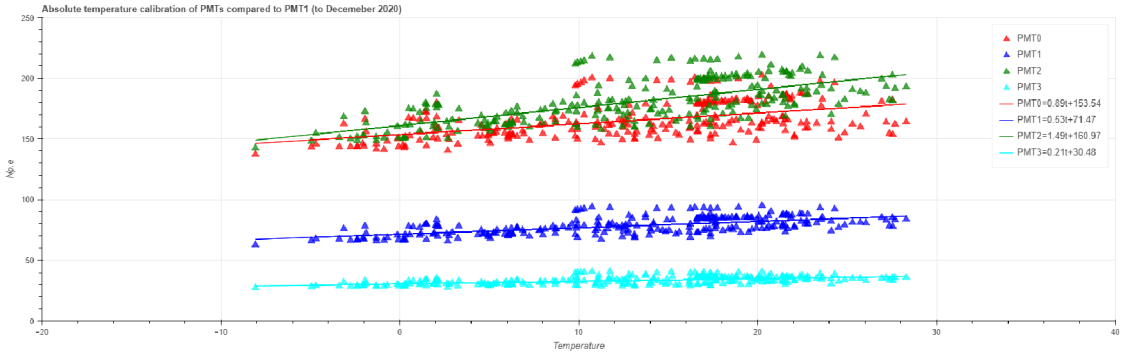

Figure 65 A fit of the relation between PMT signal in absolute values in regard to temperature. The displayed data was obtained from March 2020 to December 2020.

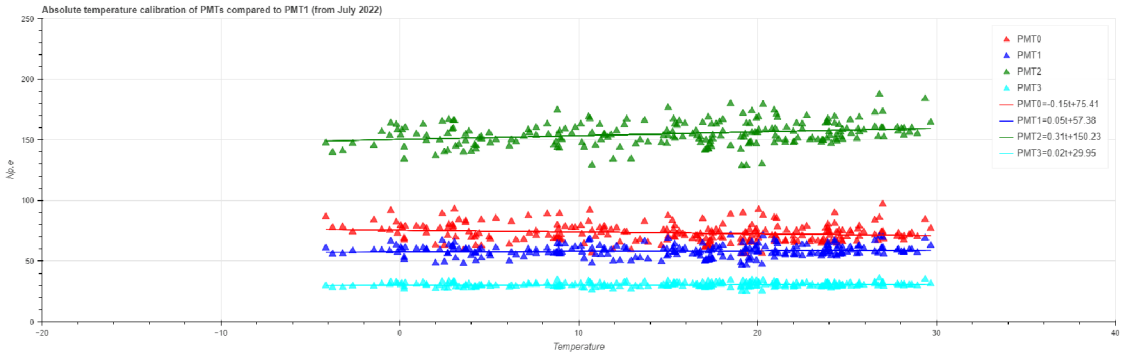

Figure 66 A fit of the relation between PMT signal in absolute values in regard to temperature. The displayed data was obtained from July 2022 to March 2023.

In the first time period of 2020, all PMTs exhibit an increase of signal strength with rising temperatures. This is directly in contrast to the data provided by the manufacturer, as the expected behaviours consists of signal reduction of $\sim 0.4\%$ per °C. A possible cause for such behaviour may be the effect of temperature on the UV LED flasher itself, as examined previously. A simple assumption from the data provided in figure 31, a temperature increase of 1°C would induce a signal increase of $\sim$ 0.3-0.5 %, up to 30°C. In theory, the variance in the radiant flux of the UV LED flasher should balance the loss of PMT sensitivity in regard to rising temperatures. The overall behaviour of the PMTs with respect to temperature should be relatively stable.

The data obtained from July 2022 to March 2023 exhibits this stable behaviour, as the slope of the fit of the four PMTs ranges from -0.15 to 0.31. The signal of PMT0 even decreases with rising temperature, which aligns with the expected behaviour. There are several possible reasons for this. A most likely cause is the gradual decline of the amount of light produced by the flasher itself. Up to the point where the effect of the change in radiant flux and PMT sensitivity balances out. This would, however, result in inaccurate or inadequate data regarding the flasher itself, since the relationship between the radiant flux and temperature would have to be considerably different. Another possible cause is an unknown, yet unconsidered effect, perhaps on the electronics the FAST telescope. Without examining the UV LED flasher and the PMTs manually, it is highly unlikely to determine a singular cause for the PMT signal behaviour shown in both presented figures.

4.2. TA data

In late 2022, three FAST telescopes were deployed in the Telescope Array observatory in Utah. All the 3 telescopes are equipped with numerous sensors measuring temperature, pressure, humidity, light or shutter status of the FAST hut. The telescopes are further equipped with the same UV LED flasher as the telescope stationed on the PAO site. Furthermore, one PMT from the north and middle telescopes provided with a YAP scintillator on the primary PMT window. However, the data shown in Section 2.7 were all obtained during UV LED calibration measurements. Data from January 16th to February 10th provided further.

The PMTs on the FAST telescopes exhibit different behaviour, as some of the PMTs detect the UV light from the flasher at thousand or even ten thousand counts, while certain other detect the UV light at a level of mostly a few hundred counts. It is important to isolate the cause of this effect, otherwise this incredible instability would severely lessen the quality of any further analysis. During the telescopes deployment, a series of YAP calibration measurements was conducted to assess the relative responses of the individual PMTs. Examples from the YAP calibration is then provided below, in figures 67 and 68.

	YAP_CALIB		
PMTID	2018-10-06	2019-09-06	2022-11-24
0	1.201	1.239	1.669
1	1.485	1.356	1.312
2	1.200	1.172	1.377
3	1.560	1.632	1.539
4	1.504	1.137	1.294
5	1.015	1.267	0.704
6	1.458	1.462	1.443
7	1.000	1.000	1.000
8	1.100	0.837	1.000
9	1.647	1.478	1.394
10	1.480	1.492	1.819
11	1.454	1.649	1.419

Figure 67 A table of the calibration constants measured during the YAP calibration run for the twelve PMTs located on the three FAST telescopes in the TA site. Taken from a presentation of the internal FAST collaboration.

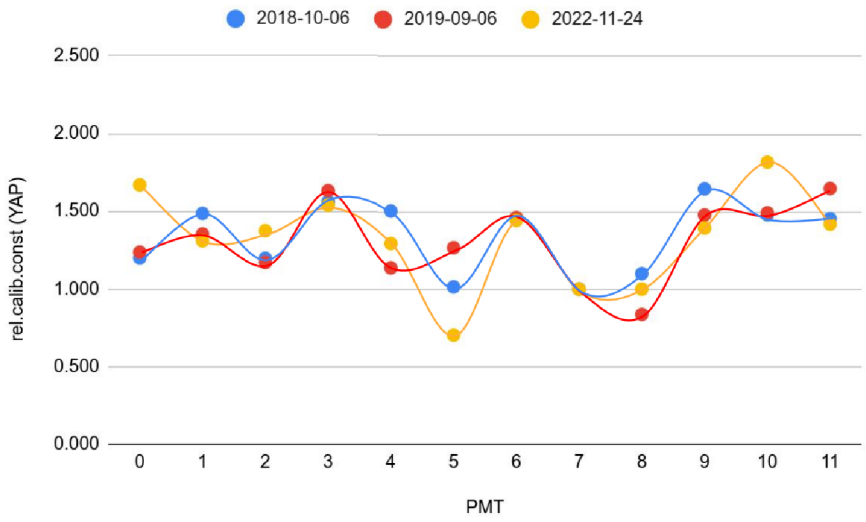

Figure 68 A visualization of the calibration constants measured during the YAP calibration run for the twelve PMTs located on the three FAST telescopes in the TA site. Taken from a presentation of the internal FAST collaboration.

The calibration constants are all in the same range, meaning the PMTs should exhibit measurements in the same count range as well. This does not happen during the UV LED measurements. Upon looking at events where no signal was detected, the noise from all twelve PMTs is in the range of a few tens of counts. This further indicates the PMTs are not at fault for the immense variance in the PMT gain. A possible cause might be the improper installation of the UV LED flasher, as the flasher itself is located behind a small pinhole as well, which might reduce the incoming light from certain directions if not placed properly. This would explain, why PMTs present on a single FAST telescope demonstrate both high and low gain measurements. Without examining the flashers manually, this cannot be confirmed, although due to the reasons provided above, this cause seems highly probable.

Time stability of the PMTs located on the TA site cannot be assessed properly, as the telescopes are only gathering data for a few months. Upon preliminary absolute time calibration data inspection, no signal loss can be observed during the time period in any of the examined PMTs. The lack of any meaningful gradual time-induced signal loss offers excellent view of the temperature dependency of the PMTs. The data in question are visualized in Section 2.7.2. A simple linear fit was performed on the absolute temperature calibration data as well, and can be seen in figures 69 to 71 for the north, middle and south TA FAST huts respectively.

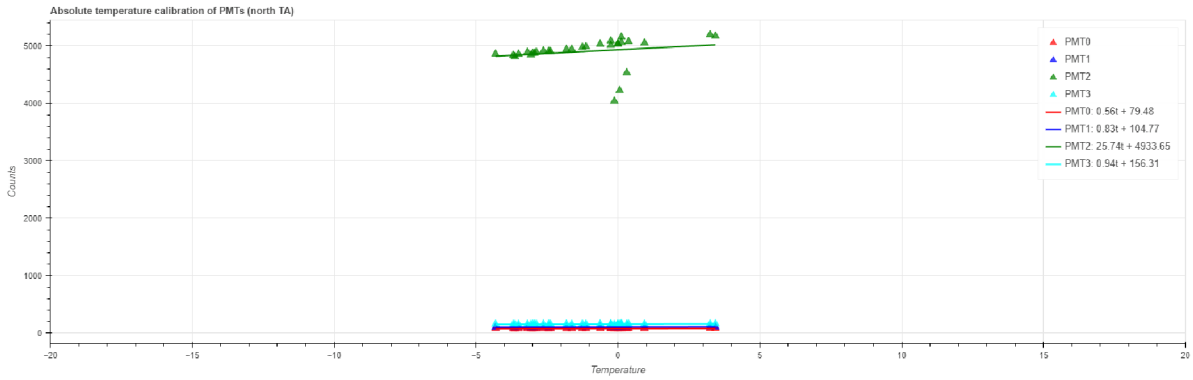

Figure 69 A fit of the relation between PMT signal in absolute values in regard to temperature. The displayed data was obtained from the north TA FAST hut from January 16th to February 10th, 2023.

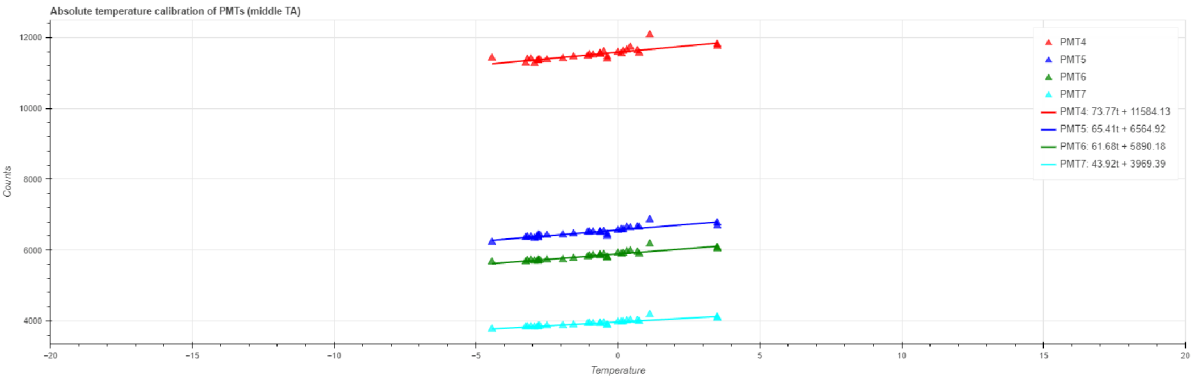

Figure 70 A fit of the relation between PMT signal in absolute values in regard to temperature. The displayed data was obtained from the middle TA FAST hut from January 16th to February 10th, 2023.

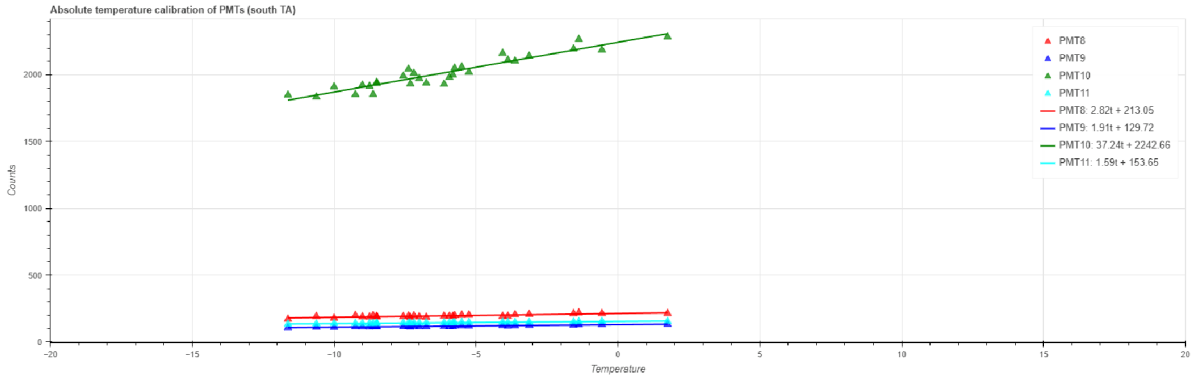

Figure 71 A fit of the relation between PMT signal in absolute values in regard to temperature. The displayed data was obtained from the south TA FAST hut from January 16th to February 10th, 2023.

All of the PMTs present on the TA site exhibit similar behaviour as the FAST telescope on the PAO site. An increase in signal strength with rising temperatures. To ensure accurate data analysis, only the temperature dependency should be depicted in the graphs, as there are no life characteristic limitations affecting the PMTs. The behaviour of the PMTs in response to temperature change further indicates an unknown parameter influencing the PMTs. The effect of the PMT sensitivity and the radiant flux change should, in theory, balance each other other and the PMT signal in regard to temperature should be stable. The increase in signal strength is fairly consistent with the data obtained from the first time period from the PAO site. Neither shift in the emitted UV wavelength nor change in the transmittance of the PMT window can cause the observed phenomena. The fact that the TA data is consistent with the PAO data suggest a presence of an unknown cause influencing the UV LED measurements. Determining whether this is due to the UV LED flasher or an inherent characteristic of the PMT is crucial for any further data analysis.

Conclusion

The Fluorescence detector Array of Single-pixel Telescopes is a modern concept of next-generation observatory of Ultra High-Energy Cosmic Radiation. Due to the exceptionally low minute flux of these incredibly energetic cosmic rays, a large net of telescopes has to be deployed to directly observe the faint fluorescent light produced by the excitation and subsequent de-excitation of nitrogen atoms in our atmosphere during an extensive air shower. An individual FAST telescope is comprised of a single circular primary mirror with 8 secondary mirrors in a "petal"shape. The mirrors reflect UV radiation onto a camera box made of four 200mm Hamamatsu Photomultiplier Tubes. The telescope offers a $30° \times 30°$ FOV and a collecting area of ~ 1 m^2. A UV filter is set up to eliminate parasitic light that may damage the PMTs. A shroud covering the telescope protects the optics and electronics from dust buildup. The telescope is then stationed in a special hut for further enhanced protection. The affordability and user-friendly nature of these telescopes make them a strong contender for the detection of Ultra-High-Energy Cosmic Rays (UHECRs).

A single FAST telescope was set up in the Pierre Auger Observatory in Argentina. The telescope has been gathering data from early 2020. Along the telescope in PAO, three more FAST telescopes have been deployed in the Telescope Array, Utah, U.S.A in late 2022. All of these telescopes are equipped with numerous sensors measuring temperature both inside and outside the FAST hut, humidity, pressure, light or shutter status. Furthermore, the telescopes are provided with a UV LED flasher for calibration purposes. In this thesis, data from the single PAO FAST telescope and three TA FAST telescopes were analyzed.

A single UV LED calibration, or run, is comprised of five individual cycles with an interval of 10 seconds between the cycles. Each cycle then consists of ~ 200 flashes, or events of the UV LED flasher for each PMT. The UV LED signal is a rectangular signal measured in counts in corresponding bins, each bins corresponding to 20 nanoseconds. Ideally, the rectangular signal can be described by a single non-zero value, its amplitude, or height. In practice, several different approaches were discussed. Median, histogram maximum or a Gaussian fit were examined as possible options. For analysis of the UV LED events, histogram maxima were utilized. The aim of the calibration is to assign a single value most representative of the entire calibration run. To achieve this, the mean of the histogram maxima is chosen, as the UV LED calibration run is comprised of ~ 1000 events for individual PMTs. To eliminate faulty measurements, several filter were set up during the data analysis. Signal detection filter, standard deviation filter or calibration runs with no UV LED flashes filter were employed. Calibration runs were then visualized in regard to both time and temperature. The calibration runs can then be examined in absolute numbers, in Np.e or in relative values, by comparing the PMT signal to a chosen PMT reference.

Time and temperature stability of the PMTs present in a FAST telescope are of primary concern. Time drift can account for the signal loss observed during uninterrupted operation of the PMTs, while life characteristic provides insight into the stability of the PMT over a long time period of several thousand hours. It is expected, that upon a few thousand hours of mean time usage, the signal strength may decrease to ~ 80 %. This can vary upon the individual PMT. Temperature affects the FAST telescope in a number of ways. The PMTs themselves are highly dependant on temperature, as the sensitivity of the PMT is reduced by 0.4 % per °C. Furthermore, both saturation and dark current are temperature dependent as well. This can lead to non-linearities in the output signal. Temperature fluctuations also impact the UV LED flasher responsible for the analyzed calibration measurements. Upon temperature change, the electromagnetic spectrum of the emitted UV light is shifted, which can impact the PMTs, as the quantum efficiency and the transmittance of the borosilicate window glass are dependant on the wavelength of incident light. The shift in peak wavelength is however minuscule and can be neglected. Radiant flux of the flasher is however drastically dependant on temperature, with a peak at ~ 30°C. Upon decrease in temperature, the radiant flux is reduced to ~ 80% at -15°C. By approximating the said effect, the PMT signal would increase by 0.3-0.5% per every °C up to 30°C. In theory, the effect of radiant flux and decrease in PMT sensitivity should balance itself out.

The data obtained from the FAST telescope stationed on the PAO site provides interesting insight regarding the time stability of the PMTs. The PMTs gathered UV LED calibration measurements in a 3-year long time period. Three of the PMTs exhibit severe signal loss with respect to time. This is somehow expected, as the PMT signal can get reduced in time, through a process called life characteristic of the PMT. However PMT0 demonstrates signal reduction of more than suggested data provided by the manufacturer. This is important to adequately assess the time stability of the PMT to ensure quality prolonged usage due to the economic constraints set by the FAST project. All PMTs also exhibit a degree of fluctuation, as the signal is not constant due to both temperature dependency and a present variance in the data. The data presented with respect to temperature is however clouted due to the effect of life characteristic of the four PMTs. Upon data separation into two time periods, where the PMT signal decrease is not prominent, the relation between PMT signal and temperature can be inferred. In the first period of time, from March 2020 to December 2022, All PMTs demonstrate an increase in signal with rising temperatures, directly in contrast to the expected behaviour provided by the manufacturer. In the second time period from July 2022 to March 2023, the PMTs exhibit fairly stable behaviour in regard to temperature, with one of the PMTs demonstrating subtle signal decrease with rising temperature. This behavioural change may be induced by the wear on the UV LED flasher itself, or perhaps even further decrease in PMT sensitivity. To evaluate the causes of the mentioned effects, manual examination of the telescope on the PAO site is mandatory.

Three additional FAST telescopes were deployed in the TA site in late 2022. The UV LED calibration measurement exhibit variance in the PMT signal, as some of the PMTs detect the event at thousands of counts, while other in mere hundreds of counts. This is not innately due to the PMTs themselves, as the YAP calibration measurement conducted in November 2022 on site measured the relative responses of the PMTs. The difference in signal levels is thus most probably due to improper setup of the UV LED flasher itself. The flasher sits behind a small pinhole, and any gradual movement of the flasher will inherently impact the UV LED calibration runs, as the light will not traverse through the pinhole properly. This can explain as to why some of the PMTs on the same FAST telescope experience significantly varying gain.

Calibration measurements from January 16th to February 10th, 2023 are available for the FAST telescopes in the TA site. Due to to the small time span of the measurements, no final assessment can be made regarding the time stability of the PMTs, although from the small sample size, the telescopes behave in a relatively stable manner in regard to time. The relation between signal strength and temperature align with the data obtained from the PAO site, as the telescopes exhibit increase in signal values with rising temperatures. This is again directly in contrast to the data provided by the manufacturer. However, due to the lack of any signal reduction due to time instability of life characteristic, the data from the TA site is suitable for assessing the relation between the UV LED calibration measurements and temperature. To evaluate the causes of the mentioned effects, manual examination of the telescope on the TA site is mandatory.

For the purpose of real-time data visualization, a python library Bokeh was utilized. Bokeh allows for interactive data visualization running on a specific server directly linked to python code. The server displays all aforementioned calibration approaches. Absolute time and temperature calibrations along with relative time and temperature calibrations are available for both the PAO and TA sites. The server also offers a single event visualization displaying individual UV LED events detected throughout the calibration runs. The server can serve as direct feedback for shifters currently operating the FAST telescopes via ssh tunnels as to the quality of calibration data obtained upon analyzing the data through a developed python data analysis script.

The FAST project successfully proved its viability in detecting UHECRs through the detection of faint fluorescent UV light during an EAS. However, calibration of the technique is of dire important to adequately assess and analyze data obtained through fluorescent FAST telescopes. Of particular importance are data regarding time and temperature stability of the PMTs present on a FAST telescopes. Time stability ensures prolonged life cycle of the PMT, while temperature stability ensures stable and reliable PMT signal with respect to environmental conditions affecting the telescope. Calibration can be done in absolute values, in Np.e, or by choosing a reference PMT, comparison of the relative values of the PMTs can be conducted. Both approaches are beneficial, as valuable information can be deduced through these methods. Further solid and reliable time and temperature stability of the PMTs of the FAST telescopes is crucial for an adequate detection of UHECRs.

References

[1] Koutný M. *Relative calibration of fluorescent telescopes of the FAST project*, 2021.

[2] Bietenholz, Wolfgang. *"The most powerful particles in the Universe: a cosmic smash."*, 2013. https://arxiv.org/abs/1305.1346

[3] Thompson, D. J. and Colleen A. Wilson-Hodge. *Fermi Gamma-ray Space Telescope*, 2022 https://ntrs.nasa.gov/api/citations/20220003070/downloads/Fermi%20Gamma-ray.pdf

[4] Zilles, A. *Introduction to Cosmic Rays and Extensive Air Showers . In: Emission of Radio Waves in Particle Showers* 2017, Springer Theses. Springer, Cham. https://doi.org/10.1007/978-3-319-63411-1_1

[5] Schroder, Frank G. *Radio detection of Extensive Air Showers*, ECRS 2016.

[6] T. Abu-Zayyad et al *The surface detector array of the Telescope Array experiment*, Nuclear Instruments and Methods in Physics Research Section A: Accelerators, Spectrometers, Detectors and Associated Equipment, Volume 689, 2012, https://doi.org/10.1016/j.nima.2012.05.079

[7] I. Allekotte et al, *The surface detector system of the Pierre Auger Observatory*, Nuclear Instruments and Methods in Physics Research Section A: Accelerators, Spectrometers, Detectors and Associated Equipment, Volume 586, Issue 3, Pages 409-420, 2008, https://doi.org/10.1016/j.nima.2007.12.016

[8] Pierre Auger Observatory (PAO), Argentina, (cit. 22.4.2023). https://www.auger.org/

[9] Letessier-Selvon, Antoine & Stanev, Todor, *Ultrahigh Energy Cosmic Rays*, Reviews of Modern Physics, 2011.

[10] Mandat Dusan, M. Palatka, M. Pech, P. Schovanek, P. Travnicek, L. Nozka, M. Hrabovsky et al. *"The prototype opto-mechanical system for the Fluorescence detector Array of Single-pixel Telescopes."Journal of Instrumentation 12*, no. 07 (2017): T07001. https://iopscience.iop.org/article/10.1088/1748-0221/12/07/T07001

[11] Malacari M., et al. *"The first full-scale prototypes of the fluorescence detector array of single-pixel telescopes."Astroparticle Physics*, 119 (2020): 102430. https://doi.org/10.1016/j.astropartphys.2020.102430

[12] T. Fujii et al, *Detection of ultra-high energy cosmic ray showers with a single-pixel fluorescence telescope, Astroparticle Physics*, Volume 74, 2016, Pages 64-72, ISSN 0927-6505. https://doi.org/10.1016/j.astropartphys.2015.10.006

[13] Hamamatsu Photonics K.K, *Photomultiplier Tubes, Basics and Application (edition 4a)*. https://www.hamamatsu.com/content/dam/hamamatsu-photonics/sites/documents/99_SALES_LIBRARY/etd/PMT_handbook_v4E.pdf

[14] Roithner LaserTechnik, *Technical Data, RLT365-10E*. Available at http://www.roithner-laser.com/datasheets/led_div/rlt365-10e.pdf

[15] DBeaver, a free multi-platform tool for database viewing. https://dbeaver.io/

[16] Python Software Foundation. Python Language Reference, version 3.9. Available at http://www.python.org

[17] Jetbrains, Integrated development environment PyCharm, version 2021.1.3. Available at https://www.jetbrains.com/pycharm/

[18] Harris, C.R., Millman, K.J., van der Walt, S.J. et al. *Array programming with NumPy. Nature*, 585, 357–362 (2020). https://doi.org/10.1038/s41586-020-2649-2

[19] J. D. Hunter, *"Matplotlib: A 2D Graphics Environment"*, *Computing in Science & Engineering*, vol. 9, no. 3, pp. 90-95, 2007. https://doi.org/10.1109/MCSE.2007.55

[20] Bokeh Development Team (2018). Bokeh: Python library for interactive visualization http://www.bokeh.pydata.org.

[21] Michael Bayer. SQLAlchemy. In Amy Brown and Greg Wilson, editors, *"The Architecture of Open Source Applications Volume II: Structure, Scale, and a Few More Fearless Hacks"*, 2012. http://aosabook.org

List of abbreviations

FAST	Fluorescence detector Array of Single-pixel Telescopes
UHECR	Ultra High-Energy Cosmic Radiation
eV	Electronvolt
UV	Ultraviolet
PMT	Photomultiplier Tube
FOV	Field of vision
PAO	Pierre Auger Observatory
TA	Telescope Array
SEP	Solar Energetic /article
GCR	Galactic Cosmic Ray
AGN	Active Galactic Nuclei
EAS	Extensive air shower
AGASA	Akeno Giant Air Shower Array
UPW	Ultra-pure Water
BRM	Black Rock Mesa
LP	Low-pass
FADC	Fast analog-to-digital converter
DAQ	Data Acquisition
RPi4	Raspberry Pi 4
Np.e	Number of photoelectrons
YAP	Yttrium-Aluminum Perovskite

Appendix

```python
import os
import matplotlib.pyplot as plt
import numpy as np

filename = "FAST_2023_01_23_10h33m54s_trig1.data_event101_channel3.txt"
with open(os.path.join(r'C:\Users\mkolo\Desktop\TA\results230123', filename)) as f:
    raw = f.read()
    signal = np.fromstring(raw, dtype=int, sep=' ')
    rawdata = np.mean(signal[:500]) - signal

rawdata_refined = rawdata[1999:2399]
value1 = np.histogram(rawdata_refined, 200)[1][np.argmax(np.histogram(rawdata_refined, 200)[0])]
value2 = np.median(rawdata_refined)

bins = np.arange(1, len(rawdata) + 1)
plt.scatter(bins, rawdata, s=3, marker="o")
plt.xlim([1900, 2500])
plt.hist(rawdata, 200)
plt.title("Visualization of a single PMT event")
plt.suptitle(filename)
plt.xlabel("Bins (1 bin = 20 ns)")
plt.ylabel("Counts")
plt.axhline(value1, color="black", label="Histogram maximum")
plt.axhline(value2, color="red", label="Median")
plt.legend()
plt.show()
```

Figure 72 An example screenshot of python code for visualization of a single UV LED calibration event.

```python
# Create a nested dictionary for data storage
channel_id = [f"ch{i}" for i in range(12)]
channel_std = [f"std{i}" for i in range(12)]
channels = channel_id + channel_std + ['temp1'] + ['temp2'] + ['temp3']
nested_dict = {d: {ch: [] for ch in channels} for d in dates}

high_stdev = []
stdev_list = []
error_list = []
for filename in filenames:
    if filename[5:25] not in nested_dict:
        continue
    with open(os.path.join(path, filename)) as f:
        raw = f.read()
        signal = np.fromstring(raw, dtype=int, sep=' ')
        rawdata = np.mean(signal[:500]) - signal
        rawdata = rawdata[1999:2399]
        value = np.histogram(rawdata, 200)[1][np.argmax(np.histogram(rawdata, 200)[0])]
        if len(rawdata) < 1:
            value = 0
            rawdata = [0, 0]
            print(filename)  # Check if the measurements are not empty
        if value < 40:
            error_list.append(filename)
            value = 0  # Check for a signal present
        #if value > 40 and statistics.stdev(rawdata) / value > 0.2:
            #stdev_list.append(statistics.stdev(rawdata))
            #high_stdev.append(filename)
        #value = 0  # Removes events with high standard deviation
```

Figure 73 An example screenshot of python code for data analysis of the UV LED flasher events for the FAST data of the TA site.

```python
path_to_abscsv = r'C:\Users\mkolo\Desktop\FAST data - Copy15.4\abs.csv'
abs_time = []
abs_temp = []
abs_PMT = [[] for i in range(4)]
abs_PMT_names = ['PMT0', 'PMT1', 'PMT2', 'PMT3']
with open(path_to_abscsv, newline='') as abs_csvfile:
    reader = csv.DictReader(abs_csvfile)
    for r in reader:
        abs_time.append(datetime.strptime(r['Time'], '%Y_%m_%d_%Hh%Mm%Ss'))
        abs_temp.append(r['temp'])
        for i in range(4):
            abs_PMT[i].append(float(r[abs_PMT_names[i]]))


values = [{'name': 'PMT 0', 'x': abs_time,
           'y': abs_PMT[0], 'color': 'r', 'marker': '^'},
          {'name': 'PMT 1', 'x': abs_time,
           'y': abs_PMT[1], 'color': 'b', 'marker': '^'},
          {'name': 'PMT 2', 'x': abs_time,
           'y': abs_PMT[2], 'color': 'g', 'marker': '^'},
          {'name': 'PMT 3', 'x': abs_time,
           'y': abs_PMT[3], 'color': 'cyan', 'marker': '^'}]


fig, ax = plt.subplots(figsize=(12, 6))

for signal in values:
    ax.scatter(signal['x'], signal['y'],
               color=signal['color'],
               label=signal['name'],
               marker=signal['marker'])

ax.legend()
ax.grid(axis='y')
ax.set_xlabel("Date")
ax.set_ylabel("Np.e")
ax.set_title("Absolute time calibration of all PMTs (PAO)")
plt.show()
```

Figure 74 An example screenshot of python code for visualizing the absolute time calibration of the PMTs on the FAST telescope of the PAO site